Mechanism and Control of Microtubule Dynamic Instability Probed by *in Vitro* Reconstitutions and Microfluidics Approaches

Christian Duellberg

University College London
and
Cancer Research UK London Research Institute
PhD Supervisor: Dr. Thomas Surrey

A thesis submitted for the degree of
Doctor of Philosophy
University College London
January 2014

Declaration

I Christian Duellberg confirm that the work presented in this thesis is my own. Where information has been derived from other sources, I confirm that this has been indicated in the thesis.

Abstract

Microtubules are non-covalent polymers that form an essential part of the cytoskeleton in eukaryotic cells. Alternating phases of growth and shortening are essential for space exploration, force generation and facilitate rearrangements of the microtubule cytoskeleton in response to various stimuli. Microtubule associated proteins regulate filament dynamics and can transport cargoes. The mechanism of how microtubules grow, what triggers the transition from a growing to a shrinking microtubule, and the interplay between the various microtubule-associated proteins is only poorly understood. *In vitro* reconstitution approaches from purified components in combination with microfluidics techniques and simultaneous multi-colour total internal reflection florescence microscopy were employed to shed new light on the mechanism of microtubule dynamics and the interplay of proteins that bind specifically to growing microtubule ends.

Tubulin undergoes conformational changes during incorporation into the polymer. Using a conformation-sensitive designed ankyrin repeat protein probe, it has been found here that these conformational changes occur at much later steps during incorporation into the polymer than previously appreciated.

Growing microtubules switch to a rapid shortening phase unless their ends contain a stabilizing structure whose nature is not fully understood. The decay of this stabilizing structure was directly measured by rapid tubulin dilutions and predictions from several theoretical models have been tested. The density of a particular tubulin conformation recognized by microtubule End Binding proteins (EB1/Mal3) could be linked to filament stability.

Microtubule end tracking proteins form a dynamic protein interaction network. Here, the molecular mechanism of several main players of these proteins that lead to growing microtubule end accumulation of the motor protein dynein has been elucidated by *in vitro* reconstitutions.

The bottom up approach applied in this thesis yielded new information about fundamental properties of microtubule dynamics and gained new insight into the interplay of an important class of microtubule associated proteins.

Acknowledgement

I thank Thomas Surrey for giving me the opportunity to do my PhD thesis in his research group. It has been a time filled with blood, sweat and tears but also very rewarding moments and episodes. I learned a lot during that time (scientifically and about myself). Thomas has been a great supervisor throughout the dissertation. I thank him for his trust and the freedom I had to do what I thought is the best thing to do next. He was always available when I needed his advice and always found the time to discuss data very thoroughly and was very supportive. He made it possible for me to have really nice collaborations with excellent labs from Switzerland, France and UCL that –in the end- all turned out to be quite fruitful (and for some, the harvesting is not over yet). I thank Michel Steinmetz from the Paul Scherer Institute and his lab (in particular Indranie Sen and Ruben Buey) for all the help and advice with the +TIPs and the great hospitality when I visited the lab for experiments. I thank Ludovic Pecqueur and Marcel Knossow from CNRS in France for a great collaboration – we DARPinned it down. And I thank David Holmes from UCL Nanotechnology centre in London who helped me getting started with the whole microfluidics business.

I thank my thesis advisory committee members Oliver Gruss and Elmar Schiebel for the Heidelberg period and Richard Treisman and Takashi Toda in London for valuable input. And of course many thanks to Ewa Paluch and Simon Bullock for reading this entire thesis!

I thank the whole Surrey lab; it has been a pleasure to be in such an awesome group. I never took this great atmosphere for granted. Everybody (without exceptions) was always very helpful. I thank Hella – we started on the same day and we will have our vivas within 24 hours proximity. We survived together. We survived India & France. We survived the PhD (not sure about the damage yet). Sebastian: You, Peter and Ivo set the bar quite high when I started. It sometimes made me feel a bit stupid but also motivated me a lot. We had great times throughout the whole time and I am still traumatised from that overdose of Belgian beer. Emanuel: It has been a blast French Notting Hill man! Let's chase the only girls in the world sometime soon. And thanks for all the *Xenopus* extracts! Franck: Your accent free "Ode an die Freude" was very impressive. Keep on singing when you're winning. Reverend Todd: Which Carnival do

we go next? So far, I visited every home region of all the lab members except yours. So we have a plan here! Surajit: Thanks for the invitation to Calcutta. That was a great experience. And thanks for all the cooking! Johanna: I am honoured to be 50 % of this great duo, generally called “the hungry two”! Hope there will be some more seminars with attached dinner soon! Iris: Thanks for providing your garden for all the BBQs. I wouldn’t know where else to sleep. But you should get rid of all these insects that start to attack when one is a sleep. On the other hand, I thank you for all the insect cells in the lab. Martina: Best Croatio-Spanish wedding ever; great times at the Teufel. Nic: Thanks for hosting the first British wedding I’ve been to. And thanks for the help in the lab so far. But I am afraid the real soul sucking part is still ahead of us. Gergo: You know when it’s best to show up: George & monkey man& Ministry - forever. Christian H: We saw Gaspard de la nuit by Pogorelich live (well, he suc.. , was not in a good mood on that day) but still, something for the “life time bucket list”. And the rather new ones (Einat, Rupam, Jonathan and Claire): I’ll still be around a bit to create some memorable stories.

I want to thank all people from EMBL and LRI for playing their role in my little PhD adventure! The whole LRI 4th floor has been a good crowed: Sabine, Charlie, Xavier, Ralph, Sophia, Richard, Anastasia, Claire, John, Francesco, Mark, Daniel, Thijs, Ruth and Tessa.

Special thanks to Mariana, I am grateful to have met you.

I thank Orit and the EMBL auditorium with its grand piano for making my EMBL time truly special for me. I thank Anni and Lotte for all the adventures and white Rock n Roll fun times. Nein Mann, Ich will noch nicht gehen, denn wir machen jetzt alles kaputt. Lotte, you were the best flatmate possible.

And of course a very special thank you to my parents! I wouldn’t know where to start so I am just saying that I am very very grateful for everything.

Table of Contents

Table of figures

List of tables

Abbreviations

Abbreviations for chemicals are listed in table 1 in section 5.1

%:Per cent (one part of hundred); **+TIP**: Plus end tracking protein; proteins that accumulate specifically at growing microtubule ends; **aa**: Amino acids; **Anova**: Analysis of variance, a statistical test (IP et al, 2007); **BSA**: Bovine serum albumin; c-terminus: carboxy -terminal end of a protein or polypeptide; **CAP-Gly domain**: Cytoskeleton-associated Protein Glycine-rich Domain; **CLASP**: Cytoplasmic linker associated protein 1; **CLIP**: Cytoplasmic linker protein; **Da**: Dalton (unified atomic mass unit) kDa stands for kiloDalton **DARPin**: designed ankyrin repeat proteins; **DNA**: Deoxyribonucleic acid; **EBs**: End Binding protein (EB1, EB2 and EB3 in humans, the fission yeast homolog is called Mal3); **e.g**.: exempli gratia ("for example") **EGFP**: Enhanced green fluorescent protein; **EMCCD**: Electron-multiplying charge-coupled device; **fps**: Frames per second; number of frames in a time laps movie per seconds; **GFP**: Green fluorescent protein; **GO**: Glucose oxidase; an enzyme; **GSK3**: Glykogensynthase-Kinase 3; **H**: helix; **His/ 6xHIS**: Histidine tag (a linear sequence of 6 to 10 histidines used for protein purification or antibody mediated detection; **kDa**: see Da; **L**: Loop; **i.e**.: id est ("that is" or "which means") **M**: Number of molecules per litre; 1 M= 1 mol/l ≈ 6.02 * 1023 /l; **MACF**: Microtubule actin crosslinking factor, a protein; **Mal3**: See EBs; **MAP**: Microtubule associated protein; **MCAK**: Mitotic centromere-associated kinesin, a protein that induces microtubule depolymerisation; **m**: meter **mCherry**: A fluorescent protein (similar to GFP) with different spectral properties; **MTs**: Microtubules; **N-terminus**: Amino-terminal end of a protein or polypeptide; **OD**: "optical density"; **p value**: Significance value in statistical tests (Dorey, 2011); **p150:**Protein subunit of the dynactin complex with a molecular weight of 150 kilodalton, synonym p150 glued; **PCR**: Polymerase chain reaction; **RB3-SLD**: RB3 is part of a protein family that contains a stathmin like domain; **RNA**: Ribonucleic acid; **SE**: Standard error; **sec**: second; **SLD**: Stathmin like domain; **StDev**:Standard deviation; **SXIP**: Consensus sequence; a short linear motif within proteins that mediate protein protein interactions with EBs; **T2R**: Protein complex consisting of 2 tubulin heterodimers and RB3-SLD **TIRF:** Total internal reflection fluorescence microscopy; **U test**: A statistical test (Mann et al 1947); **XCTK2**: Xenopus c terminal kinesin, minus ends directed motor protein from the kinesin 14 family.
Standard prefixes for the metric SI units of measure: M: Mega (10^6); k: Kilo (10^3); **m**: mili (10^{-3}) **µ**: Micro (10^{-6}); **n**:Nano (10^{-9}); **p**: Pico (10^{-12}).

Chapter 1. Introduction

1.1 The cytoskeleton

The cytoskeleton fulfils a variety of cellular functions and is generally divided into three subclasses of filaments: Actin, Intermediate filaments and microtubules (MTs). All filament types act as scaffold structures and contribute to the overall shape of different cells which gave rise to their name as the skeleton of the cell. However, the functionality for all of these filament types extends the role as pure static elements by far.

Actin can be usually found at the cell periphery, where is forms a dynamic meshwork along the plasma membrane. MTs typically originate from a specialized MT organizing centre and show a radial arrangement. Due to the large heterogeneity within intermediate filaments, it is hard to generalize their arrangements. Typical arrangements of cytoskeleton arrangements in cultured cells are presented in **Fig.1.**

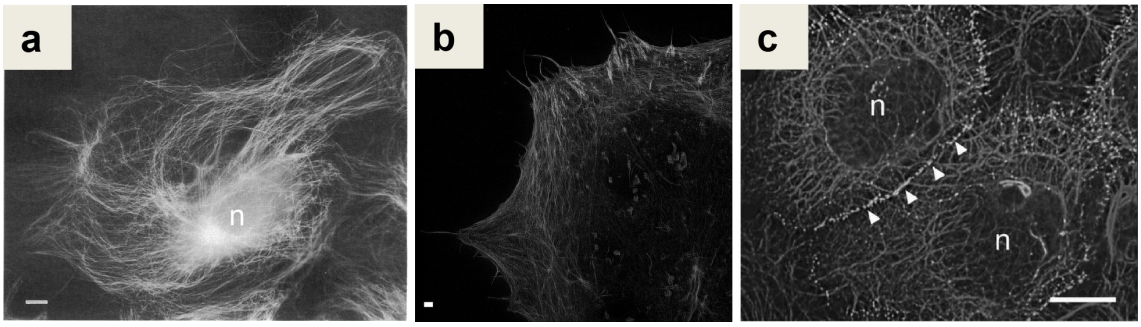

Figure 1: Organisation of the cytoskeleton in mammalian cells

(**a**) Fluorescence immunostaining against MTs in an interphase newt lung cell. Scale: 10 µm (from (Gliksman et al., 1993)). (**b**) Structured illumination fluorescence immunostaining against actin of a HeLa cell in interphase. Scale: 1 µm. (from (Hosny et al., 2013)). (**c**) Fluorescence immunostaining of keratin intermediate filaments in an interphase skin keranocyte and their attachment to desmosomes (dots at the cell periphery indicated by arrows). Scale: 20 µm. (from (Kim and Coulombe, 2007)) n=nucleus.

Actin exists in a monomeric form (G-actin) which can polymerize into filaments (F-actin) in which two actin strands are arranged in a helical fashion to form a polar filament with an outer diameter of ~ 8 nm (Holmes et al., 1990, Otterbein et al., 2001). Actin monomers assemble in an ATP bound state and ATP hydrolysis provides the energy for filament dynamics (Schuler, 2001). Hydrolysis followed by phosphate release destabilizes actin filaments and actin filaments can polymerize, depolymerize

and/or exhibit treadmilling like behaviour (Carlier and Pantaloni, 1988, Jegou et al., 2011, Kirschner, 1980). Filament dynamics are controlled by a large number of actin binding proteins that control filament nucleation, polymerisation/depolymerisation and its arrangement into gel like arrangements (Niederman et al., 1983, Lee and Dominguez, 2010, Higgs, 2001, Witke et al., 1998). Many functions of actin filament rely on ATP utilizing myosin motors that can walk along actin filaments, generating contractile elements (Levayer and Lecuit, 2012).

G actin regulates gene expression (Grummt, 2006, Treisman, 2013) and actin has been found to be a direct cofactor of RNA polymerases (Philimonenko et al., 2004). Furthermore, actin is implicated in signalling events associated with apoptosis (Wang, 2000).

The actin network participates in forces generation on many levels. Muscle based movements are based on myosin filaments that slide along actin filaments (Herzog et al., 2012). Cellular movements require constant rearrangements of actin filaments during protrusion formation at the leading edge, adhesion, contraction, and retraction at the rear of cells (Etienne-Manneville, 2013). Actomyosin complexes are essential for hydrostatic pressure generation, crucial for cell rounding prior cell division and protrusion formation in bleb based cell motility (Stewart et al., 2011, Paluch and Raz, 2013). At later stages of cell division, actin and myosin form a contractile ring for the abscission of the two cells at late stages of cell division in the process of cytokinesis (Glotzer, 2005).

Intermediate filaments are a complex group of fibrous cytoskeleton proteins encoded by at least 70 different genes. They are very different from actin or MTs as they do not assemble and disassemble using NTP hydrolysis and lack polarity. Usually, monomers assemble in an antiparallel fashion into tetramers without intrinsic polarity. These tetramers then can form higher ordered structures and form filaments with a diameter of about 8-12 nm (intermediate between actin and MTs/myosin filaments in skeletal muscles) (Chung et al., 2013).

Intermediate filaments act as tension bearing elements and contribute to cell shape and cell rigidity and play important roles in cell-cell and cell-matrix contacts and maintain tissue integrity in complex with desmosomes and hemi desmosomes (Harmon and Green, 2013, Zhang and Labouesse, 2010) (**Fig.1c**). Furthermore, they are important for

cell migration (Chung et al., 2013). A specialized group of intermediate filaments are nuclear lamins that build a meshwork in the periphery of the nucleus. They provide stability of the nucleus and are important for nuclear assembly and chromatin organization (Zuela et al., 2012).

The microtubule cytoskeleton participates in almost all cellular processes, including cell motility, cargo transport, cell division and morphology maintenance or changes (Wade, 2009).

MTs are hollow proteinous cylinders with an outer diameter of ~25 nm composed by the α tubulin β tubulin heterodimer. Similar to actin, MTs exhibit intrinsic polarity. The end where β tubulin is exposed is called the plus end and the end where α tubulin is exposed is called minus end (**Fig.2**) (Mitchison, 1993).

MTs are dynamic, which means that they alternate between phases of growth and shrinkage (called dynamic instability). Generally, the plus end is more dynamic. In the cell, minus ends are usually capped within the MT organizing centre and show little dynamicity. From these MT organizing centres, MTs show a radial arrangement with MT plus ends emanating towards the cell periphery (Desai and Mitchison, 1997).

From the interphase to mitosis transition or during cell differentiation, the microtubule cytoskeleton rearranges tremendously. MT dynamics and spatial MT arrangement is under the control of many microtubule associated proteins (MAPs) and the target of many therapeutic strategies in the treatment of various cancer forms (Wade, 2009, Desai and Mitchison, 1997, Seligmann and Twelves, 2013).

1.2 Microtubules: A detailed view on their structure, dynamics and regulation

1.2.1 Protofilament arrangements in a MT

MTs form cylinders that consist of protofilaments, non-covalent longitudinal arrangements of tubulin heterodimers (**Fig.2a**). Each heterodimer accounts for a length of ~ 8 nm within a protofilament. *In vivo*, typically 13 of these protofilaments arrange into a MT. MTs with protofilament numbers different from 13 only account for ~20 % and consist mainly of 14 protofilaments. In contrast, protofilament numbers between 10

and 16 have been reported for MTs assembled *in vitro* from purified brain tubulin under various conditions with the 14 protofilament form being the most abundant species (Chretien et al., 1992, Ray et al., 1993). MTs can switch protofilament numbers during growth resulting in MTs with mixed protofilament numbers. Both loss and gain of protofilaments has been observed *in vitro* and in *Xenopus laevis* egg extract (Chretien et al., 1992, Vitre et al., 2008). Switches in protofilament number might be linked to dynamic properties of MTs (See below; section 1.3.4).

For a 13 protofilament MT, the major *in vivo* configuration is called B lattice as depicted in (**Fig.2c**) (Desai and Mitchison, 1997). The majority of lateral contacts is represented by α- α tubulin interactions and β – β tubulin interactions except for the seam, were α and β tubulin are next to each other. Longitudinal contacts are thought to be stronger than lateral contacts (Castle and Odde, 2013, Muller-Reichert et al., 1998).

Each protofilament exhibits intrinsic polarity with α-tubulin exposed at one end (called the "minus end") and β-tubulin exposed on the other end (called plus end). As a consequence, the entire MT has a polarity (Mitchison, 1993).

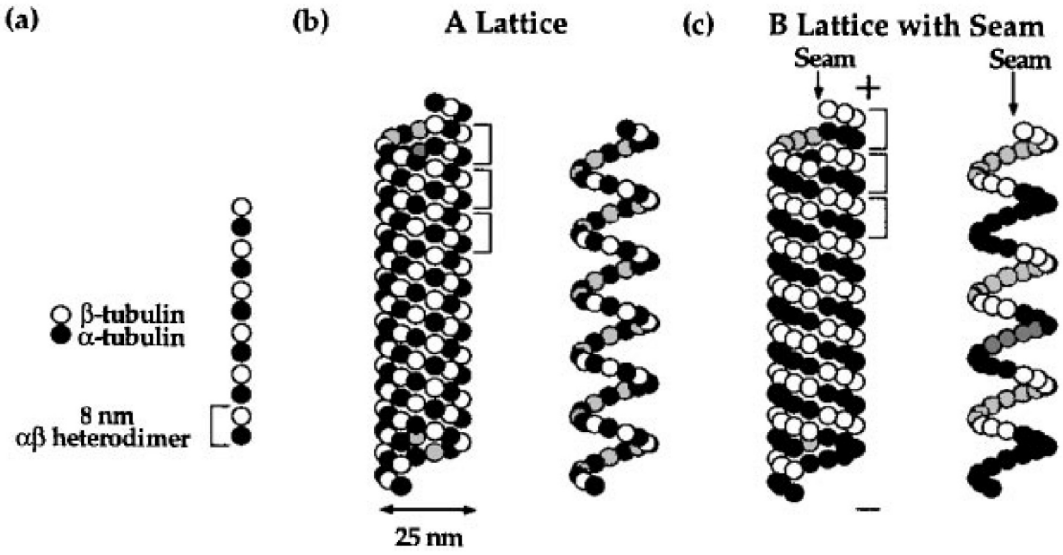

Figure 2: Scheme of 13 protofilament MT architectures

(**a**) Head to tail interaction of α and β tubulin in a protofilament. (**b**) Scheme of an A lattice configuration (left) and a single 3 start helix to visualize adjacent monomer contacts as a visual aid (right). (**c**) MT B lattice conformation, the predominant form *in vivo*. The majority of lateral interaction occurs between α and α tubulin and β and β tubulin respectively, except for the seam, where α tubulin and β tubulin form lateral contacts. (from (Desai and Mitchison, 1997))

Tubulin dimers within MTs and protofilament sheets adopt a rather straight conformation (Wang and Nogales, 2005, Fourniol et al., 2010). In contrast, several lines of evidence suggest that the solution structure of tubulin has an overall curvature of approximately 12 ˚ (see below and (Barbier et al., 2010, Gigant et al., 2000, Ravelli et al., 2004, Rice et al., 2008).

1.2.2 Tubulin – the subunit of MTs

α and β tubulin form a stable hetero dimer that polymerizes spontaneously into MTs *in vitro* in the presence of GTP but not GDP (Olmsted and Borisy, 1975). The tubulin heterodimer was originally identified as a protein that strongly binds to the mitosis inhibitor colchicine and GTP (Borisy and Taylor, 1967, Shelanski and Taylor, 1967, Weisenberg et al., 1968). Both, α and β tubulin can bind GTP. α tubulin lacks appreciable hydrolysis activity and nucleotide turnover is slow with a half-life time of ~33 hours (Spiegelman et al., 1977). In comparison, nucleotide exchange in β tubulin is fast (reaction half-life of a few seconds (Brylawski and Caplow, 1983, Amayed et al., 2000) and its affinity for GDP and GTP is in a similar concentration range (~10 $10^6 M^{-1}$ for GTP and ~5 $10^6 M^{-1}$ for GDP tubulin) at physiological Mg^{2+} concentrations (Mejillano and Himes, 1991, Ebel and Gunther, 1980). In solution, β tubulin exhibits appreciable GTP hydrolysis activity (1.7 nM/sec at 10 μM tubulin; (Carlier et al., 1984)). The hydrolysis rate increases up to 50 fold once MT polymerisation starts i.e. incorporation of tubulin into a MT stimulates the intrinsic hydrolysis rate (Vandecandelaere et al., 1999).

A crystal structure of tubulin on its own is not available but co-crystals in complex with a stathmin domain RB3-SLD (called T2R, (Gigant et al., 2000)), an artificially engineered tubulin binder (DARPin, see results, chapter 4) and a mutagenized tubulin binding domain (Ayaz et al., 2012) have been reported. The overall structure (**Fig.22b**) revealed that α and β tubulins adopt rather globular conformations and form a dimer in which the two proteins exhibit a curvature of ~ 12˚ relative to each other. The degree of curvature is very similar between tubulin in which GTP or GDP is bound to β tubulin (Nawrotek et al., 2011).

1.2.3 Tubulin nucleation – birth of new MTs

MT nucleation is the process where soluble tubulin dimers assemble into a new MT.
The intracellular tubulin concentration has been measured in *Xenopus laevis* oocytes and was typically in the range of 10 – 15 μM (Gard and Kirschner, 1987). In the absence of specific templates, no considerable nucleation has been observed in extracts from these oocytes or at similar tubulin concentrations *in vitro* (buffer), unless nucleation enhancing agents were added (Gard and Kirschner, 1987, Vandecandelaere et al., 1999). This allows cells to control MT nucleation in space and time due to mechanisms that trigger MT nucleation only at sites where MTs are needed and forms the first layer of regulation for an organized MT array (Teixido-Travesa et al., 2012, Dogterom and Surrey, 2013).
MT can nucleate and grow from specialized templates, usually γ-tubulin containing microtubule organizing centres (Brinkley, 1985, Bornens, 2012). Similarly, a specialized structure at the basis of cilia (MT based structures important for cell motility of several cell types and important for several forms of perception (Kim and Dynlacht, 2013)) forms a template for MT nucleation defining the 9 fold symmetry of the MT array in these structures (Kitagawa et al., 2011).
MT can also branch from existing MTs which means that a new MT nucleates from the lattice of an existing MT. The new MT nucleates at a low branch angle and maintains the polarity of the "mother MT". MT branching does not readily occur *in vitro* and several proteins such as Augmin, Ran and TPX2 have been shown to be required for this process. It has been proposed that branching is utilized particularly during mitosis to generate many MT with identical polarity (Petry et al., 2013).
Another set of new MTs is generated in the absence of specific template structures. MT nucleation from pure tubulin is readily observed *in vitro* at higher concentration and its efficiency is concentration dependent (Vandecandelaere et al., 1999). In cells, local concentrations of tubulin available for nucleation and polymerization are controlled by sequestering proteins such as stathmin/op18 (Belmont and Mitchison, 1996, Rubin and Atweh, 2004). Stathmin binds two tubulin dimers (as shown in **Fig.22b**) and prevents their nucleation and their incorporation into MTs (Steinmetz, 2007, Gigant et al., 2000). Stathim has several phosphorylation sites which modulate the affinity to tubulin (Manna et al., 2009, Steinmetz, 2007). Studies in *Xenopus laevis* spindles identified a

phosphorylation gradient of Stathmin with the highest degree of phosphorylation in the spindle itself. The tubulin-stathmin affinity increases with distance away from the spindle and thereby allows MT nucleation within the spindle but prevents it further away from the spindle where MT are not needed at this stage (Fuller, 2010, Niethammer et al., 2004) .

Additionally, several proteins have been identified that favour MT nucleation in solution (Brunet et al., 2004, Moores et al., 2006, Lazarus et al., 2013). Some of them are involved in the so called Ran-GTP pathway. Nucleation factors are thought to bind to Importins. After Ran activation due to nucleotide exchange, nucleation factors are displaced from importing by Ran-GTP and become active, facilitating local nucleation of new MTs (Caudron et al., 2005, Halpin et al., 2011, Fuller, 2010).

Coordinated regulation of these three pathways for the generation of new MTs in cells allow for very precise control of nucleation in time and space which marks the initial step in the formation of higher ordered MT arrays (Dogterom and Surrey, 2013).

1.2.4 GTP triggered MT growth

MT predominantly grow by addition of GTP bound tubulin heterodimers to their ends, although occasional GDP-tubulin incorporation into already existing MTs has been reported when GTP-tubulin and GDP-tubulin were mixed (Valiron et al., 2010). While it is clear that GTP hydrolysis is the energy source for MT dynamic instability, the question of how GTP binding transforms non-polymerizable tubulin into polymerization competent tubulin dimers has been a debate for a long time and is still not fully understood.

The first high resolution structure of unpolymerized GDP-tubulin has been called T2R (two tubulin dimers in complex with a Stathmin domain), where the tubulin dimer is curved while it is straight in a microtubule (Lowe et al., 2001, Wang and Nogales, 2005, Gigant et al., 2000, Ravelli et al., 2004, Nawrotek et al., 2011).The idea has been proposed that GTP would pre-straighten a tubulin dimer and would thus make it polymerization competent (Muller-Reichert et al., 1998, Howard and Hyman, 2009).This idea was mainly based on the observations with GMPCPP, which has been proposed to be a GTP mimic with very slow hydrolysis kinetics. GDP/GTP and

GMPCCPP MTs were depolymerized by rapid temperature shifts and the addition of calcium (a MT destabilizer, (O'Brien et al., 1997)) and observed by electron microscopy. At shrinking ends, pronounced outward curling of protofilaments could be detected (**Fig.3d**), which fragmented into oligomeric structures derived from single protofilaments, in which tubulin dimers formed longitudinal but not lateral bonds. These oligomers exhibited a pronounced curvature. A comparison of the degree of curvature revealed that GDP protofilament oligomers are more curved as compared to the GMPCCP protofilament oligomers (Muller-Reichert et al., 1998, Wang and Nogales, 2005), which was the basis for the idea in which GTP binding would "pre-straighten" a tubulin dimer. More recent data however challenged this idea. A recently reported high resolution crystal structure for tubulin in complex with RB3-SLD (T2R) in the presence of GTP or GDP did not observe any evidence for pre-straightening and the overall structures were very similar (Nawrotek et al., 2011). However, a possibility remained that RB3-SLD (Stathmin domain) would force tubulin into a curved conformation. Biophysical and biochemical studies support the notion that GDP and GTP tubulin are similarly curved in solution in the absence of RB3-SLD: Small angle light scattering experiments of tubulin in the presence of GTP and GDP did not detect appreciable differences in their overall structure, in good agreement with the reported crystal structures (Rice et al., 2008). In addition, small molecules that have been shown to bind tubulin at the curved dimer interface do not discriminate between GTP and GDP tubulin, which further argues against a pronounced pre straightening (Barbier et al., 2010). Taken together, these data argue against a pre straightening idea and suggest that tubulin adopts a curved conformation in solution when bound to GDP or GTP.

However, this notion does not explain why GTP tubulin polymerizes into MTs. *Nawrotek* and co-workers proposed that more subtle changes would be responsible for the polymerization potency of tubulin and that these changes are facilitated but not triggered by GTP (see section 4.3 for a more detailed discussion about this topic)(Nawrotek et al., 2011).

1.2.5 The GDP MT lattice is an intrinsically unstable structure that depolymerizes unless stabilized by a cap

Tubulin preferentially adds onto MT ends in its GTP bound state which activates GTP hydrolysis kinetics within β tubulin. GTP hydrolysis in a MT is essentially irreversible. As a consequence, the majority of a MT lattice is composed of GDP tubulin (Stewart et al., 1990, Vandecandelaere et al., 1999). GDP MT plus ends are intrinsically unstable and depolymerize via outward curling protofilaments (**Fig.3d**) unless they are protected by a GTP-Cap at their ends which is constantly renewed by newly incorporated GTP-tubulin subunits during MT growth (Walker et al., 1989, Tran et al., 1997, Drechsel and Kirschner, 1994, Muller-Reichert et al., 1998, Caplow and Shanks, 1996). The intrinsic instability of GDP MTs is thought to derive from the tendency of GDP-tubulin dimers to "flip back" into their curved solution structure. Lateral and longitudinal contacts between neighbouring tubulin subunits counteract this force which maintains the rather straight tubulin conformation within a MT. Mainly lateral contacts are thought to be weakened as a consequence of GTP hydrolysis: In this view, stronger lateral contacts within the GTP cap keep the MT together but once the stabilizing cap is lost, lateral contacts in terminally exposed GDP tubulin subunits would not be strong enough to counteract the intrinsic tendency of tubulin dimers to adopt their energetically favourable solution structure, resulting in overall depolymerisation of a MT. Several lines of evidence support this view:

The M-loop is a structural feature of tubulin that mediates lateral inter-dimer interactions. This loop is structured within MTs but not in soluble tubulin dimers. A recent study identified the mechanism of the MT stabilizing drugs Epothilone A and Zampanolide that bind to the taxaene pocket which results in a structured M loop of tubulin, even in uncomplexed soluble tubulin. The authors reasoned that a structured M loop could be important for lateral interaction which would explain why drugs targeting the taxaene pocket favour MT nucleation and stabilize existing MTs, even in the absence of a GTP cap (Prota et al., 2013).

GTP analogues have been widely used to study MTs. GMPCPP is an essentially non hydrolysable GTP analogue and GMPCPP tubulin conformations are thought to be a mimic of GTP tubulin conformation. A comparison of GDP and GMPCPP MTs indicated a more straight conformation of GMPCPP tubulin within a MT (Hyman et al.,

1992). In their depolymerizing state (induced via low temperatures and destabilizing ions) a higher degree of curvature was observed for outward curling GDP protofilaments as compared to protofilaments from depolymerizing GMPCPP MT (Muller-Reichert et al., 1998, Wang and Nogales, 2005). Both findings could mean that GDP tubulin dimers in a MT might have a higher tendency to "flip back" to the curved conformation than GTP tubulin.

Another essentially non hydrolysable nucleotide analogue is GTPγS, that potentially mimics an early hydrolysis transition intermediate. GTPγS MT do not have catastrophes (Maurer et al., 2011, Maurer et al., 2012, Scheffers et al., 2000). A comparison between GDP MTs and GTPγS MTs by electron microscopy (in the presence of the associated proteins doublecortin and monomeric Mal3, respectively) revealed additional lateral densities between tubulin dimers in the GTPγS state, suggesting stronger lateral interactions. This might explain the absence of catastrophes in the GTPγS case. However, it should be noted that these comparisons come from experiments in the presence of different proteins, which could also affect the MT lattice structure (Maurer et al., 2012, Fourniol et al., 2010)). MT stabilization has also been reported for beryllium fluoride and aluminium fluoride that are thought to mimic a late GTP hydrolysis states or a GDP+Pi state (Carlier et al., 1989).

Taken together, these studies suggest that lateral interaction strength between tubulin subunits in the MT end region and the tendency of tubulin dimers to switch between a straight into a curved conformation are the main determinants that define MT stability. The stabilizing end structure is not necessarily GTP tubulin as hydrolysis intermediate states might also be of stabilizing nature.

A more detailed view of the MT plus end morphology

Several studies focused on the morphology of MT plus ends. While growing MT ends in yeast are rather blunt/flared (Kukulski et al., 2011), MT ends in mammalian cells exhibit a high degree of "tapering" (**Fig.3**) i.e. different lengths of protofilaments at MT ends, often resulting in sheet like arrangements of a few protofilaments prior to full tube closure (Zovko et al., 2008).

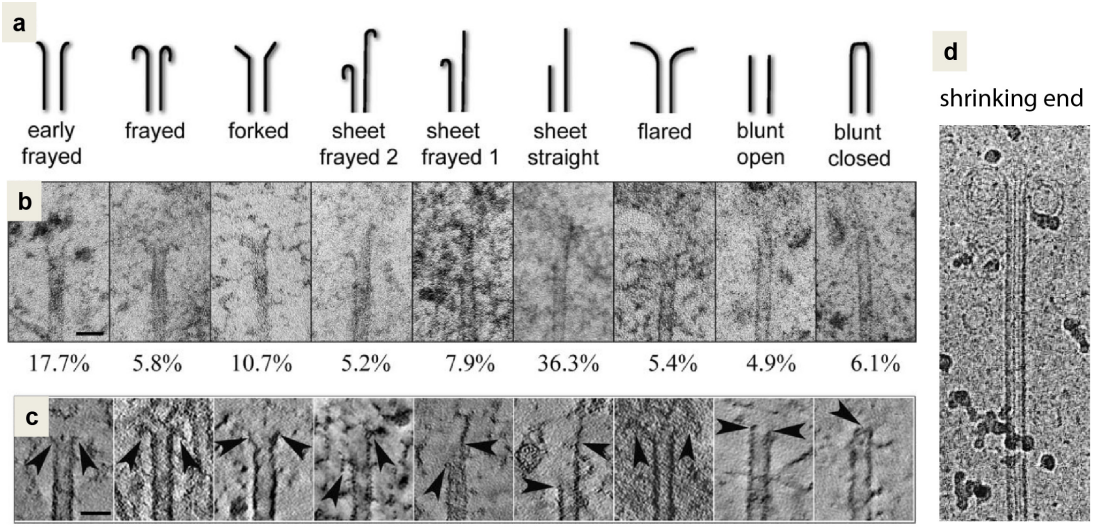

Figure 3: Morphology of MT plus ends

(**a**) Cartoon representation of different MT end morphologies. (b) Electron micrographs of the corresponding MT plus end morphologies in mouse fibroblasts and (**c**) tomographical slices of 5 nm thickness of corresponding MT plus end structures in mouse fibroblasts. Numbers indicate the relative abundance of each structure in per cent. Scale bar: 50 nm. This illustration was taken from (Zovko et al., 2008) (**d**) EM micrograph of a depolymerizing MT end. Taken from (Muller-Reichert et al., 1998).

In vitro studies showed that the degree of tapering increases with time of polymerisation ("with age") and growth speed of MTs (Chretien et al., 1995, Coombes et al., 2013). This agrees well with the *in vivo* data as MT growth rates in yeast are generally slower as compared to vertebrate systems (Tanaka et al., 2005, Gard and Kirschner, 1987).

The reason for tapering is not intuitive at first. In a blunt MT end, all terminal tubulin dimers form three contacts: two lateral contacts and one longitudinal. In a tapered end, terminal tubulin subunits are engaged in one longitudinal and zero, one or two lateral contacts. Thus the average off rate for tubulin dimers is expected to be higher in tapered end structures (Gardner et al., 2011a). In turn, this should prevent tapering due to higher off rates of tubulin subunits of longer protofilaments. In order to understand the existence of tapered ends, one needs to take diffusion and the geometry of MT ends into account. In a blunt MT tubulin subunits can add onto the end from solution. In a tapered end, the volume from which new tubulin dimers can arrive to a lagging protofilament is reduced, because leading filaments or sheets block tubulin dimer arrival from one side (Castle and Odde, 2013).

On-rate and off-rate are therefore reduced at lagging protofilaments. A recent study simulated these two opposing effects by using available diffusion coefficients for tubulin. Their simulation indeed recapitulated tapered end structures (Castle and Odde, 2013).

End structures might have large impact on MT dynamic (see below section 1.3.4) and some evidence suggest that proteins can modify these end structures to control MT behaviour (Vitre et al., 2008).

1.3 Dynamic instability of MT plus ends

1.3.1 The GTP cap hypothesis

MTs switch between a slow growing phase and a rapid shrinking phase, termed dynamic instability. The transition from a growing to a shrinking end is called a catastrophe and the transition from a shrinking to a growing MT ends is termed rescue (Mitchison and Kirschner, 1984, Horio and Hotani, 1986). MT Dynamic instability is utilized for efficient space exploration, allows the MT cystoskeleton to rearrange in response to various triggers and directly generates forces (Desai and Mitchison, 1997, Volkov et al., 2013). Its importance is best shown by the potency of mitosis inhibitors such as nocodazol, that block cell division at nM concentrations by altering MT dynamicity without obvious effects on the overall MT polymer mass (Jordan et al., 1992, Vasquez et al., 1997). MT dynamicity is tightly controlled and can be quickly adapted to changing environments or during changes in the cell cycle. *Saxton et al.* microinjected florescent tubulin into cultured cells and measured the time until florescent tubulin was incorporated into MTs. Incorporation was much faster for mitotic cells as compared to interphasic cells, which clearly demonstrated that MT dynamicity is under the control of the cell cycle and greatly enhanced during mitosis (Saxton et al., 1984).

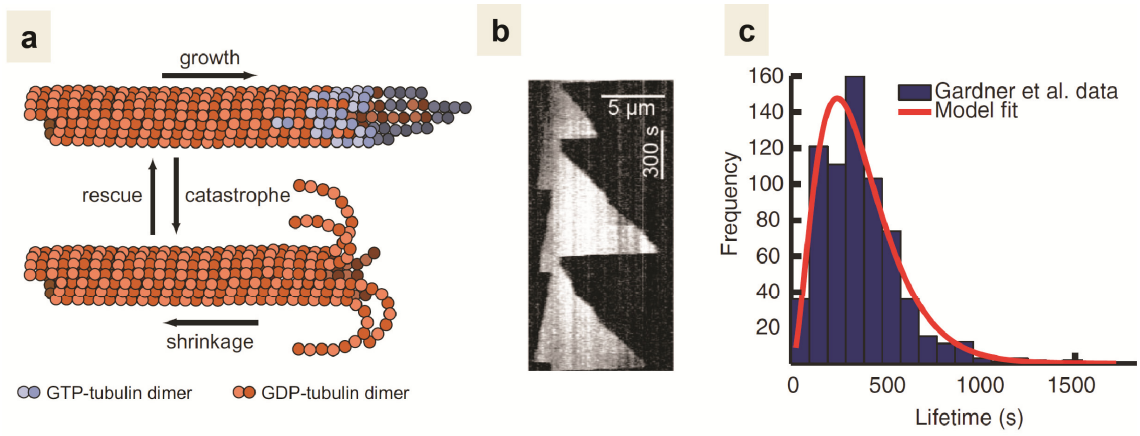

Figure 4: MT dynamic instability

(**a**) MTs switch between growing phases in which the end is protected by a stabilizing end structure and shrinking phases in which the stabilizing end structure is lost. The transition from a growing to a shrinking MT is called catastrophe and the reverse process a rescue.(**b**) Time space plot (kymograph) of MT dynamic instability observed *in vitro* by DIC microscopy. The MT grows from a stabilized GMPCPP seed. Slow growth phases are alternating with rapid shrinking phases. The faster growing end is the plus end (right) and the slower growing end is the minus end (left). (**c**) MT life time distribution of MTs polymerized *in vitro* and a model fit with a gamma function shaped curve, as specified in (Bowne-Anderson et al., 2013). Images are taken from (Bowne-Anderson et al., 2013).

Mainly GTP tubulin but not GDP tubulin polymerizes into MTs and studies with radioactively labelled GTP revealed that the vast majority of a MT consists of GDP tubulin (Stewart et al., 1990). The idea of a protective GTP cap at MT ends was formulated and many experiments supported this idea. MTs were cut by UV beams to generate ends without stabilizing end structure; as predicted from GTP cap hypothesis, GTP cap free MT plus ends immediately started to depolymerize (Walker et al., 1989, Tran et al., 1997).

Experiments with GMPCPP-tubulin showed that a single layer of non-hydrolysable tubulin dimers at MT ends is sufficient to stabilize them against dilution induced depolymerisation, indicating that the GTP cap can in principle be small (Drechsel and Kirschner, 1994, Caplow and Shanks, 1996). However, when MT growth fluctuations were analysed with enhanced spatiotemporal resolution, short shrinking episodes of up to 40 nm that did not lead to catastrophes were observed, incompatible with an average stabilizing structure of only 1 layer (8 nM) of tubulin dimers (Schek et al., 2007).

Estimates for the length of the stabilizing end structure range from a single layer of GTP tubulin (Caplow and Shanks, 1996) up to 60 layers of tubulin (Seetapun et al., 2012) and the exact nature of the stabilizing end structure is still under debate.

1.3.2 Relationship between free tubulin, growth speeds and catastrophes

MT growth speed but not MT shrinking speed scales with tubulin concentrations. Catastrophe frequency decreases at higher tubulin concentration where rescues are more often observed (Walker et al., 1988), in favour of an intuitive idea where the length of the stabilizing end structure increases at higher growth speeds.

In contrast, when MTs were grown at various tubulin concentrations and were diluted below the critical concentration (cc, where no net growth of filaments exists), no correlation between initial growth speed and delay time until catastrophe onset was observed (Walker et al., 1991, Voter et al., 1991).The authors proposed that the GTP hydrolysis rate might scale with the growth speed of MTs. However, EB proteins (End Binding proteins, see below in section1.6.1) that recognize nucleotide dependent conformations at MT ends form more extended comet like structures at MT ends at higher growth speeds (Bieling et al., 2007, Maurer et al., 2011) arguing against a strict coupling between MT growth speed and GTP hydrolysis rate.

To know the dependence between MT growth rate, GTP hydrolysis associated transition kinetics and MT stability would greatly improve our understanding of MT dynamics in order to explain these counter intuitive observations.

1.3.3 MT plus ends “age” with time

Younger MTs have a lower probability to undergo catastrophe as compared to older MTs, often called “MT aging” (Odde et al., 1995, Gardner et al., 2011b, Mohan et al., 2013). Essentially, younger MTs are also shorter than older/younger MTs and it is not clear if the destabilizing element is linked to the actual age or the increased length of a MTs.

Consequently, MT life time distribution of plus ends at steady state cannot be described by a simple exponential distribution (Odde et al., 1995, Gardner et al., 2011b) (**Fig.4c**). Instead, it can be well fitted with a convolution of exponential distributions (e.g. gamma distribution), which lead to the proposal that MT catastrophe is a multi-step process (Odde et al., 1995, Gardner et al., 2011b). The underlying mechanism for aging is still under debate (see the following section) and experiments are needed that distinguish between different possibilities in order to explain this phenomenon.

1.3.4 What is the mechanism of MT plus end dynamic instability?

Dynamic instability has been described more than 25 years ago but its mechanism is still not fully understood. Several ideas have been proposed for the underlying mechanism of catastrophe induction.

A complete description of catastrophe induction has to cover the following experimentally observed features: They have to predict that (1) higher tubulin concentrations lead to higher growth speeds, (2) the catastrophe frequency decreases with higher tubulin concentrations but that at the same time (3) the delay time until catastrophe after tubulin removal is independent of the initial growth speed at the time point of dilution; and (4), it further has to predict the reported aging phenomenon. Additionally, nano-scale parameters such as rapid assembly kinetics and growth fluctuation at MT ends and the impact of the MT ends structure would be needed for a complete description of MT dynamic instability

The main ideas that more or less withstand this challenge are summarized.

Up to date, the model that fits experimentally observed values of MT plus end dynamics best is a "defect accumulation" model (Bowne-Anderson et al., 2013). It assumes irreversible and discrete defects that accumulate over a growth episode and destabilize a MT (**Fig.5a**). More specifically, protofilament loss has been hypothesised as a cause of dynamic instability: Whenever the terminal GTP bound subunit detaches and the former sub terminal newly exposed tubulin is in its GDP state, this particular protofilament stops to grow and is lost. A loss of three protofilament would cause a catastrophe. So far, this model fits best to all experimental observation because it predicts (1&2) the dependency of tubulin concentration and catastrophe frequency and growth speed, (3) a gamma distribution like shape of MT life time distributions (**Fig.4**) and (4) the observed data from tubulin dilution experiments. While the rate constant for the detachment of the terminal subunit is constant, the probability of the sub terminal tubulin dimer being in a GTP state scales with tubulin concentration. At higher tubulin concentrations, the step time between arriving tubulin dimers is reduced, effectively lowering the detachment probability of a terminal GTP-tubulin once incorporated. Higher tubulin concentrations therefore decrease the rate of defect accumulation and consequently the catastrophe frequency. A young MT has on average fewer defects compared to an old MT, which would explain the "aging" phenomenon. The catastrophe time after rapid

dilution would be only determined by the number of defects a MT has acquired before dilution and the detachment rate of the terminal GTP bound subunit. Because this detachment rate is slow in comparison to the hydrolysis rate of sub terminal tubulin dimers, the hydrolysis rate can be neglected in the dilution case. Effectively, the number of defects acquired prior to dilution would solely define the waiting time until catastrophe after dilution because the detachment rate of terminal tubulin subunits is constant and the hydrolysis rate negligible. Therefore initial growth speed and waiting times until catastrophe after dilution do not correlate.

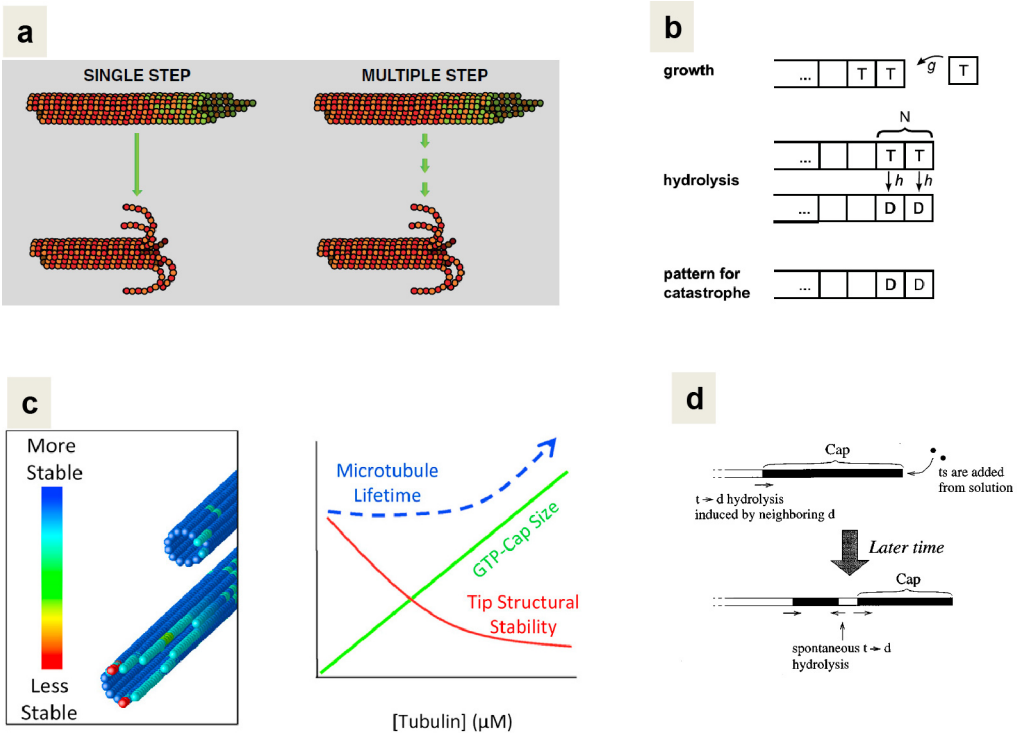

Figure 5: Schematic overview of current dynamic instability models

(**a**)Irreversible defects (called steps) are accumulated during MT growth. A step parameter of 3 did fit experimental data best and it was hypothesized that 3 defects have to occur until the MT starts to depolymerize. From (Bowne-Anderson et al., 2013) (**b**) In the model of longitudinal coupling, T (GTP) and D (GDP) states exist and the coupling parameter N defines, how many D subunits have to be in a row at a MT end of one protofilament for catastrophe induction. An example for N=2 is shown. From(Brun et al., 2009) (**c**) The tapering model assumes that increased tapering at MT ends leads to decreased stability (left lower) whereas blunt MT ends (left, upper) are more stable. The GTP-Cap scales with tubulin concentration/growth speed and is independent of age. Because tapering increases over time, MT stability decreases over time From.(Coombes et al., 2013) (**d**) In the lateral crack model, a stabilizing GTP cap is present at MT ends that scales with tubulin concentration/growth speed. However, "cracks" within the GTP cap create new hydrolysis fronts that shorten the functional GTP cap, because the GTP tubulin subunits "behind" the cracks do not stabilize the MT end. Cracks occur stochastically and randomly. From (Flyvbjerg et al., 1996).

Brun et al tested an alternative model in which a "coupling parameter" was introduced where a row of N (1,2,3..) GDP tubulin dimers at the end of one protofilament would induce a catastrophe (**Fig.5b**) (Brun et al., 2009); similar ideas of coupling have been also studied in (Padinhateeri et al., 2012). The model further assumes random and uncoupled hydrolysis of GTP nucleotides within the MT. While N=1 (one GDP at a protofilament end causes catastrophe) does not agree well with experimental data, N=2 (two GDP in a row at a protofilament end cause catastrophe) qualitatively recapitulates the MT life time distribution and reproduces the observation that initial growth speed and delay times until catastrophe after rapid dilution do not correlate well. However, the actual numbers do not fit well with experimentally observed numbers. Lateral bonds break before longitudinal bonds while MT depolymerize. Therefore a lateral coupling might be a more realistic approach. In any case, the model shows that such coupling in principle explains the available data as well, without having to assume hypothetical defects.

"Aging" at steady state could also be explained by the following assumption: The GTP cap fluctuates around an average value and if the GTP cap density or length is low, catastrophe occurs. This could be the GTP tubulin density at a certain MT end position or the GTP/GDP distribution in longitudinal direction within a single protofilament. MTs with a longer growth history have increased lengths and also a higher probability of a more pronounced tapering at their ends (Chretien et al., 1995, Castle and Odde, 2013, Coombes et al., 2013). In a blunt MT end, all terminal tubulin dimers form three contacts: two lateral contacts and one longitudinal. In a tapered end, terminal tubulin subunits are engaged in one longitudinal and zero, one or two lateral contacts. Thus the average off rate for tubulin dimers is expected to be higher in tapered end structures (Gardner et al., 2011a). Therefore, catastrophe probability increases with time, which would explain the observed MT life time distributions (**Fig.5c**).

Historically, the first model that could explain the dilution experiments and the reduced catastrophe frequency at higher tubulin concentrations was postulated by (Flyvbjerg et al., 1994, Flyvbjerg et al., 1996) and co-workers. In their model, GTP hydrolysis does not scale with MT growth velocity but "lateral cracks" stochastically generated new hydrolysis fronts within the GTP cap, stochastically shortening the effective stabilizing end zone (**Fig.5d**). More recently, this model has been refined (Margolin et al., 2012).

However, the existence and nature of these lateral cracks is difficult to prove experimentally and the model does not explain the aging phenomenon.
Several possible scenarios of MT dynamic instability exist but experiments that clearly distinguish between these models are elusive.

1.4 Dynamic instability of MT minus ends

Minus ends differ from plus end in many aspects. Instead of β tubulin, α tubulin is exposed at the minus end (Mitchison, 1993). They also exhibit dynamic instability behaviour *in vitro* but are generally less dynamic and growth speeds are approximately three times slower as compared to plus ends at identical tubulin concentrations. *In vivo*, MT minus ends are often even less dynamic as they are "caped" which inhibits their growth and shrinkage (Dammermann et al., 2003, Goodwin and Vale, 2010)
In vitro, EB proteins that bind nucleotide dependent conformations at growing MT ends bind with similar affinity to growing plus ends and minus ends (Bieling et al., 2007, Bieling et al., 2008a). Similar to plus ends, also minus ends shrink with a delay after tubulin dilution, suggesting a similar dynamic instability mechanisms for minus ends and plus ends (Walker et al., 1991). However, minus ends –in contrast to plus ends- do not immediately depolymerize after laser cutting, a still poorly understood phenomenon which marks an interesting difference between the two ends. (Walker et al., 1989, Tran et al., 1997). Interestingly, MT minus ends do not exhibit a strong aging phenomenon and the life time distribution of minus ends can be well fitted with a single exponential distribution (Odde et al., 1995), suggesting more pronounced differences in the nature of end dynamics between MT plus ends and minus ends.

1.5 Rescues

A shrinking MT can either depolymerize completely and disappear or can switch back to a growth phase, called a rescue. Similar to catastrophes, rescues are an intrinsic property of MT dynamics and can be observed *in vitro* in the absence of additional proteins (Walker et al., 1988).
The underlying mechanism is not well understood. The most popular view is that GTP remnants within the MT lattice form stable rescue points due to non-hydrolysed GTP

islands (Dimitrov et al., 2008, Tropini et al., 2012), possibly due to tubulin isoforms with altered hydrolysis kinetics (Bhattacharya et al., 2011). Alternatively, loss of protofilament spots might mark rescue points. When the overall MT switches from 14 to 13 protofilaments the one lagging protofilament might still be able to bind GTP tubulin from solution from which rescues might occur (Gardner et al., 2013). This idea is vaguely supported by the observation that rescue frequency increases mildly with tubulin frequency (Walker et al., 1988), as higher tubulin concentrations would result in a higher on rate of GTP tubulin to this lagging protofilament.

Cytoplasmic Linker-Associated Protein (CLASP) has been identified as a rescue factor (Akhmanova et al., 2001). CLASP is thought to catalyse the addition of tubulin dimers to a shrinking MT thus enhancing the rescue frequency (Al-Bassam et al., 2010).

Despite considerable progress in understanding MT dynamics of plus ends and minus ends, many unanswered questions regarding the mechanism of this fundamental cellular process remain.

1.6 Functions of MT dynamics

Microtubule dynamics is crucial for many different reasons. Microtubule dynamics increases drastically at the onset of mitosis which enables fast reorientation of the interphase MT array into the spindle (Saxton et al., 1984). Spindle formation relies on localized MT nucleation near the cromosomes and their arrangement into a bipolar structure by motor proteins and other MAPs. Another complementary pathway is called the “serach and capture” pathway where highly dynamic MT plus ends emenate form centrosomes that get stabilized only, when a stable link to chromosomes is formed. Fast dynamics are important because MT that “miss a chromosome” need to shrink and regrow in order to be able to make a stable contact with a chromosome(Wittmann et al., 2001).

MT dynamics in spindles is important to directly generate forces that (a) centre the genetic material in the metaphase plane and (b) pull the chromosomes apart at later stages of mitosis(Grill et al., 2003).

The metaphase spindle exhibits “flux” which means that MT constantly polymerize at plus ends and depolymerize at their minus ends while motor proteins slide antiparallel MTs apart(Loughlin et al., 2010).

In some cases, specific sets of MTs get stabilized selectively. This is the case in long axons of neurons and is belived to be caused by posttranslational tubulin modifications such as acetylation or glutamylation (Janke and Kneussel, 2010). MT stabilization can occur specifically at the leading edge of migrating cells; Here, Phosphatidylinositol (3,4,5)-triphosphate inactivates GSK3β which promotes binding of CLASP to EBs and MTs which selectively stabilizes MTs near the leading edge of migrating cells (Kumar et al., 2009, Duellberg et al., 2013).
Another important function of MT dynamic instability is to shape cell compartments. For instance, the ER transmembrane protein STIM1 binds directly to EB1. The ER membrane is then dragged along the path of growing MTs which shapes the three dimensional arrangement of this compartment (Pozo-Guisado et al., 2013).

1.7 Regulation of MT properties by MAPs

MT dynamic instability is an intrinsic property of MTs but its parameters need to be adjusted depending on the specific task of an MT. For instance, MT dynamicity is enhanced during mitosis as compared to interphase. Within the same cell some MT can be specifically stabilized such as kinetochore MTs, MTs in antiparallel overlaps during anaphase or MTs within the leading edge during cell migration and differentiation (Duellberg et al., 2013). In addition to MT dynamics, their arrangement in space and time needs to be controlled. At similar MT concentrations, MT growth velocities are generally faster in cells as compared to pure *in vitro* systems, which is mainly attributed to MAPs (Gard and Kirschner, 1987, Amos and Schlieper, 2005).
Within the next sections, the main activities that control MT dynamics and their spatiotemporal arrangement are introduced.

1.7.1 +TIPs control MT dynamics, link MT to cellular structures and control their spatial organization

Plus end tracking proteins (+TIPs) comprise a heterogeneous group of proteins that accumulate at growing MT ends where they regulate MT dynamics, regulate their spatial arrangement and link MT ends to other cellular structures such as the endoplasmic reticulum, the plasma membrane or the actin cytoskeleton (Duellberg et al., 2013).

1.7.1.1 Autonomous +TIPs

Homologues of XMAP215 and EBs (EB1, EB2 and EB3 in mammalian systems) are the only known proteins that accumulate autonomously at growing MT ends *in vitro* and *in vivo*. XMAP215 accumulates at growing and shrinking ends in the absence of other proteins and accelerates MT growth rate *in vitro* and *in vivo*. It acts as a processive polymerase and catalyses tubulin turnover at MT ends (Brouhard et al., 2008, Ayaz et al., 2012, van der Vaart et al., 2011). Despite an interaction of the human homologue of XMAP215 with another +TIP complex (Slain/EB1, (van der Vaart et al., 2011)) it is not clear whether XMAP215 can recruit other proteins to MT ends.

EBs binds autonomously to growing but not to shrinking MT ends *in vitro* and *in vivo*. The domain organization of EBs (**Fig.6**) reflects its two functionalities: The n terminal Calponin Homology domain (CH-domain) recognizes a nucleotide dependent tubulin conformation at MT ends and the c terminal EB homology domain and the acidic flexible tail are needed for the recruitment of other proteins (Duellberg et al., 2013).

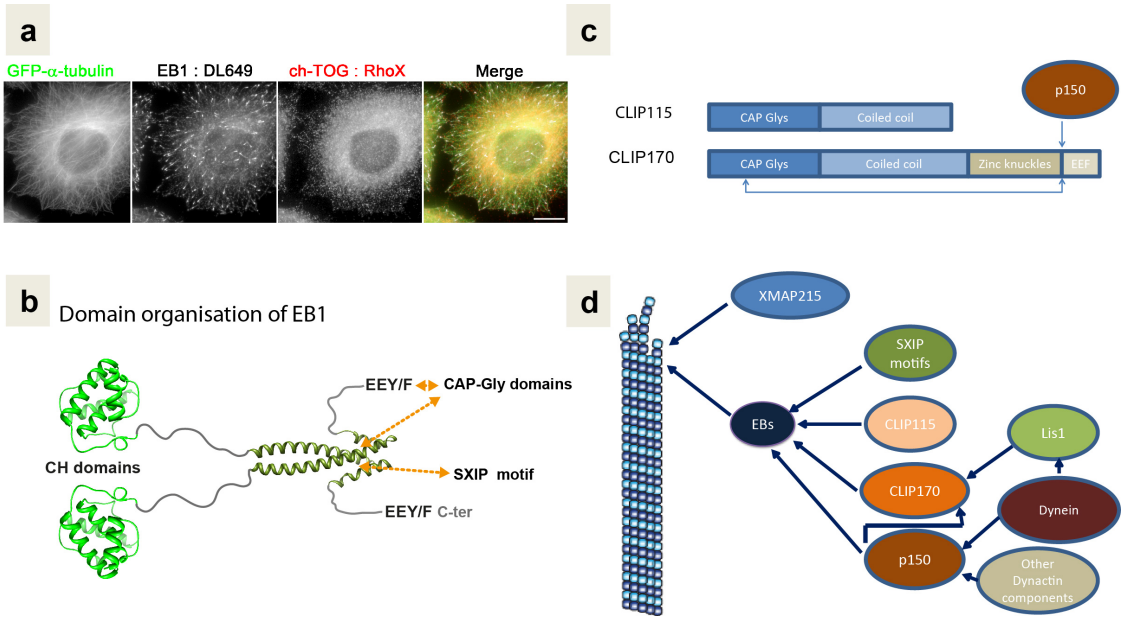

Figure 6: The +TIP network in vertebrate cells

(**a**) Intracellular localization of the autonomous +TIPs EB1 and the human XMAP215 homologue chTOG in HeLa cells, visualized by immunostaining in combination with structured illumination fluorescence microscopy. Merge: green indicates GFP-α tubulin, white indicates EB1 and red indicates ch-TOG. Scale bars: 10 µm. pictures are taken from (Nakamura et al., 2012) (**b**) Domain structure of EB1. The CH domains at the n terminus mediate specific binding to MT end regions, which is followed by a flexible linker. The α helical coiled coil part mediates the formation of a parallel dimer. The EB homology domain and a flexible acidic c terminal tail, ending with the EEY/EEF motif mediate protein-protein interaction. SXIP motifs

bind to the hydrophobic cavity within the EB homology domain. CAP-Gly domains interact with the acidic tail of EBs and potentially with parts of the EB homology domain. Modified form (Duellberg et al., 2013) (**c**) Schematic comparison of CLIP115 and CLIP170. Both proteins have 2 n terminal CAP-Gly domains for EB1/tubulin binding per monomer, followed by a coiled coil domain for dimerization. CLIP170 but not CLIP115 has two c terminal zinc binding domains and an EEF motif per monomer. The c terminus of CLIP170 can bind to the n terminal CAP-Gly domains (resulting in autoinhibition) or mediate binding to p150. (**d**) Simplified scheme of reported interactions between +TIPs.

Cryo EM studies using the CH domain of the fission yeast EB homolog Mal3 showed that the CH domain binds in the groove between protofilaments (except for the seam) contacting 4 neighbouring tubulins. The grove is in very close proximity to the GTP binding pocket where hydrolysis takes place (Maurer et al., 2012).

TIRF microscopy based *in vitro* reconstitution experiment with purified components showed that EBs accumulates at growing MTs independently of additional proteins, where they forms comet like structures. The length of these comets scales with MT growth rate. The turnover of EBs at MT ends is very dynamic with average times of a view hundreds of milliseconds. It was further shown that Mal3 recognizes nucleotide dependent conformations: High affinities have been observed for potential GTP hydrolysis transition state mimics GTPγS and GDP+BeF3- MTs (Bieling et al., 2007, Bieling et al., 2008a, Maurer et al., 2011). Both of these analogues prevent MT catastrophe. In contrast, EBs do not bind strongly to GMPCPP MTs, a potential GTP mimic. It is therefore possible that EBs recognize a GTP hydrolysis transition sate of tubulin (Maurer et al., 2011).

The effect of EBs on MT dynamics and spindle organization has been studied in *Xenopus laevis* egg extract and cell based systems (Komarova et al., 2009, Tournebize et al., 2000) but these data are difficult to interpret because EBs recruit various protein activities to MT ends, including depolymerases and proteins that stabilize MTs (Akhmanova and Steinmetz, 2010). The direct effect could be assessed *in vitro.* EBs on their own increase MT growth velocity and catastrophe frequency, thereby enhancing the overall dynamicity of MTs (Bieling et al., 2007, Komarova et al., 2009, Mohan et al., 2013). Interestingly, Mal3 shortens the length and the life time of its own binding site (life time: length of the binding site region divided by the growth speed of the MT) (Maurer et al., 2011). This suggests that EBs catalyse transition kinetics at MT ends, which would explain why they increase the overall dynamicity of MTs.

1.7.1.2 EB dependent end tracking

The vast majority of +TIPs accumulate at growing MT ends because they are recruited by EBs (Akhmanova and Steinmetz, 2010). All +TIPs studies so far, turn over with fast kinetics at MT ends, similar to EBs (Dragestein et al., 2008, Bieling et al., 2008a). SXIP motifs and Cytoskeleton-associated Protein Glycine-rich (CAP-Gly) domains are the two known signatures that directly bind to the c terminal part of EBs. CAP-Gly domains are roughly spherical domains that interact with the c terminal tail of α tubulin or the very similar c terminal of EBs. Only some of the CAP-Gly domain containing protein are enriched at growing MT ends via EBs, probably because additional and less conserved contacts with the EB homology domain are needed to define specify for EB binding (Duellberg et al., 2013). SXIP motifs are short linear amino acid (aa) sequences within intrinsically disordered protein regions that are flanked by positive charged that bind to a hydrophobic cavity of EBs as depicted in **Fig.6b** and **Fig.15**. (Honnappa et al., 2009a, Buey et al., 2012). If SXIP motifs and CAP Gly domains can simultaneously bind to EBs and how they influence each other is not known but would be important to understand, how +TIPs works as a system (Honnappa et al., 2009a, Kumar and Wittmann, 2012). Several EB-dependent +TIPs interact with each other or recruit additional proteins, giving rise to an even more complex local protein-interaction network at growing microtubule ends (Duellberg et al., 2013).

By now, over 40 +TIPs have been identified that have an SXIP motif but are otherwise unrelated (Jiang et al., 2012). The long list includes destabilizing Kinesin 13 members that enhance catastrophe frequency (Montenegro Gouveia et al., 2010), minus end directed motor proteins from the kineis 14 family important for spatial MT organization (Goshima et al., 2005), proteins like Stim1 or IQGAP that mediate contacts to membrane structures and MACF/ACF7 that binds actin, MTs and EBs (Duellberg et al., 2013).

In contrast, only three EB dependent +TIPs that share a CAP-Gly domain are known. CLIP170 and CLIP115 share very high sequence similarity at their n terminus but CLIP115 lacks the c terminal domain (**Fig.6c**). *In vitro*, CLIP170 binds directly to EBs but a crystal structure could not be achieved yet. CLIP170 accumulates at growing MT ends only in the presence of EB1 but not on its own (Bieling et al., 2008a). The n terminal CAP-Gly domains containing part binds composites of EBs and α tubulin but

also to its own c terminal zinc knuckle domains and the terminal ETF motif, which is very similar to the c terminal tail of EBs. It has therefore been proposed that CLIP170 can switch between an inactive folded back conformation in which c and n terminus bind to each other and an open and active conformation (Lansbergen et al., 2004) (**Fig6b**). Several kinases have been identified that modulate the fraction of activated CLIP170 via direct phosphorylation (Li et al., 2010, Lee et al., 2010). Because CLIP115 lacks the c terminal domain, it cannot adopt an autoinhibited conformation.

P150 is the third known CAP-Gly domain containing +TIP that is found at growing MT ends in various cell types. P150 is a subunit of the dynactin complex, an important regulator of the minus end directed dynein motor complex (see below, section1.6.2). *In vitro* studies with purified components established that p150 and EB1 directly interact with each other (**Fig.6d**) and a co crystal structure between the interacting fragments could be achieved. P150 makes contacts to flexible acidic tail of EBs as well as to the hydrophobic cavity of EBs, in close proximity to were SXIP motifs bind to (Hayashi et al., 2005, Honnappa et al., 2006, Honnappa et al., 2009a). Even though EB1 and p150 can bind directly to each other, EBs are necessary but not sufficient for end tracking of p150 in cells as knock down of EBs as well as knock down of CLIP170 causes loss of p150 enrichment at growing MT ends (Lansbergen et al., 2004, Watson, 2006). The exact mechanism of how CLIP170 contributes to p150 end tracking is not known but potentially involves its c terminal part, that directly binds to p150 (Weisbrich et al., 2007) (**Fig6**).

p150 itself mediates end accumulation of the dynactin complex and is also involved in the enrichment of dynein motors at growing MT ends (Moughamian et al., 2013, Splinter et al., 2012). Mutations within p150 that impair its plus end tracking ability lead to severe neuronal disorders (Farrer et al., 2009, Stockmann et al., 2013) and resulted in perturbed dynein dependent cargo transport from distal neurites (Moughamian and Holzbaur, 2012).

Lissencephaly 1 (Lis1) is another dynein regulator that accumulates at growing MT ends in some cell types. Lis1 is important for dynein activity under high load conditions and mutation in Lis1 one can cause Lissencephaly, a neuronal disorder due to impaired migration of neuronal cells during development (Caspi et al., 2003). End tracking of Lis1 has been implicated in dynein localization in non-neuronal cells (Splinter et al.,

2012, Tanenbaum et al., 2008).In contrast, studies in neuronal cells suggested that Lis1 is not enriched at MT plus ends and its inhibition results in overall impairment of cargo transport that is not specific to neurite ends (Moughamian et al., 2013). This suggests that the +TIP network has specifically evolved for different tissue types to fulfil the different functions of specialized cells.

The +TIP network controls main aspects of MT dynamics, transport along MTs and spatial MT organization. While it is clear that EBs are the master regulator of this complex network, the interdependencies between EB dependent +TIPs are not well understood. A better understanding of the hierarchical structures within this network would be beneficial to understand MT dynamics control by +TIPs and would improve our understanding of the many diseases, that are linked to failures within the +TIP network.

1.7.2 Kinesins and dyneins

MT based motor proteins are mechano-chemical enzymes that couple the energy of ATP hydrolysis to directed motion along the MT lattice. The majority of motile kinesins exhibits plus end directed motility while kinesin 14 members and dyneins are minus end directed (Gennerich and Vale, 2009). So far, the budding yeast kinesin cin8 is the only known motor that can switch its directionality (Roostalu et al., 2011). In addition, non motile kinesin members are known. On example is the kinesin 13 member MCAK, a catastrophe factor (Wordeman and Mitchison, 1995).

Motor proteins arrange MT into higher ordered three dimensional structures (Dogterom and Surrey, 2013) and some of them also influence MT dynamicity (Varga et al., 2006). In concert with other MAPs, kinesins and dyneins are involved in almost all MT dependent processes, which are discussed in the following sections.

Cytoplasmic dynein is a proteincomplex of approximately 1.4 MDa and consists of two identical motor domain containing heavy chain subunits and 5 different additional accessory subunits (Kardon and Vale, 2009). While budding yeast dynein is processive on its own, mammalian dynein seems to be non processive on its own unless it gets activated by cargo binding and/or regulators (Reck-Peterson et al., 2006, Trokter et al., 2012). Many proteins bind directly to the dynein complex and control its properties and localisation (Kardon and Vale, 2009). Dynactin is a multi protein complex that is

important for many dynein functions. Its large subunit (p150 glued) binds directly to the dynein complex via an interaction with the intermediate chain of dynein (Schroer, 2004). Dynactin enhances dynein processivity, is important for dynein targeting to microtubule ends and also mediates interaction with several cargo types (Splinter et al., 2012, Yeh et al., 2012, Schroer, 2004, Ozaki et al., 2011). Dynactin is also essential for dynein mediated removal of cell cycle check point components and normal progression throughout cell division (Ozaki et al., 2011). Other dynein regulators are LIS1 and NDEL1 which are important for dynein function under high load conditions (McKenney et al., 2010).

Many motile kinesins are autoinhibited via a direct association of the tail domain with the motor domain. Regulated cargo binding (often in combination with phosphorylation reactions) can release this autoinhibition which activates motor activity. In addition, posttranslational modification on MTs or MAP decoration of MTs might be an additional layer of kinesin/dynein regulation (Verhey and Hammond, 2009).

1.7.2.1 Motor proteins move cargo along MT tracks

Active intracellular transport is crucial for the correct spatial distribution of various components inside the cell and also for the establishment and maintenance of signalling gradients. Axons of differentiated neurons range from the µm scale up to the metre scale and rely on an active transport mechanism as diffusion would be to slow to deliver molecules from the cell body to the distal axon regions within a reasonable time scale. In the context of intracellular transport, MTs can be seen as tracks for motor proteins of the kinesin and dynein family, which walk along these tracks and transport their cargos.

The range of cargos that is transported along MTs is quite diverse and includes whole organelles such as mitochondria (Hirokawa, 1996), RNAs (Holt and Bullock, 2009, Hermesh and Jansen, 2013) and a variety of vesicles such as endosomes or lysosomes (Hamm-Alvarez and Sheetz, 1998). Many defects in intracellular transport are directly linked to severe diseases. For example, two proteins implicated in Parkinson's disease, PINK1 and Parkin control the association of mitochondria with kinesin motors and consequently their mobility. Misregulation of mitochondria transport and associated oxidative stress are hallmarks of Parkinson's disease (Wang et al., 2011). The MT

cytoskeleton is also used by viruses to travel their way towards the nucleus where DNA insertion into the host genome takes place (Sodeik et al., 1997).

In addition to the classical cargos, many motor proteins themselves are transported along MTs by other motors with opposed directionality. Studies in *Xenopus* egg extracts revealed that dynein transports kinesin 5 proteins towards spindle poles (Uteng et al., 2008). In order to facilitate minus end directed transport of cargo from the plus end of a MT, dynein motors need to be targeted to these ends. This is ensured by a combination of kinesin mediated transport of dynein (Ligon et al., 2004, Yamada et al., 2010) and a directed loading onto MT ends by +TIPs (Galjart, 2005, Moughamian et al., 2013).Dynein targeting to MT plus ends is not restricted to vertebrate systems and has also been observed in fungi (Zhang et al., 2003, Galjart, 2005). In cells were dynein is not enriched at MT plus ends (e.g. plants that do not have dynein) minus end directed kinesins are usually enriched at plus end, as it has been shown for ATK5 in *Arabidopsis thaliana* or NCD in *Drosophila melanogaster* (Ambrose et al., 2005, Goshima et al., 2005).

Interestingly, cargo transport along MT tracks is bidirectional and motors of opposing directionality are present within the same cargo complex. This mechanism is thought to allow a more dynamic regulation of cargo distribution, more precise establishment of gradients and also proved a mechanism to correct for errors (Welte, 2004). However, the exact mechanism of specific cargo recognition and distribution during this highly complex sorting process is not well understood yet. A comparison of riobonucleoprotein (RNP) cargo complexes in *Drosophila melanogaster* showed that apically localized RNAs containing RNP complexes contain higher numbers of minus end directed motors as compared to “non-localized” RNA/RNP complexes which provides a possible mechanism for their net biased movement towards MT minus ends (Amrute-Nayak and Bullock, 2012).

1.7.2.2 Motors and localized nucleation form the spindle for cell division

MTs form the mitotic and meiotic spindle responsible for segregating the genetic material prior to cytokinesis. The spindle is a bipolar array of MTs that center the condensed DNA at the metaphase plate and later on mediate segregation of sister chromatids to opposing sites of the cells. A RanGTP mediated gradient controls

localized nucleation of MTs around the DNA that are then arranged into the typical spindle arrays by motor proteins, cross likers, severing enzymes and other factors that control MT stability and mediate their attachment to DNA. In many cell types, spindle positioning is further supported by membrane associated dynein that exerts pulling forces. In addition to RanGTP, centrosome containing cells employ an additional pathway to link MTs emanating from centrosomes to kinetochores, generally called the "search and capture" mechanism, which coexists with the RanGTP pathway (Loughlin et al., 2011, Wittmann et al., 2001).

Another important function of motor proteins is the removal of check point components, allowing cells to progress through the distinct cell cycle stages. Among other phenotypes, p150 inhibition in HeLa cells causes mitotic delays because check point components that inhibit the metaphase anaphase transitions are not removed by the dynein-dynactin complex (Ozaki et al., 2011).

1.7.2.3 Motors and +TIPs influence cell morphology

MT control main aspects of cell morphology, giving rise to the many different overall shapes of cells but also organizes intracellular organization and architecture. MT acts as tracks for proteins from the kinesin and dynein family that slide the ER membrane along the MT network (Wozniak et al., 2009). The integral membrane protein STIM1 has been shown to bind directly to the +TIP EB1, forming the TAC (tip attachment complex) complex. As a consequence, the ER membrane is dragged along the path of a MT end and the ER rearranges in response of MT dynamics (Duellberg et al., 2013).

MTs contribute to the overall shape of a cell by two mechanisms. Direct forces exerted by MT dynamic instability impact the overall shape of a cell but also the motor protein mediated delivery of cellular components to a specific side of the cell determines indirectly the shape of a cell (Rodionov et al., 1993, Gittes et al., 1993). An intensely studied example for this process is axonal outgrowth in neurons were membrane material is delivered to the axonal growth cone along MTs and were an orchestrated MT and actomyosin network facilitates correct mechanical properties for axonal outgrowth (Goldberg, 2003, Schaefer et al., 2008).

1.7.3 MT regulation by other MAPs

Despite +TIPs many other proteins are known that directly regulate the MT cytoskeleton in cells. These include severing proteins (e.g. katanin), cross linkers, nucleation factors and general MT stabilizing proteins such as tau. For a detailed description see the review by Amos & Schlieper and references within (Amos and Schlieper, 2005).

Chapter 2. Mechanism of Microtubule Catastrophe Induction Probed by Fast Microfluidic Buffer Exchange

2.1 Introduction

MT dynamic instability has been described more than 25 years ago and has been subject to extensive experimental and theoretical studies, but its underlying mechanisms are still not fully understood. *In vitro* studies with purified tubulin yielded important information about this process because these experiments are performed under defined conditions and are open to manipulations to access the influence of different parameters individually.

Several possible scenarios of MT dynamic instability have been proposed so far (as summarized in **Fig.5**). Unfortunately, experiments that clearly distinguish between these models are elusive. A very insightful type of experiments are tubulin dilution experiments where depolymerisation of dynamic MTs is induced by partial or complete removal of free tubulin. Different models predict different behaviours of MTs after tubulin removal and many theoretical studies have simulated the behaviour of individual dynamic MTs after rapid and complete tubulin removal (Piette et al., 2009, Brun et al., 2009, Martin et al., 1993, Bowne-Anderson et al., 2013, Flyvbjerg et al., 1996, Padinhateeri et al., 2012, Bolterauer et al., 1999, Margolin et al., 2012). But until now, no such experiment has been performed.

The majority of dilution experiments have been performed in bulk and did not allow observation of individual MTs (Voter et al., 1991, Caplow and Shanks, 1996, Drechsel and Kirschner, 1994). So far, the only exception is a pioneering study performed by *Walker et al.* in which individual MT have been observed by DIC microscopy while free tubulin was diluted to a calculated concentration of 3.3 μM during a time course of 8 seconds. After tubulin dilution, MT started to have catastrophes with an average delay of ~ 10 seconds; the time until the feature that stabilizes MT ends against catastrophe has decayed to a level, where it does not protect MTs against catastrophe anymore. The

delay time between tubulin dilution and the onset of catastrophe was largely independent of the initial tubulin growth speed before dilution (Walker et al., 1991).
Several ideas have been formulated since then, trying to explain the underlying mechanism of dynamic instability of MT plus ends. With an increasing amount of available experimental data, models for catastrophe induction have to face the challenge to explain various aspects of dynamic instability: They have to predict that (a) higher tubulin concentrations lead to higher growth speeds, (b) the catastrophe frequency decreases with higher growth speed but that at the same time (c) the delay time until catastrophe after tubulin removal is independent of the initial growth speed at the time point of dilution; and (d), it further has to predict the reported aging phenomenon (see introduction, **Fig.4** and **Fig.5**). At least qualitatively, some of the reported models predict the points (a-d) (see Introduction 1.3.4, and a very well written introduction in (Bowne-Anderson et al., 2013)). However, the mechanisms for dynamic instability proposed by these models are very different i.e these different models cannot be all correct at the same time.
20 years after *Walker at al* published their study, I used modern microfluidics devices in combination with simultaneous multi-colour TIRF microscopy imaging to perform tubulin wash out experiments with greatly enhanced time resolution. I designed these experiments in a way to directly test predictions from current models of dynamic instability. I confirmed the principle finding by *Walker et al* that delay times and initial growth speed after dilution do not correlate well and gained several new insights into the process of catastrophe induction. These new insights allowed discriminating between previously proposed models for dynamic instability.
GTPase cycle associated transition kinetics at MT ends were found to be the main trigger responsible for MT catastrophe induction. Aging contributed significantly - but little in comparison to transition kinetics rates at MT ends – to catastrophe induction. I found no evidence of destabilizing defects that have been proposed recently as a cause for dynamic instability (Bowne-Anderson et al., 2013, Gardner et al., 2011b) I discovered a relationship between density fluctuations of Mal3 binding sites at MT ends and MT stability. These density fluctuations in combination with evolving tip tapering provide a possible explanation of MT dynamics and also provide possible explanations for the observed differences between MT plus ends and minus ends.

2.2 Results

2.2.1 Assay design and validation

MT dynamics have been studied extensively using TIRF microscopy based assays (Telley et al., 2011, Mohan et al., 2013, Komarova et al., 2009, Bieling et al., 2007, Tropini et al., 2012, Gardner et al., 2011b, Bieling et al., 2008a, Pecqueur et al., 2012). In this assay type, biotinylated GMPCPP stabilized fluorescently labelled MT seeds are attached to PEG-Biotin functionalized glass cover slips by Neutravidin in flow chambers assembled by sandwiching two glass cover slips with double sticky tape (Telley et al., 2011) Methods section 5.6). From these GMPCPP seeds, free tubulin (in part fluorescently labelled) assembles into MTs exhibiting dynamic instability behaviour (Scheme in **Fig.13a**). In essence, this assay has been transferred to a microfluidics device allowing fast solution exchanges during imaging (**Fig.7**). To perform this assay, PDMS based micro channels were transiently attached to PEG-biotin functionalized glass using standard surface plasma treatment procedures ((Lycans et al., 2013) and methods section 5.7 for details). Solutions were introduced via three independently controllable inlet channels via computer controllable syringe pumps. Neutravidin and biotinylated GMPCCP seeds in assay buffer (methods section 5.6 and 5.7) were introduced via one inlet and the GMPCPP seed density could be directly monitored by TIRF microscopy. Unbound GMPCPP seeds were removed by assay buffer and experiments were started by introducing solutions of choice in the desired order. MTs were aligned by flow (**Fig.7c**) to avoid bending induced MT damage and to simplify downstream analysis. A flow rate of 15 µl/min was maintained throughout the entire experiment to maintain MT alignments.

I first confirmed that solution exchange during MT growth did not cause catastrophes by itself. For that, I switched between two solutions with different tubulin concentrations and the background fluorescence of tubulin could be used as a convenient indicator to monitor solution exchanges. **Fig.7d** shows that a solution exchange by itself did not cause catastrophes and that MT adapted quickly to changed environments. As can be seen from the slopes in the kymographs, growth velocity changed essentially instantaneously when tubulin concentrations are varied (**Fig.7d**). To further verify that solution exchange did not cause catastrophe, I performed repeated

buffer exchanges between two tubulin containing solutions, one being supplemented with Mal3-GFP as a monitor of solution exchange. Mal3 is the fission yeast homolog of EB1 (as explained in the introduction, section 1.6.1) and accumulates specifically at growing MT ends. As shown in **Fig7e**, MT growth was not affected during a total of 8 consecutive solution exchanges and these buffer exchanges did not cause catastrophes.

The flow profile within microchannels under laminar flow conditions is parabolic i.e. fluids have higher velocities in the channel middle as compared to the regions close to the channel walls (**Fig. 8a**) (Reynolds, 1895, Allen et al., 2010)). The depths of the TIRF field is ~150 nm and MTs are expected to be within 50 nm proximity of the glass coverslip (Kerssemakers et al., 2006). During solution exchange a slight delay between the time point where new molecules can be seen in the TIRF field as background fluorescence and before they are in actual contact with the microtubule is expected. To measure this delay, I exchanged a tubulin containing solution with a tubulin containing solution supplemented with Mal3-GFP (**as in Fig.7e**) with high time resolution (32 frames per second).**Fig.7f** shows intensity profiles for the GFP background fluorescence and the GFP signal at MT ends after background subtraction. An increase in fluorescence specifically at the MT ends in comparison the background fluorescence was observed with a delay of 150 ms – 200 ms. This delay was negligible in comparison to the time scale of further experiments (several seconds, see below). The total duration of a complete solution exchanges close to the surface (were MTs are located) was ~ 500 ms as judged by the time course of the fluorescent intensities (**Fig.7f and Fig.8b**). Imaging was performed only in the centre of the channel (see material methods) to avoid unwanted effects near lateral channel edges.

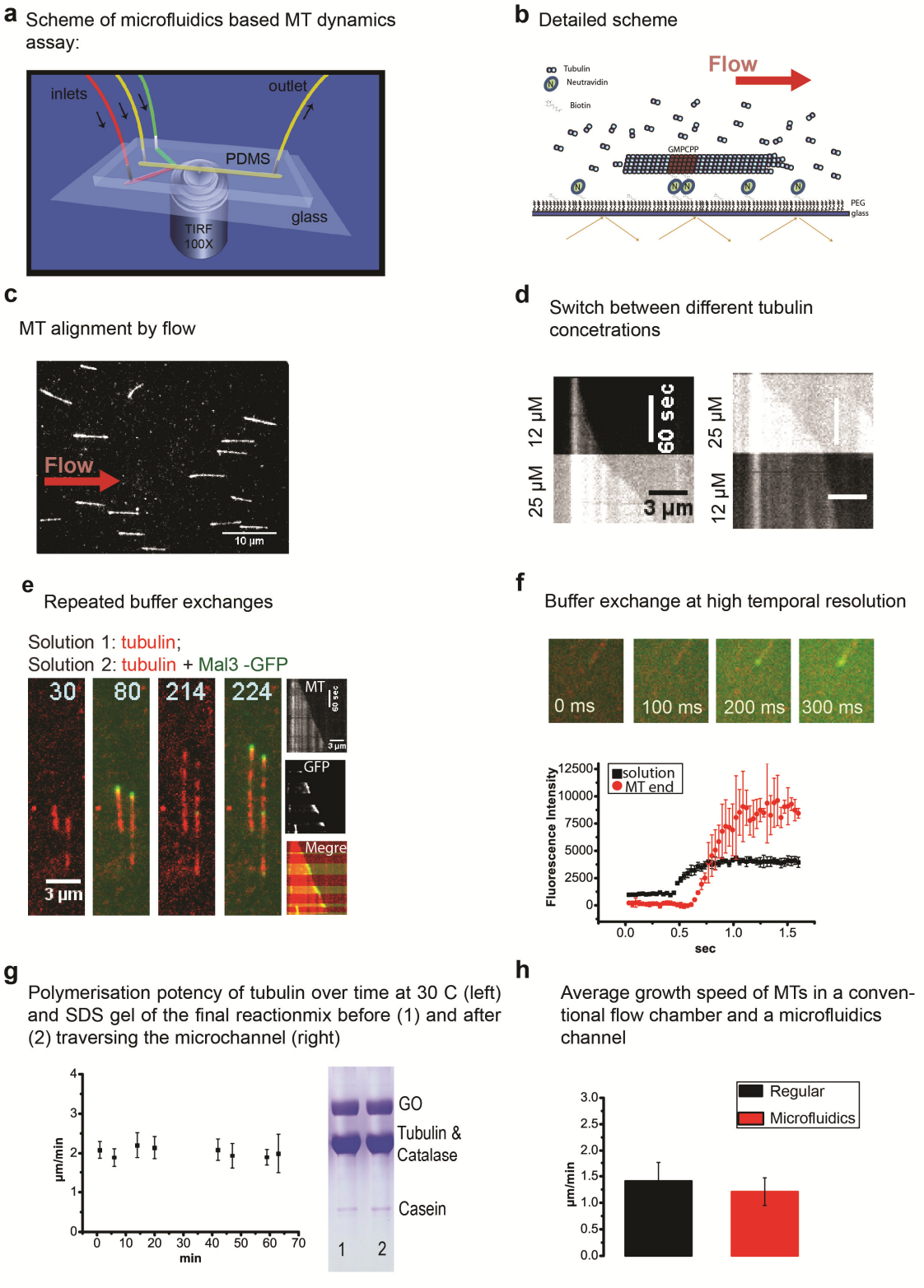

Figure 7: Assay validation

(a) Scheme of microfluidics based set up. Three individually controllable inlet channels merge into a main channel where MT dynamics is observed using TIRF microscopy. PDMS and Peg-Biotin glass are transiently attached to each other by surface plasma treatment. (**b**) Detailed scheme of the field of view where imaging takes place. MTs grow from Biotin/Neutravidin

immobilized GMPCPP seeds on PEG-biotin functionalized glass coverslips, exhibiting dynamic instability behaviour which is observed by TIRF microscopy. (**c**) MTs align parallel to the direction of flow. The flow is maintained throughout all experiments to maintain MT alignment. Occasionally, MT are not well aligned with the flow (see an example at an upper middle position), which tend to bend due to flow and was not analysed. (**d**) Representative kymograph of tubulin concentration alteration within a growth phase of a MT as indicated. The change in background fluorescence marks the time point of solution exchange. (**e**) Repeated solution exchanges do not alter MT dynamics. MT growth was observed during several sequential solution exchanges. Both solutions contained 15 µM tubulin (in part fluorescently labelled) and one solution was supplemented with 75 nM Mal3-GFP, which accumulates at growing MT ends. A time series (left) and representative kymographs (right, individual channels as indicated and their merge, tubulin in red, Mal3-GFP in green) are presented. (**f**) Solutions were exchanged as in (**e**) and imaging was performed at 32 fps. A time series (upper) demonstrates a short delay between increased background fluorescence and specific enrichment of Mal3-GFP at the MT end region. The GFP background florescence (black) and the fluorescent at the MT ends (red, max intensity minus background) are plotted against the time (lower). (**g**) Tubulin stocks were diluted to 18 µM (with 8% Alexa 568 tubulin) in final assay buffer and stored at 30˚ C for the indicated time points, introduced in conventional flow cells and plus end growth speeds were measured as described (Bieling et al., 2010a) (left). Identical volumes of final assay buffer (including 18 µM tubulin) were analysed by SDS-PAGE followed by comassie brilliant blue staining before and after traversing the microchannel. GO: glucose oxidase. (**h**) MT plus end growth speeds at 14 µM were compared between conventional flow chambers and a microfluidics device under constant flow (15 µl/min).

For the majority of experiments, background fluorescence of free tubulin was used as an indicator for solution exchange. For experiments were all solutions had the same tubulin concentration purified GFP, GFP labelled Mal3 or Alexa647-BSA was used as reporters of buffer exchange. Purified GFP, Mal3-GFP, Alexa568 tubulin and Alexa647-BSA had virtually identical solution exchange profiles (not shown).

During the preparation of the microfluidics device (e.g. attaching Neutravidin, coupling of the GMPCPP seeds) prior to the actual experiment, tubulin solutions remained in the tubing connected to the micro channels and could not be kept on ice. The total assembly time until an experiment was started was typically 15 – 20 minutes. To test that tubulin does not lose a significant amount of polymerization competent subunits during this period, I stored tubulin in the final imaging buffer at 30˚ C for different time points and then introduced these solutions into conventional flow chambers and measured the growth speed of MT plus ends. Growth speeds stayed constant (within the error) over the time period of an hour, verifying that storage of tubulin at 30 ˚C for the indicated time period is not a problem (**Fig.7g**). In line with that, other research groups observed MT dynamics using TIRF microscopy for over 35 minutes without detectable loss of polymerisation efficiency (Mohan et al., 2013).

As a further control, final reaction mixes were loaded onto a SDS gels before and after passing through the tubing and the PDMS micro-channel. Band intensities of all proteins in both lanes were very similar (**Fig.7g, right**) indicating that nonspecific adsorption to the tubing or the micro-channel wall does not significantly falsify the calculated final protein concentrations. I compared the growth speeds of MT plus ends in conventional flow chambers (Telley et al., 2011) and within microfluidics devices, which were in a similar range (**Fig.7h**), which further indicates that no significant amount of free tubulin is depleted due to nonspecific adsorption to the microfluidics device.

In summary, the well-established TIRF based MT dynamics assay (Bieling et al., 2007, Telley et al., 2011) has been successfully transferred to a microfluidics device where typical parameters of dynamic instability could be observed. Complete exchange between two solutions was fast (~500 ms) and did not cause MT destabilization by itself.

2.2.2 Tubulin removal induced catastrophes

In the current work tubulin was essentially completely removed in much less than a second to study the delay time until catastrophe at MT plus ends after tubulin removal with greatly enhanced time resolution and precision. MTs were grown in the presence of free tubulin containing solutions that were then exchanged with tubulin free solutions (Scheme in **Fig.8a**). **Fig.8b** shows a kymograph of tubulin background fluorescence during such a wash out experiment. The fluorescence intensity is plotted against the time (**Fig.8b, right**) yielding total solution exchange times of ~ 500 ms, similarly to the time course of Mal3-GFP *wash-in* as depicted in **Fig.7**. The representative kymograph in **Fig.8c** depicts the distinct phases of a tubulin wash out experiment. MTs grow until tubulin is removed as indicated. The MT end remains in a pause like state without obvious net shrinkage, termed “delay time” until transition into a rapid shrinking phase occurs (=catastrophe). In order to have an objective criteria for the catastrophe onset, I defined catastrophe onset as the time point when the MT plus end shrank 3 pixels (=360 nm) i.e. its new end position was 3 pixels shifted relative to its position at the time point of tubulin wash out. **Fig.8d** depicts typical distributions of delay times among one condition. The histogram shows clearly, that the data cannot be described by a mono

exponential decay which suggests that catastrophe induction after tubulin wash out is not a stochastic single step process.

2.2.3 Initial MT growth speed and delay times until catastrophe after tubulin wash out do not correlate

I polymerized MT at different tubulin concentrations in the range from 9.8 μM to 24.5 μM for 160 sec (± 10 sec), removed free tubulin and measured the delay time until catastrophe. The difference in growth speed between the highest and lowest tubulin concentration was ~ three fold, as judged from the mean length of MTs at the time point of wash out (**Fig.8e**). No strong correlation between initial growth speed and delay time until catastrophe was observed (**Fig.8e1**). MTs at the lowest tubulin concentration of 9.6 μM started depolymerizing after 5.72 sec (± 0.43 sec, standard error (SE)) while MT at 24.5 μM had an average delay time until catastrophe of 6.32 sec (± 0.49 sec, SE). The apparent trend (R^2=0.85) was statistically not significant (ANOVA F-Test test, (Ip, 2007)). These findings are in good agreement with earlier dilution experiment (Walker et al., 1991, Voter et al., 1991) and show that when tubulin is rapidly and completely removed, initial growth speed and the delay time until catastrophe are largely independent of each other.

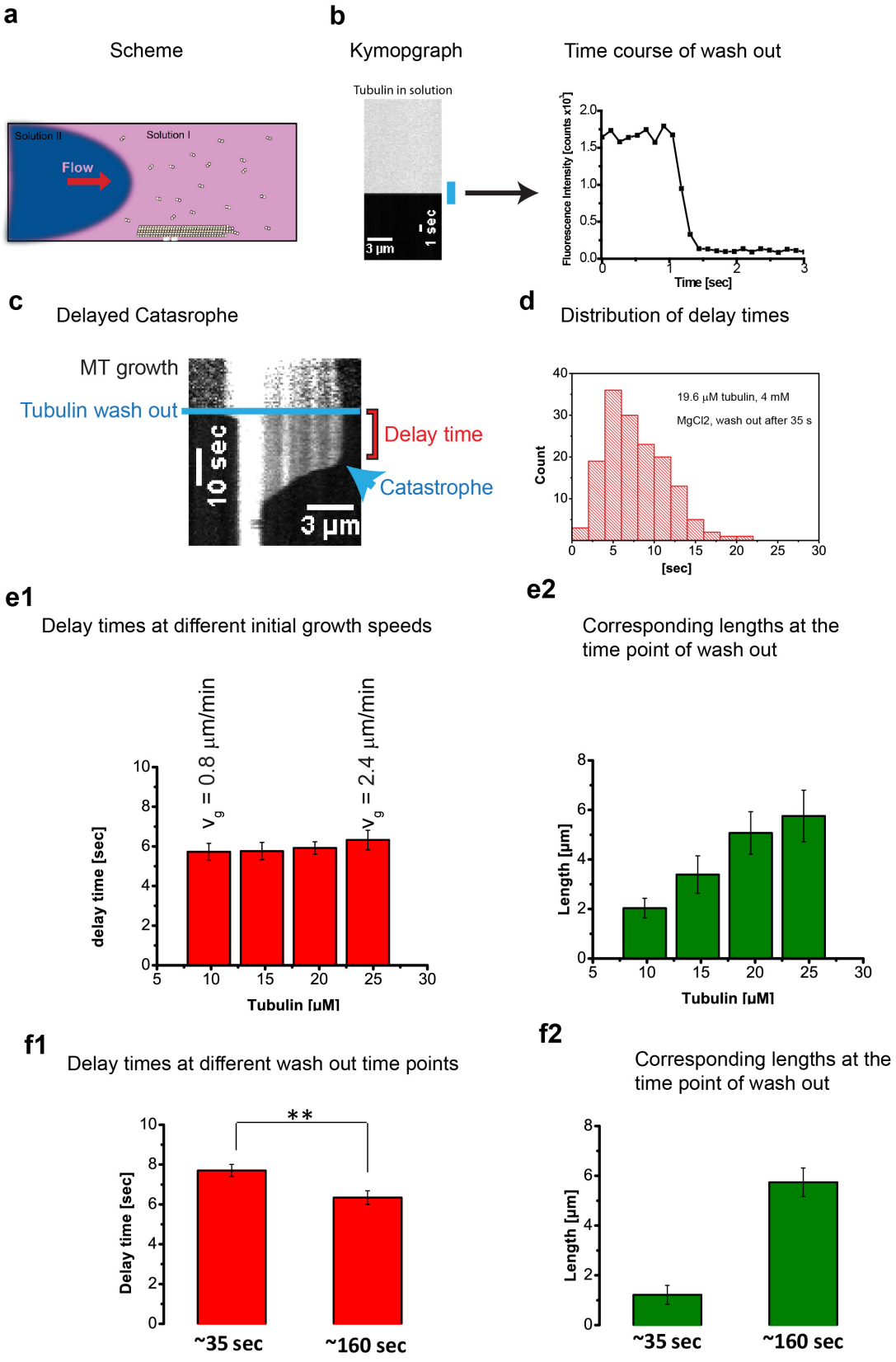

Figure 8: Dependency of delay times until catastrophe after tubulin wash out on initial growth speed and wash out time point

(**a)** Schematic representation of a tubulin wash out experiment. MTs grow in the presence of free tubulin until tubulin free solutions displace the tubulin containing solution(**b**) Representative kymograph of the background fluorescence of 20 µM tubulin (8% Alexa 568 labelled, 1.6 µM in total) during a tubulin wash out experiment (left). The time course of wash out was monitors via line scans from these kymographs in which fluorescence intensities are plotted against time (right) (**c**) Distinct phases of a wash out experiment. The MT growths on both ends in the presence of 14.7 µM, (including 8% Alexa568 tubulin; marked as "growth") and soluble tubulin dimers are removed (indicated as "Tubulin wash out"). The "delay time" is measured from the kymograph until the MT switches to a rapid shrinking phase ("catastrophe"). The exact time point of catastrophe was defined as the time point, when the MT end is 3 pixels away from its position at wash out.(**d**) Histogram representation of a representative data set of delay times within one condition. Exact conditions are indicated. (**e1**) MTs were grown for 160 sec (± 10) at the indicated tubulin concentrations and soluble tubulin was removed. Plotted are the mean delay times until catastrophe (± standard error (SE)) against the tubulin concentration during the growth phase. (**e2**), average lengths (± Stdev) at the time point of tubulin wash out plotted against the tubulin concentration during growth. From these lengths (divided by the time period of growth), the average growth speed (v_g) was estimated as indicated in (e1). At least 50 individual plus ends were analysed from at least 3 independent experiments per condition. (**f1**) Microtubules were grown at 19.6 µM for 35 seconds (± 5 seconds), or 160 seconds (±10 seconds) and soluble tubulin was removed. Plotted are the mean delay times until catastrophe (± standard error). At least 100 individual plus ends were analysed from at least 4 independent experiments per condition. Statistical test for (f1) was: Mann-Whytney U test (Mann, 1947) with significance level $p < 0.01$. (**f2**) depicts the mean lengths (± StDev) at the time point of wash out corresponding to (f1).

2.2.4 Tubulin wash out at later time points results in decreased waiting times until catastrophe

Under "steady state conditions " (≈ constant tubulin concentration; "no wash out"; from now on called steady state), short/young MT are less likely to switch from a growing to a shrinking state as compared to old/long MTs, a phenomenon that has been called MT aging (Gardner et al., 2011b, Gardner et al., 2013, Bowne-Anderson et al., 2013, Mohan et al., 2013). I performed tubulin wash out experiments at a fixed tubulin concentration of 19.6 µM but varied the time point of wash out to test, if the tubulin wash out time points influence the delay time until catastrophe after tubulin wash out and if aging can be seen in tubulin wash out experiments.

MTs were polymerized for 35 sec (±5 sec) or for 160 sec (±10 sec) and then tubulin was removed. These conditions are called "early" for the wash out at 35 sec and "late" for the wash out after 160 seconds of elongation, respectively. Consequently, MTs from the "early" condition were younger and also shorter (**Fig.f2**). I compared the delay times for the two conditions and found statistically significant longer waiting times until

catastrophe for shorter / younger MTs (U test, P <0.01 (Mann, 1947)). This indicates that something destabilizes MT ends over time under steady state and non-steady state conditions which is related to length or age.

In summary, the delay times until catastrophe after tubulin wash out depend on the time point of wash out but not on the initial growth speed (**Fig.8**). Qualitatively, this result was predicted from the defect accumulation model (Bowne-Anderson et al., 2013) and the tapering model (Coombes et al., 2013) but cannot be explained purely by longitudinal coupling (Brun et al., 2009) or lateral cracks (Flyvbjerg et al., 1996) (see below; section 2.2.6 and discussion).

2.2.5 Mg^{2+} accelerates transition rates associated to the GTPase cycle and shortens the delay time until catastrophe after tubulin wash out

Crucial parameters for MT dynamics are the on-rate of arriving tubulin dimers, their off-rates and the GTP-hydrolysis rate. In order to test MT dynamic instability models more rigorously, I tested the impact of the hydrolysis rate on MT stability after tubulin wash out without affecting the other rates.

Mg^{2+} seemed to be a good tool to access the impact on the hydrolysis rate. Studies in actin showed that Mg^{2+} directly enhances ATPase hydrolysis rates, effectively shorting the ATP cap (Carlier et al., 1987). Increasing Mg^{2+} concentrations increase MT plus end growth speeds without stabilizing these ends, possibly due to enhanced conformational transition kinetics at MT ends (O'Brien et al., 1990). *O Brien et al* further showed that the off-rate of tubulin subunits at growing MT plus ends is not affected by increasing Mg^{2+} concentrations. Because the on-rate of tubulin dimers that add onto the plus end is zero after tubulin removal in wash out experiments, Mg^{2+} might be a suitable tool to investigate the effect of hydrolysis rate associated transition kinetics on MT stability after tubulin wash out directly.

To obtain evidence if Mg^{2+} influences the GTP hydrolysis rate, I tested its effect on the life-time of the Mal3 binding site at MT ends. Mal3 binds a nucleotide dependent conformation at MT ends and thus is a good sensor to monitor changes associated with GTP cycle kinetics at microtubule ends. Tubulin conformations at MT ends are formed, where Mal3 binds to with high affinity and selectivity. These tubulin conformations transform into the GDP lattice over time, where Mal3 does not strongly bind to. The

kinetics of this transformation can be measured and expressed as life time of the Mal3 binding site, which is the ratio of the Mal3 comet decay length divided by the MT growth speed (see **Fig.31** for a scheme and a more detailed explanation in the method section 5.11 (Bieling et al., 2007, Maurer et al., 2011, Maurer, in press)).

I measured the life time of the Mal3 binding site at 10 mM and 1.6 mM $MgCl_2$ in the presence of 2.5 nM Mal3-GFP in conventional flow chambers. The average comet shapes of Mal-GFP signals and the MT growth speeds were determined for both Mg^{2+} conditions as described (methods section 5.11), from which the life time of the Mal3 binding site could be calculated. Strikingly, the life time of the Mal3 binding sites was reduced by ~ 40 % in the high Mg^{2+} condition. While the life time of the Mal3 binding site was found to be 10.52 sec (± 0.44 sec, S.E.) at 1.6 mM $MgCl_2$, it was reduced to 6.63 sec (± 0.53 sec) at 10 mM $MgCl_2$ (**Fig.9a**). Similar to previous reports, MT growth speed was also enhanced at higher Mg^{2+} concentration under my conditions (**Fig.9a**). This suggests that Mg^{2+} indeed accelerates transition kinetics at MT ends, which are likely to be directly linked to GTP hydrolysis. As an additional effect, a reduction in the overall Mal3-GFP affinity at higher Mg^{2+}concentration was observed, potentially due to some charges that are shielded by Mg^{2+} that are involved in the MT – Mal3 interaction.

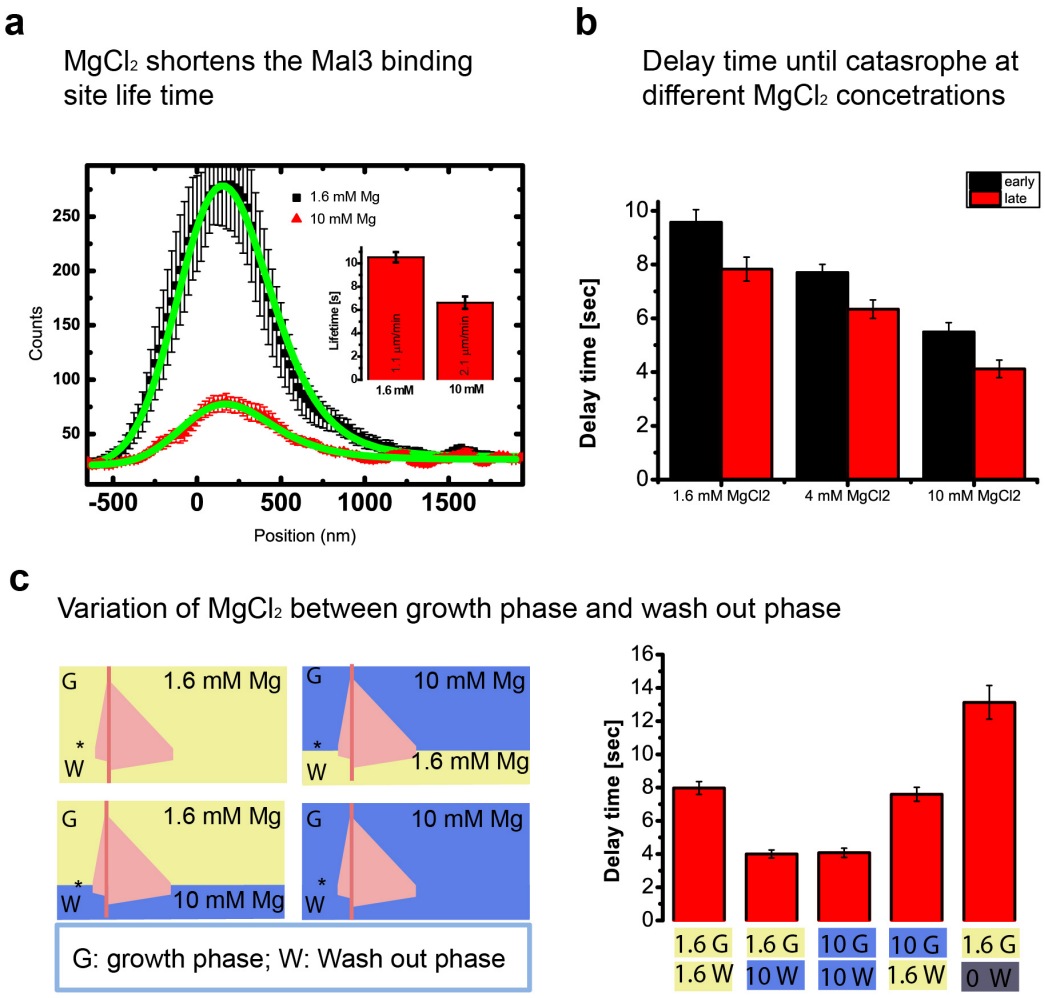

Figure 9: Mg^{2+} triggered transition kinetics at MT ends determine MT stability

(**a**) MTs were grown in conventional flow chambers in the presence of 2.5 nM Mal3-GFP and 1.6 mM $MgCl_2$ or 10 mM $MgCl_2$. The tubulin concentration was 15 µM (including 8% Alexa568 tubulin). Mal3-GFP comets were averaged using automated image analysis tools and comets were fitted as specified in material and methods (5.11). The averaged comets with respect to the MT end (position 0) are plotted. Average growth speeds are inserted in the bar graph for each condition. Mal3 binding site life time are presented in the bar graph on the right (mean ± S.E.).(**b**) MT were grown for 35 (± 5 seconds; "early") seconds or 160 (± 10 seconds; "late") at 19.6 µM tubulin at different $MgCl_2$ concentrations as indicated and soluble tubulin was removed. The delay times until catastrophe are plotted. Errors are standard errors. For each condition, at least 50 individual MTs were analysed from 3 independent experiments. (**c**) MTs were grown at 19.6 µM tubulin for 160 (± 10 seconds) seconds and tubulin was removed (marked with "*" in the scheme). Buffers during MT growth (marked as "G") and buffers used for tubulin wash outs (marked as "W") contained the indicated $MgCl_2$ concentration. For each condition, at least individual 50 MTs were analysed from 2 independent experiments.

I next tested if increasing Mg^{2+} concentration would affect the delay times until catastrophe after tubulin removal. This was indeed the case (**Fig.9b**). MT grown in the presence of low Mg^{2+} (1.6 mM) for ~ 160 sec had delay times of 7.83 sec (± 0.45 sec,

S.E.). At high Mg^{2+} concentrations (10 mM), the delay times until catastrophe decreased to 4.12 sec (± 0.32 sec, S.E.). Interestingly, the difference between "early" and "late" wash out time points was not significantly affected (**Fig.9b**), suggesting that increasing Mg^{2+} concentrations do not have a strong impact on "aging" in this assay type. Taken together, this suggests that accelerated transition kinetics decreases the delay time until catastrophe after tubulin washout by accelerating the decay of the stabilizing end structure that is linked to GTP hydrolysis.

2.2.6 GTPase cycle associated transition kinetics determine the waiting times until catastrophe but not the growth history of an MT

The main models to explain "MT aging" are coupling models (e.g. (Brun et al., 2009)), the tapering model (Coombes et al., 2013) and the "defect accumulation model" (Bowne-Anderson et al., 2013) (Introduction, section 1.3.4 and **Fig.5**). A pure coupling model cannot explain shorter waiting times for late time point of tubulin wash outs because the distribution of D to T state ratios does not increase over time in this type of model. In contrast, both, the tapering and the defect model would predict a trend towards decreased delay times until catastrophe after tubulin removal at later wash out time points. In the defect model, the number of acquired defects prior to tubulin wash out determines the waiting time until catastrophe. The hydrolysis rate influences the occurrence rate of these steps/defects during the growth phase (before wash out) but is negligible after wash out during the delay period until catastrophe. (Introduction, 1.3.4). In the tapering model, the hydrolysis rate is important for MT life times under steady state as well as in the tubulin wash out case (Introduction1.3.4).

To unambiguously distinguish between the two models, I created MT with the same average number of hypothetical defects at the time point of tubulin wash out but different transition kinetics rates at MT ends after tubulin wash out.

To do that, I polymerized MTs at low $MgCl_2$ concentrations (1.6 mM) for 160 sec (±10 sec) and used a buffer with high $MgCl_2$ (10 mM) or low $MgCl_2$ (1.6 mM) for the tubulin wash out. I obtained average delay times of 4.00 sec (± 0.24 sec) for the wash out with high Mg^{2+} buffer, virtually identical to MTs where growth phase and wash out phase were performed under high Mg^{2+}conditions, were catastrophes were observed after 4.01 sec (± 0.28 sec SE)(**Fig.9c**). This is ~ 2 times shorter as compared to MTs where

growth phase and wash out phase were performed at low (1.6 mM) Mg^{2+}concetrations, were catastrophes started with an average delay of 7.97 sec (± 0.39 sec SE) after tubulin removal (**Fig9c**). Therefore, the growth history (in which defect accumulation would have had happened (Bowne-Anderson et al., 2013)) does not have an effect of the delay times until catastrophe. In turn, the composition of the buffer used for tubulin wash out (which is expected to determine transition kinetics rates at MT ends) determines this delay time.

Vice versa, when wash outs were performed in the presence of 1.6 mM $Mg^{2+}$of MTs grown in the presence of 10 mM Mg^{2+}, average delay times were 7.59 sec (± 0.42 S.E.); very similar to MT were both phases were performed at 1.6 mM Mg^{2+} , were average delay times were 7.97 sec (± 0.39 sec SE) (**Fig.9c**). These experiments show that the delay times until catastrophe after tubulin wash out does not depend on the growth history (e.g. defects) but is determined by transition kinetics rates at MT ends.

To further test the impact of Mg^{2+} dependent transition kinetics, I performed tubulin wash out experiments with Mg^{2+} free wash out buffer. In good agreement with the experiments described in this section, average delay times until catastrophe further increased to 13.13 sec (± 1.02 sec, S.E.), which is a more than a 3 fold increase in comparison to the 10 mM Mg^{2+} condition (**Fig.9c**).

2.2.7 Mal3 shortens the delay time until catastrophe after tubulin wash out

Similarly to Mg^{2+}, Mal3 has been shown to shorten the life time of its own binding site and accelerates MT growth speed. In addition, Mal3 increases MT catastrophe frequency ((Maurer et al., 2011, Bieling et al., 2007)). Due to these features, Mal3 has been hypothesized to act as a maturation factor for MT ends, in analogy to a GTPase activating enzyme (Maurer et al., 2011, Maurer et al., 2012, Maurer, in press)

If Mal3 acts as a maturation factor by accelerating transition kinetics at MT ends and if these transition kinetics determine MT stability after tubulin removal, Mal3 should decrease the delay times until catastrophe after tubulin wash out. Indeed, addition of 75 nM Mal3-GFP reduced the delay time until catastrophe from 7.43 sec (± 0.39 sec SE) to 4.63 sec (± 0.20 sec SE) at a constant Mg^{2+}concentration of 1.6 mM (**Fig.10a**).

This in indicative of a link between the Mal3 binding site life time and MT stability, present under “steady state” conditions and in the rapid dilution case.

2.2.8 Fluctuation in the Mal3 binding site density determine the momentary stability of MT plus ends

During growth periods, MT growth velocities considerably fluctuate (Pedigo and Williams, 2002). Fluctuations in the Mal3 binding site (length or density) during MT growth have not been systematically analysed yet but it has been reported, that the average Mal3-GFP signal at MT ends decreased shortly before catastrophe occurs (Maurer et al., 2012). A possible explanation for that would be that the presence of Mal3 binding sites vanishes prior to catastrophe.

The total length of the Mal3 binding region and therefore the sum of Mal3 binding sites scale with MT growth speed (Bieling et al., 2007). The data presented in **Fig.8** clearly demonstrated that MT growth speed (proportional to Mal3 binding site length) and delay time until catastrophe do not correlate well. However, it could be that not the length but the density of Mal3 binding sites at MT ends is important. These densities might fluctuate and low densities might increase catastrophe probability, which would be a possible explanation why the average Mal3-GFP signal directly before catastrophe is decreased in comparison to the growth phase. A potential relationship between the density of Mal3 binding sites and MT stability has not been studied yet.

A prerequisite for this hypothesis would be that the Mal3 binding site density does fluctuate during growth episodes of MTs. To test that, I measured fluctuations of signals derived from 75 nM Mal3-GFP at MT ends in the presence of GTP and GTPγS, the latter being an essentially non hydrolysable GTP analogue (Scheffers et al., 2000) and therefore a suitable model for MT ends with essentially constant composition i.e. a non-fluctuating Mal3 binding site density. GTPγS mimics an MT end structure to which Mal3 binds to with similar average affinity as compared to the MT end region of GTP/GDP MTs (Maurer et al., 2011). Using automated MT tracking procedures (method section 5.13), I measured the maximum Mal3-GFP signal (essentially the brightest pixel after background subtraction, see Methods section 5.13) over growth periods of MTs in the presence of GTP or GTPγS at 9.9 fps over 1500 frames (= ~ 150 seconds) and extracted intensity and variance of GFP signals for 10 MT per condition.

The overall means of the maximum Mal3-GFP signals were very similar on both types of MT ends (12,115 counts for GTPγS versus 15,204 for GTP). In contrast, the mean variance of the signal was ~ 10 fold higher in the case of MTs growing in the presence of GTP (**Fig.10 b&c**). Because 75 nM is ~ 2.5 times above the k_d of Mal3-GFP for MT ends (k_d was reported to be ~ 30 nM,(Maurer et al., 2011)) fluctuations due to stochastic binding/unbinding events to a constant number of binding sites are essentially negligible (the theoretical contribution to the variance (Wolter, 2003) accounts for less than 1 % of the measured variance for the GTPγS case, which basically reflects instrumental detection noise). These experiments clearly demonstrate that the density of the Mal3 binding sites fluctuates considerably during a growth episode of a MT.

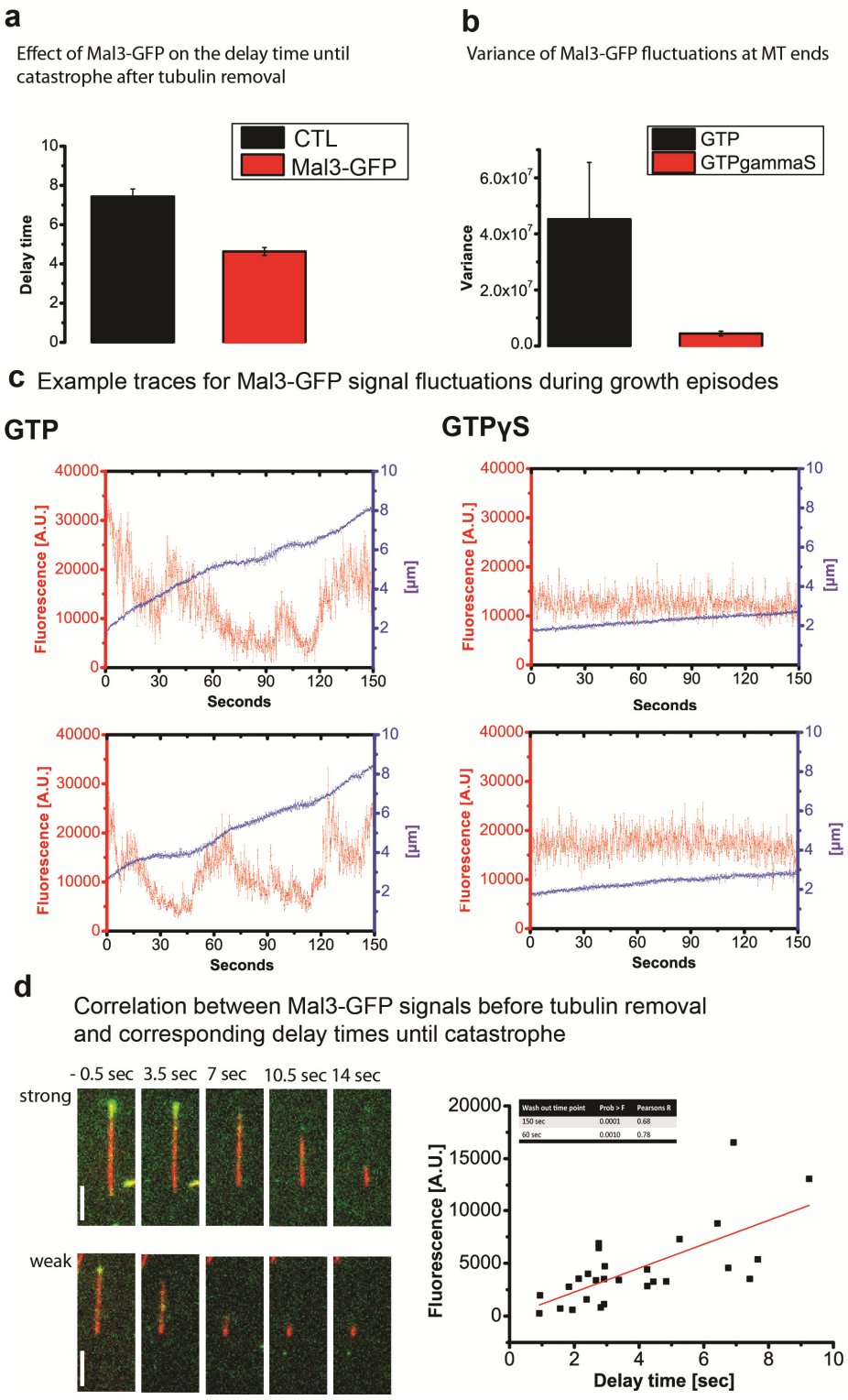

Figure 10: Mal3 binding site density fluctuations correlate with MT stability in dilution experiments

(**a**) MTs were grown at 19.6 µM tubulin for 160 (± 10 seconds) seconds in the presence (red) or absence (black) of 75 nM Mal3-GFP and tubulin was removed and the delay time until catastrophe was measured. For each condition, at least 50 individual MTs were analysed from 3 independent experiments; errors are standard errors. For the control conditions Mal3-storage

buffer was added to maintain identical buffer environments and illumination conditions were identical as well. $MgCl_2$ was 1.6 mM (**b**) MT were grown at 22 µM tubulin (including 8 % Alexa 568 tubulin) in conventional flow chambers in the presence of 75 nM Mal3-GFP and 1 mM GTP or 1 mM GTPγS. MT were imaged at 9.9 fps and analysed by automated tracking. The variance of the max GFP signal is depicted (error: StDev from 10 individual MT growth episodes of 1500 frames (151.5 seconds) from 10 individual MTs from 4 independent experiments per condition) (**c**) Example traces for each condition as in (b). Blue: MT end position (relative to the GMPCPP seed, blue) and the maximum fluorescence intensity (red) of Mal3-GFP at MT plus ends. (**d**) MTs were grown at 19.6 µM tubulin in the presence of 75 nM Mal3-GFP and soluble tubulin was removed after 150 seconds. The maximum GFP intensity 0.5 sec prior tubulin wash out (-0.5 in the image series, left) was measured and plotted against the delay time of the same MT (right). Tubulin: red, Mal3-GFP: green. The significance of the linear regression line was analysed using Anova F test statistics (Origin). The F-value was 21.8 with Prob > F below 0.0001. Similarly good statistical correlations were obtained for tubulin wash outs after 60 seconds as indicated in the inserted table (upper left) in the diagram.

I next asked if the Mal3 binding site density and MT stability are connected and performed tubulin wash out experiments in the presence of Mal3-GFP after 150 seconds of MT growth. Using simultaneous dual colour TIRF microscopy imaging, I directly tested, if the densities of Mal3 binding sites are direct indicators of momentary MT stability. I measured the maximum Mal3-GFP signal shortly (=500 ms) before tubulin removal and plotted these signals against the delay times until catastrophe of the corresponding MTs (**Fig.10d**). Strikingly, there was a good correlation between the Mal3-GFP signal before tubulin removal and the time until the MT started to depolymerize after free tubulin was removed (**Fig.10d**). The pearson's R value for the linear regression was 0.68 and the F value (Anova F test, (Ip, 2007)) was 21.8 with prob > F below 0.0001 (Origin, linear regression analysis,) and thus statistically significant. Considering the fluctuations due to instrumental noise (see Mal3-GFP fluctuations on GTPγS which mainly represents instrumental noise (**Fig.10c, right**)), the obtained correlation is in fact very good. A similarly good linear fit was obtained for a shorter wash out time point of 60 seconds (table inset in **Fig.10d**), demonstrating that the instantaneous Mal3 binding site density is a reliable and age independent measure of momentary stability of an MT ends.

Taken together, this uncovers a link between the density of Mal3 binding sites and MT stability as MT with a high Mal3 density at the end region had significantly longer delay times between complete tubulin removal and catastrophe onset.

2.3 Discussion

2.3.1 Initial MT growth speed and delay times until catastrophe after tubulin wash out do not correlate

In this study, MT catastrophes were induced by fast and essentially complete tubulin removal. MTs were observed on the single filament level using simultaneous multi-colour TIRF microscopy and a microfluidics based set up to measure the decay of the stabilizing end structure after tubulin was removed until MTs had catastrophes. So far, only *Walker et al.* performed a similar type of dilution experiment, where free tubulin was diluted to a calculated concentration of 3.3 μM over a time course of 8 seconds. Using modern microfluidics techniques, MTs could be well alignment with the flow stream and comparatively low flow rates allowed image acquisition during the dilution process which has been proven to be difficult in the set up used by *Walker et al*.

The main finding reported in *Walker et al* is that the initial growth speed before dilution induced catastrophe does not correlate well with the waiting time until catastrophe after tubulin removal. Similarly, I also observed only a very mild and statistically insignificant correlation between the two parameters. *Walker et al.* speculated that the GTPase activity might scale with tubulin growth which would explain these data, assuming that the functional stabilizing cap and the biochemical GTP cap are identical (Walker et al., 1991). However, two observations speak against this idea. If there would be a strict coupling between GTPase rate and MT growth speed, the catastrophe frequency would be independent of the free tubulin concentration (proportional to growth speed). This is not supported by the observation that catastrophe frequency decreases with increasing tubulin concentrations (Walker et al., 1988, Gardner et al., 2011b).

EBs form comets at growing MT ends where they recognize a nucleotide dependent MT conformation (Maurer et al., 2011). *Bieling et al* tested the dependence of comet length and MT growth speed and found that comet lengths increased with higher tubulin growth speeds (Bieling et al., 2007). This also argues against the idea that GTPase activity and MT growth speed are strictly coupled parameters. These observations indicate (although they do not rigorously rule it out) that the GTPase activity and MT growth speed are not strictly coupled. In any case, it means that the length of the Mal3

binding zone and probably the length of the biochemical GTP cap do not correlate with MT stability in rapid dilution experiments. A possible explanation, at first postulated by *Flyvbjerg et al* is the model of "lateral cracks". Here the GTPase activity does not scale with MT growth speed and the biochemical GTP cap is longer for faster growth velocities. In their model, stochastic "lateral cracks" within the GTP cap zone would create new hydrolysis fronts, effectively shortening the functional protective end structure but not the biochemical GTP cap zone. However, this model on its own would not explain why MT exhibit the reported "aging" effect as catastrophes should be randomly distributed.

Weak or no correlations between initial tubulin concentration and delay times until catastrophe after wash out have been also predicted by other models but similarly to *Flyvbjerg et al*, they also do not predict a dependence on the time point of wash out (Brun et al., 2009, Margolin et al., 2012). These models might therefore be incomplete.

2.3.2 MT aging probed by rapid tubulin dilution

While the initial average growth speed of MTs did not correlate with the delay times until catastrophe after tubulin removal, the time point of tubulin removal was critical as short/young MTs had significantly longer waiting times until catastrophe. This is similar to the MT plus end life time distributions measured at steady state, which could not be fitted using a single exponential distribution (Odde et al., 1995). Similarly, the delay time distributions after tubulin wash out could not be described by a single exponential distribution, both consistent with the notion that MT catastrophes are not a stochastic single step process.

In the tapering model, older MTs have increased lengths and also a higher probability of a more pronounced tapering at their ends. In a blunt MT end, all terminal tubulin dimers form three contacts: two lateral contacts and one longitudinal. In a tapered end, terminal tubulin subunits are engaged in one longitudinal and zero, one or two lateral contacts. Thus the average off rate for tubulin dimers is expected to be higher in tapered end structures (Gardner et al., 2011a). As a result, the exposure of non-stabilizing elements at MT ends (e.g. terminal GDP tubulin dimers) commences earlier after tubulin wash out due to accelerated loss of terminal subunits.

In the defect model proposed by *Bowne Anderson et al* , the delay times until catastrophe after tubulin wash out are determined almost only by the constant k (the off rate, which is independent of Mg^{2+}, (O'Brien et al., 1990)) and the number of defects/steps that have been acquired during MT growth prior tubulin wash out. The on rate after tubulin removal is zero. The hydrolysis rate is ~35 times faster than the off rate of terminal GTP-tubulin subunits and therefore does not significantly contribute to the predicted delay in the dilution case. The presented data clearly distinguish between the two models because the contribution of the hydrolysis rate and the number of hypothetical defects could be accessed independently. The data are in good agreement with all predictions derived from the tapering idea. However, a numerical and quantitative expression of this tapering idea is elusive and would be needed to further describe dynamic instability more quantitatively. In contrast, the defect model failed to predict the presented dilution data, which revealed a strong influence of the hydrolysis rate but did not provide evidence for the existence of defects related to MT stability.
Another argument that speaks against a defect model in which irreversible protofilament loss induces catastrophes comes from the distribution of protofilament numbers among MTs in *Xenopus laevis* egg extract. Here 78.7 % of them had 13 protofilaments, 17.8 % had 14 protofilaments and only 3.5 % had other protofilament numbers. If loss of protofilament numbers are the main reason for dynamic instability and loss of three protofilaments are needed for a catastrophe (where loss a is independent of loss a_{+1}), one would not expect such a protofilament distribution at steady state. In addition, 13 to 14 protofilament transitions and vice versa have been demonstrated under various conditions, which means that loss and gain of protofilaments is a reversible process (Chretien et al., 1992).

2.3.3 The relationship between the Mal3 binding site and MT dynamics

Under steady state conditions, the Mal3 signal starts to drop approximately 8 seconds before catastrophe (Maurer et al., 2012) but it has not been examined if catastrophes are a consequence of reduced Mal3 binding or if a reduced Mal3 binding site density resulted in reduced Mal3 signals and catastrophes. Considerable fluctuations in the Mal3 binding site density have been demonstrated here by comparing Mal3-GFP signal

fluctuations on MTs grown in the presence of GTP and GTPγS. These experiments showed large fluctuations favouring an idea of reduced Mal3 binding site densities that cause reduced Mal3 signals and are upstream of the event of catastrophe.

The Mal3 binding site density correlates with momentary stability of MT plus ends and MT ends with lower Mal3 binding site densities have a higher probability to undergo catastrophe **(Fig.11)**. Conceptually, this is somewhat similar to a coupling idea proposed by *Brun et al*. They propose a coupling parameter for terminal tubulin subunits in longitudinal direction. The data presented here for the Mal3 binding site density allow the speculation, that the relative abundance of stabilizing states in lateral direction determine the probability for catastrophe at any given time. When MT depolymerize, protofilaments curl outwards, which means that lateral bonds break before longitudinal bonds. In the simplest idea, the density of Mal3 binding sites (by themselves or simply because their density is a result of the GTP-tubulin density at the very MT ends) reflects the effective opposing force that holds the MT ends together and acts against the intrinsic tendency of the GDP MT lattice to break and outward curling of protofilaments.

Because of the limited resolution of light microscopy, I was not able to determine the exact location of highest density on the individual filament level. Previous studies have reported that the highest EB1 (human analogue of Mal3) binding site is not at the very end of a MT (Nakamura et al., 2012, Maurer, in press). Mal3 binding sites are probably not the very terminal GTP tubulin subunits but may well be conformational transitions of tubulin subunit during the process of adopting the final GDP lattice conformation instead of GTP tubulin. GTP to GDP Pi transition analogues (Beryllium fluoride, GTPγS (Maurer et al., 2011) and Aluminium fluoride, not shown) mimic Mal3 binding states and stabilize MTs, suggesting that Mal3 binding sites are of stabilizing nature.

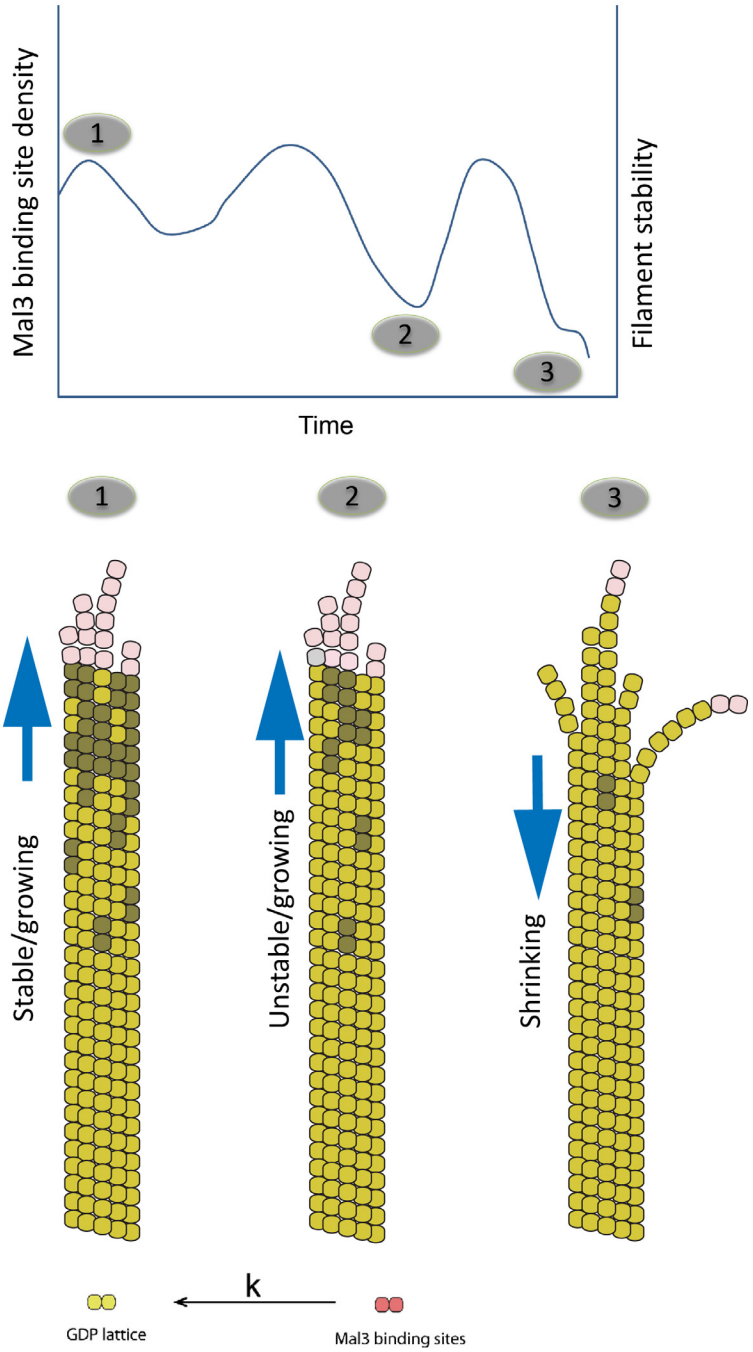

Figure 11: **Mal3 binding site density fluctuations are linked to momentary filament stability**.
The Mal3 binding sites density fluctuates during MT growth episodes over time and this density is proportional to momentary filament stability. High Mal3-densities result in low catastrophe probability (1) whereas low Mal3-binding site densities increase catastrophe probability. The Mal3 binding site density at (3) is not high enough to hold protofilaments together which results in transition to microtubule shrinkage.

After tubulin wash out, the density of Mal3 binding sites decays (see image series **Fig.10d, left**). The rate of transition kinetics at MT ends determines the rate of decay, explaining why Mg^{2+} and Mal3 shorten the waiting time until catastrophe. The initial density at wash out (the starting value) and the rate of decay determine the waiting time until catastrophe, and progressing decay increases catastrophe probability. Assuming an exponential decay of this density, one would expect a somewhat gamma distribution shaped function to fit the distributions of delay times even in the absence of tapering, similar to the fit obtained for longitudinal coupling with coupling parameters $N \geq 2$ (Brun et al., 2009) and in agreement with the obtained distributions of delay times (**Fig.8**). This idea is also consistent with delay time distribution after tubulin dilution for minus ends, which also show a somewhat gamma shaped delay time distribution profile in wash out experiments but do not exhibit strong aging effect under steady state conditions (Odde et al., 1995, Walker et al., 1991).

Tapering increases with the duration of a growth episode and with increased growth speed and fast growing and long MTs are more likely to have pronounced tapering (Coombes et al., 2013). Tapering possibly contributes to MT aging. Minus ends grow slowly compared to plus ends and may depolymerize (due to fluctuations of the Mal3 binding site density/GTP cap density) before tapering has a strong impact on their dynamics. Therefore gamma distribution shaped distributions of delay times after tubulin wash outs are expected and observed for both MT plus ends and minus ends in the presence or absence of tapering.

In addition to Mal3 binding site fluctuations and growth fluctuations, tapering might be the second component necessary to describe dynamic instability and the reason why MT plus ends age in contrast to minus ends under steady state conditions. By changing the time point of wash out and by triggering transition kinetics at MT ends by Mal3 or Mg^{2+}, age/length contributions (potentially due to tapering) and the speed of transition kinetics (potentially related to GTP hydrolysis) could be accessed individually. It was found that transition kinetics have a stronger effect on the delay times after tubulin wash out as compared to the age/length effect.

Tapering destabilized MT ends due to a higher off rate of tubulin as described before. A second consequence would be that the point of highest Mal3 binding site density would be decreased. In a blunt MT end, all protofilaments ends are aligned but they are shifted

relative to each other in a tapered end. Therefore the point of highest Mal3 binding site versus GDP lattice state ratio would be shifted between protofilaments in lateral direction, resulting in a decreased “point of highest Mal3 binding site density” in lateral direction. Therefore, tapering might destabilize MTs in two different ways

Taken together, the data presented in this chapter are in favour of an idea, in which a combination of stabilizing state fluctuations and an evolving tip tapering are the underlying mechanisms for MT dynamic instability and contrast earlier proposals where irreversible and destabilizing defects accumulation over time is responsible for dynamic instability behaviour of MT plus ends (Gardner et al., 2011b, Bowne-Anderson et al., 2013). These finding shed new lights on MT dynamic instability, a fundamental process in the cell which is also target of many therapeutic strategies in the treatment of many cancer types (Marzo and Naval, 2013). Evolutionarily, MT aging is favourable because it prevents the disappearance of very short MTs and also prevents the formation of very long MTs and narrows the length range of MTs within a cell to a window, in which MTs are useful. Transition kinetics rates at MT ends mainly determine MT stability which allows fast adaptation of their dynamics control on multiple levels. While EBs directly affect these rates, other factors may influence different features at MT ends, ultimately changing the probability relationship between Mal3 binding site density and catastrophe. For instance, MCAK has been proposed to favour outward curvature of protofilaments ends, effectively altering the force balance between lateral contacts that hold the MT end together and the tendency of protofilamnts to detach from each other (Asenjo et al., 2013). Fast changes of MT dynamicity are important for global MT rearrangement processes especially at the interphase to mitosis transition where MT dynamicity tremendously increases.

Chapter 3. *In Vitro* Dissection of the Functional Interplay between Core Components of the Microtubule Plus End Tracking Network

3.1 Introduction

+TIPs accumulate at growing MT plus ends and are crucial for MT dynamics control and spatiotemporal arrangement of MTs. EBs form the core of a complex +TIP network. The majority of known +TIPs depend directly or indirectly on EBs for plus end accumulation. How EB dependent +TIPs directly influence each other is not well understood but important in order to understand how +TIP work as a system to regulate MT behaviour. p150 is a crucial component of this network as it directly stabilizes MTs and is implicated in targeting a minus end directed motor to theses ends, crucial for cargo transport along MTs (Duellberg et al., 2013).

p150 is a component of the dynactin complex and has been shown to have a stabilizing effect on MTs *in vitro* and neuronal cells (Lazarus et al., 2013) and to be an important regulator of the minus end directed motor protein complex dynein (Schroer, 2004). p150 accumulates at growing MT ends and contributes to the enrichment of the dynein motor complex at growing MT plus ends (Moughamian et al., 2013, Splinter et al., 2012). For this end accumulation the CAP-Gly domain of p150 is required (Vaughan et al., 2002, Moughamian and Holzbaur, 2012) which mediates interactions with EBs and CLIP170, which are both needed for plus end tracking of dynactin/p150 in cultured cells (Lansbergen et al., 2004, Watson, 2006).

Homozygous mice with the G59S mutation in the CAP-Gly domain of p150 are not viable as well as homozygote p150 null mice (Lai et al., 2007). Several other point mutations within the CAP-Gly domain of p150 lead to severe neuronal disorders in human patients (Farrer et al., 2009, Stockmann et al., 2013). These mutation do not abolish MT binding but abolish binding to EB1 (Ahmed et al., 2010). As a consequence, lack of p150 enrichment at MT ends impairs the initiation of dynein/dynactin-dependent retrograde vesicle transport from the very distal end of neurites whereas vesicle

transport in the middle parts of neurits is not strongly affected by these mutations (Moughamian and Holzbaur, 2012). This underlines that correct intracellular localisation of the dynactin/dynein complex is indispensable for proper neuronal development and functioning.

A molecular understanding of the mechanism of p150 end tracking and its ability to recruit dynein to growing MT ends would significantly improve our understanding of these neuronal disorders and would also be potentially beneficial for the evaluation of therapeutic strategies.

In order to understand the molecular mechanism of how dynactin/dynein is targeted to growing MT ends, an *in vitro* reconstitution approach with purified proteins was chosen. The advantage of an *in vitro* approach is its reduced complexity in comparison to cell based experiments and that the contribution of each protein to system dynamics can be accessed individually in a controlled fashion.

In the presented work I show that EBs are necessary and sufficient for p150 end tracking *in vitro*. However, SXIP motif containing proteins -the other known class of EB dependent end tracking proteins (Akhmanova and Steinmetz, 2010) - compete with p150 for EB binding which could explain in addition to EBs, CLIP170 is needed to target p150 to growing MT ends. It is shown here that CLIP170 can restore p150 end tracking in the presence of competitors by providing additional binding sites for p150 at growing MT ends where SXIP motifs do not bind to. Finally, p150 and EB1 have been identified as the minimal set of activities that target the dynein complex to growing MT ends.

3.2 Results

3.2.1 EB1 targets p150 to growing MT ends *in vitro*

Purified full length p150 derived from baculovirus infected insect cells was not soluble on its own (not shown, also reported in (Lazarus et al., 2013)) but fragments lacking the dynactin integration domain have been shown to be soluble and comprise the ability to bind MTs, the dynein complex and EB1 *in vitro* (Miura et al., 2010, Culver-Hanlon et al., 2006, Hayashi et al., 2005). I therefore tested if fragments lacking the dynactin integration domain could be used as surrogates as they should comprise all necessary

features with respect to plus end tracking and dynein interaction. I generated an expression construct for mammalian cells comprising an EGFP for visualization, the n terminal 218 amino acids of p150 (as detailed in a scheme in **Fig.12b**) and a GCN4 sequence for artificial dimerization (Ciani et al., 2010) because p150 dimerizes (see below) and each dynactin complex contains two p150 subunits (Schroer, 2004).

Live cell imaging of transiently transfected CHO cells showed comet shaped GFP signals that moved at typical speeds of MT growth through the intracellular space of these cells (**Fig.12c**); this shows that the n terminus of p150 harbours all features required for plus end tracking and that integration into the dynactin complex is not required for this process, consistent with earlier proposals (Vaughan et al., 1999).

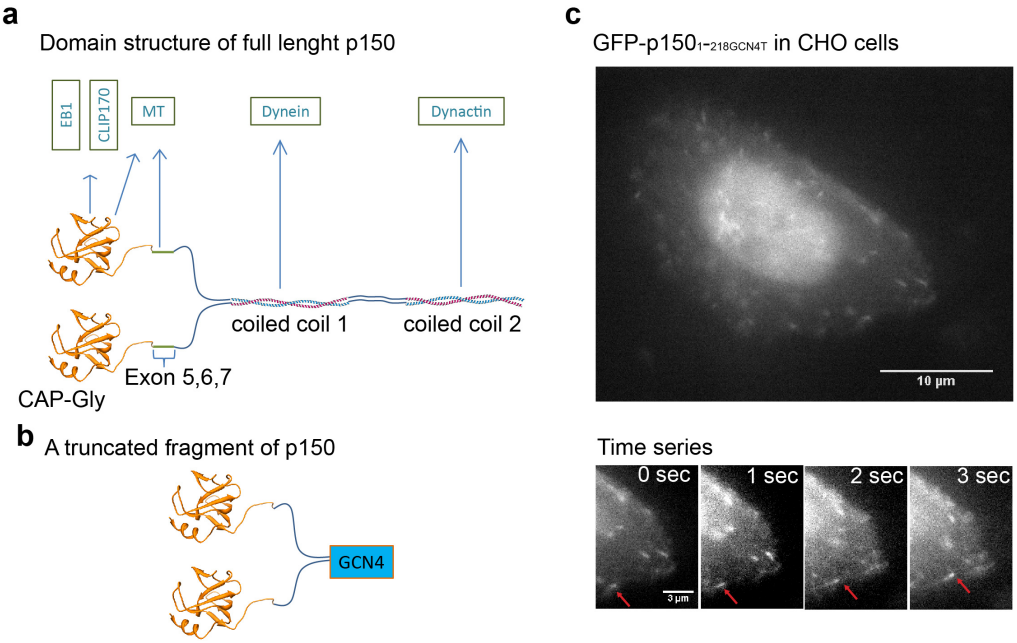

Figure 12: Dynactin integration is not required for p150 plus end tracking in CHO cells

(**a**) Domain structure of full length p150. The N terminal CAP-Gly domains interact with EBs, CLIP170 and MTs. The CAP-Gly domain is followed by a positively charged stretch encoded by Exon 5,6, and 7 which is present only in the neuron specific splice variant of p150. This stretch enhances binding to MT. The coiled coil 1 part mediates interaction to the dynein motor complex and mediates dimer formation of p150. Coiled coil 2 is responsible for insertion into the dynactin complex. Crystal structure for a CAP-Gly domain was taken from the protein data base (code 1LPL) and represents F53F4.3 from *Caenorhabditis elegans*, the first crystal reported crystal structure of a CAP-Gly domain (Li et al., 2002) (**b**) Scheme of a truncated n terminal fragment of p150 used for transient transfection of CHO cells as depicted in (c). The fragment lacks dynactin and dynein interaction domain, and the amino acids encoded by exon 5,6, and 7, which are present in the neuron specific isoform of p150 only. (**c**) Live cell imaging of a CHO cell, expressing a GFP tagged fragment of p150 as shown in (b) by epi-flurecence microscopy. The GFP signals appear as comet shaped spots (upper) that move with typical speeds of MT growth as shown by a time series (lower). The arrow follows one of these signals throughout the time series.

To test the mechanisms of p150 plus end tracking *in vitro* using a bottom up approach, two constructs for purification of p150 were designed. p150 is expressed in a neuron specific isoform and an ubiquitously expressed version that lacks exon 5, 6 and 7 that is found in all dividing cells (Zhapparova et al., 2009, Dixit et al., 2008). Both isoforms accumulate at growing MT ends in their respective cell type (Lansbergen et al., 2004, Moughamian and Holzbaur, 2012). To test the mechanisms of p150 plus end *tracking in vitro*, I used mCherry tagged fragments of both isoforms referred to as mCherry-$P150_{1-547N}$ for the neuronal version and mCherry-$P150_{1-547T}$ for the "tissue isoform" to directly compare these isoforms with respect to their ability to interact with MTs and their requirements for plus end tracking. A schematic representation of these constructs is depicted in **Fig.13**.

Both constructs could be purified from *E. coli* and had similar gel filtration profiles. Using SEC-MALS I obtained an average mass for mCherry-$P150_{1-547N}$ of 184.5 kDa (±3 kDa) which is close to the calculated mass for a dimer (197.4 kDa; not shown) indicating that both fragments form homodimers.

I next tested if unlabelled EB1 alone would be sufficient to target the mCherry labelled p150 fragments to growing MT ends *in vitro* using a well-established plus end tracking reconstitution assay (Telley et al., 2011, Bieling et al., 2007). Strikingly, both p150 isoforms were specifically enriched at growing MT ends in the presence of unlabelled EB1 (**Fig.13**). In the absence of EB1, mcherry-$P150_{1-547T}$ showed very weak binding along the MT lattice (**Fig.13d, right**) while mCherry-$p150_{1-547N}$ bound along the MT lattice with moderate affinity (**Fig.13e, right**). A higher affinity of the neuronal isoform for the MT lattice has been reported earlier using MT pelleting assays (Zhapparova et al., 2009) and can be well explained by the positive net charge of the amino acids encoded by exon 5, 6 and 7.

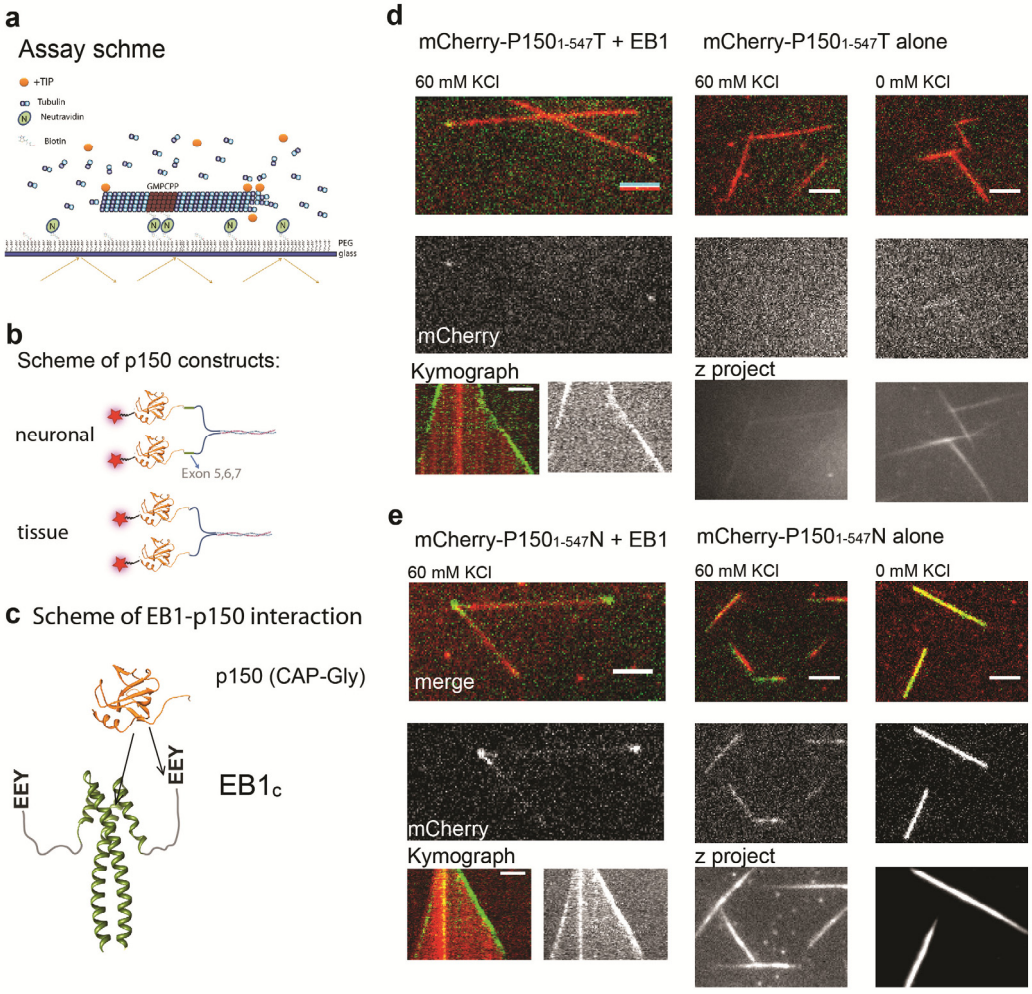

Figure 13: EB1 targets p150 to growing MT ends in vitro

(a): Scheme of in vitro +TIP reconstitution assay (**b**): Overview of the domain structure of p150 constructs used for *in vitro* experiments. The domain organization in full length p150 is depicted in Fig.11. The neuronal splice variant contains exons 5,6,and7 which are lagging in the non neuronal splice variant. Otherwise, both isoforms are identical on the level of their primary sequnce (**c)** Scheme of EB1 – p150 interaction. p150 and EB1 form two contacts, one involving the flexible c terminal tail of EB1 and the other involves the hydrophobic cavity of EB1 (**d)** left: EB1 (150 nM) targets mCherry-P150$_{1\text{-}547}$T (125 nM) to growing MT ends. Depicted are a merged single frame images, (upper, tubulin in red, p150 in green) the mCherry channel (middle) and a representative kymograph (lower; left: mCherry channel, right: merge with tubulin channel, scale bar for all images: 3 µm, total duration of kymographs is 2 minutes)). Right: in the absence of EB1, mCherry-P150$_{1\text{-}547}$T (125 nM) binds weakly to the MT lattice in a salt dependent manner. Single frame images of a merge with the MT channel (upper) the mCherry channel only (middle) and an average intensity z projection of the mCherry channel of 60 frames (lower) are depicted for 2 salt concentrations as indicated. (**e**): same as in (d**)** for the neuronal isoform of p150 (P150$_{1\text{-}547}$N, also at 125 nM). Both constructs behave similarly but the neuronal isoform binds more strongly to the MT lattice.

A recent paper reported that EB alone is not sufficient to target an artificially dimerized shorter fragment of p150 to growing MT ends. Very similar to the construct used in

Fig.11 for transient CHO cell transfection, the n terminal 218 aa of p150 are dimerized by GCN4 (Moughamian et al., 2013). I tested this fragment (called GFP-P150$_{1\text{-}218GCN4N}$ and derived from that: GFP-p150$_{1\text{-}218GCN4T}$ for the non neuronal splice variant). Again, EB1 was able to recruit both p150-fragments to MT ends *in vitro* (**Fig.14** and **Fig.19b**) although the ionic strength of the buffer had to be increased for GFP-p150$_{1\text{-}218GCN4N}$ because of its stronger affinity to the MT lattice. The n terminal part of p150 has a positive net charge while the natural coiled coli 1 domain is negatively charged. These negative charges are absent in the artificial GCN4 coiled coil (based on calculated values from http://web.expasy.org/compute_pi/). Thus the increased MT lattice affinity of the artificial dimers is probably due to a lack of these negative charges (tubulin is overall negatively charged). However, the main reason why *Moughamian et al* did not observe EB mediated end tracking of their p150 fragment might be the use of a chemically labelled EB1 construct in which dyes could block essential interactions between EB1 and p150 (Moughamian et al., 2013).

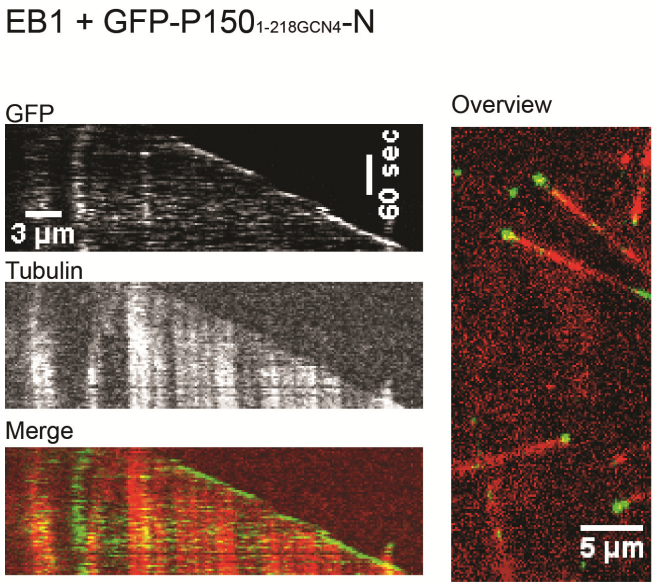

Figure 14: EB1 targets an artificially dimerized p150 construct to growing MT ends

Unlabelled EB1 (150 nM) targets GFP-P150$_{1\text{-}218GCN4}$N (10 nM) to growing MT ends in vitro. Left: Representative kymograph of the indicated channels (Upper and middle) and a merge (lower) with the MT channel in red and GFP-P150$_{1\text{-}218GCN4}$N in green. Right: Single frame of a merge between the MT channel (red) and the GFP-P150$_{1\text{-}218GCN4}$N channel (green). Final imaging buffer was supplemented with additional 25 mM KCl and 85 mM K-Acetate

Taken together, this shows that EB1 is necessary and sufficient to target CAP-Gly domain containing fragments of p150 to growing MT ends in a minimal *in vitro*

reconstitution system. This is in apparent contradiction to the situation in the cell, where EBs are not sufficient for p150 end tracking (Lansbergen et al., 2004, Watson, 2006).

3.2.2 SXIP motifs and CapGly domains compete for EB1 binding

A direct interaction between EB1 and p150 is well described *in vitro* and has been further supported by co- immunoprecipitations from cell extracts (Hayashi et al., 2005, Sun et al., 2008, Honnappa et al., 2006). In cells however, EB1 is necessary but not sufficient for p150 end tracking. Here knock down of CLIP170 results in a loss of p150 at growing MT ends similar to knock down of EBs (Lansbergen et al., 2004, Watson, 2006). In a minimal *in vitro* system however, CLIP170 is dispensable (this work). A possible explanation would be that in the cell, other proteins compete with p150 for EB binding which are absent *in vitro*. Beside CAP-Gly domains, the SXIP motif is the only other known motif within +TIPs that binds directly to EBs. Co crystal structures have been solved for EBc-p150 and EBc-SXIP-motif (Hayashi et al., 2005, Honnappa et al., 2006, Honnappa et al., 2009b). However, it was not obvious from these data, if SXIP-motifs and CAP-Gly domains could simultaneously bind to EBs or in which way they would influence each other in terms of EB binding (Kumar and Wittmann, 2012, Honnappa et al., 2009b, Duellberg et al., 2013). To address this question I added an SXIP motif containing peptide to the *in vitro* reconstitution +TIP system.

A well described bona fide +TIP with an SXIP motif is MACF/ACF7 (Honnappa et al., 2009b) which links growing MT ends to the actin network (Leung et al., 1999). To test how CAP-Gly domains and SXIP motifs influence each other with respect to EB mediated plus end tracking, I used a MACF derived 39 aa long SXIP motif containing monomeric peptide (called MACF-$_{SXIP}$)(**Fig.15a&b**). Its functionality was tested using a FITC labelled version of this peptide. As expected FITC-MACF-$_{SXIP}$ was targeted to growing MT ends by EB1 (**Fig.15c**). An EB mutant (EB1$_{Y217A,E225A}$) with two point mutations within the hydrophobic cavity of EB1 failed to target FITC-MACF-$_{SXIP}$ to growing MT ends as predicted from the available crystal structure (Montenegro Gouveia et al., 2010, Honnappa et al., 2009b), supporting a proposed binding mode that involves the hydrophobic cavity of EB1.

I next tested how MACF-$_{SXIP}$ peptides would influence EB1 mediated end tracking of mcherry-P150$_{1-547T}$. While a control peptide in which the sequence SKIP was changed

to SXNN (MACF-$_{SXNN}$, see scheme in **Fig.15a**) did not alter EB1 mediated end tracking of mCherry-P150$_{1-547T}$, the same amount of the SXIP containing peptide completely abolished EB mediated end tracking of mCherry-P150$_{1-547T}$.(**Fig.15d**) This shows that SXIP motifs act as a competitors with p150 for EB1 binding which could explain why EB1 is sufficient for p150 end tracking in a minimal *in vitro* system but not sufficient in cells due to the presence of other competitors.

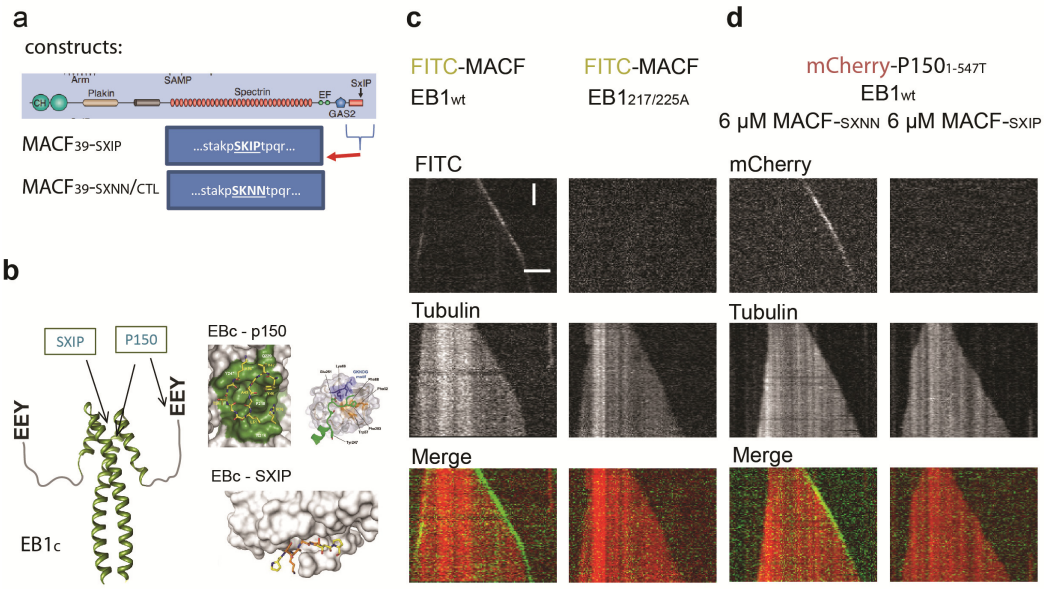

Figure 15: SXIP motifs can disrupt EB1 mediated end tracking of p150

(a) Scheme of the domain structure of MACF and the SXIP peptides derived from it. For control experiments, the natural sequence (SKIP) was changed to SKNN as depicted. **(b)** Scheme of the interaction between EB/SXIP motive and EB/P150 and the corresponding crystal contacts revealed by x ray crystallography (taken from (Hayashi et al., 2005, Honnappa et al., 2009a, Honnappa et al., 2006) . (**c**) EB1 (150 nM) targets the SXIP containing MACF fragment (150 nM; here labelled with FITC dye) to growing MT ends. The EB1$_{Y217A/E225A}$ mutant (150nM) fails to target MACF-FITC to growing MT ends. Representative kymographs for each condition are depicted with channels as indicated. Merge: tubulin in red and FITC-MACF in green. Scale: 3 µm and 20 seconds. (**d**) The control peptide MACF-$_{SXNN}$ (6 µM) does not impair EB1 (150 nM) mediated end tracking of mCherry p150$_{1-547}$T (75 nM) while the same concentration of MACF-$_{SXIP}$ (6 µM) completely abolishes EB1 mediated end tracking of mCherry P150$_{1-547}$T (75nM). Representative kymographs for each condition are depicted with individual channels as indicated. Merge: tubulin in red and p150$_{1-547}$T in green. Scale: 3 µm and 20 seconds.

This raises the question of how CLIP170 contributes to p150 end tracking in cells in the presence of competitors. I therefore introduced CLIP170 into the *in vitro* reconstitution system. I first confirmed that human EB1 can target full length GFP-CLIP170 to growing MT ends (**Fig.16b, left**) as it has been shown previously for *Xenopus laevis*

EB1 (Bieling et al., 2008a). Qualitatively, MACF-$_{SXIP}$ peptides also abolished GFP-CLIP170 end tracking by EB1 but ~ two fold higher MACF-$_{SXIP}$ concentrations were needed to fully displace GFP-CLIP170 as compared to mCherry-P150$_{1\text{-}547T}$ (**Fig.16b)** also compare to **Fig.15d**). This could be attributed to an increased affinity of CLIP170 to EB1, enhanced interaction with MTs ends due to the additional two CAP-Gly domains and/or differences in the binding mode between CLIP170 and EB versus p150 to EB1.

To test if different affinities might be at least in part responsible for the observation, that higher MACF$_{\text{-}SXIP}$ concentrations are needed to displace CLIP170 from growing MT ends in the presence of EB1 as compared to P150$_{1\text{-}547T.}$, I performed analytical gel filtration experiments to compare the affinities in a semi-quantitative manner. Full length CLIP170 was not soluble enough under the used assay condition and a fragment that lacks the c terminus (called CLIP170ΔC or CLIP170H2) was used as described in (Scheel et al., 1999). EB1 and GFP-CLIPΔC formed a stable 1:1 complex at equi-molar concentrations. In contrast, a considerable fraction of uncomplexed EB1 was observed for a 1:1 ratio of EB1 and mcherry-P150$_{1\text{-}547N}$ and a molar ratio of 3:1 (P150:EB1) was required to remove all uncomplexed EB1 (**Fig.16c**).

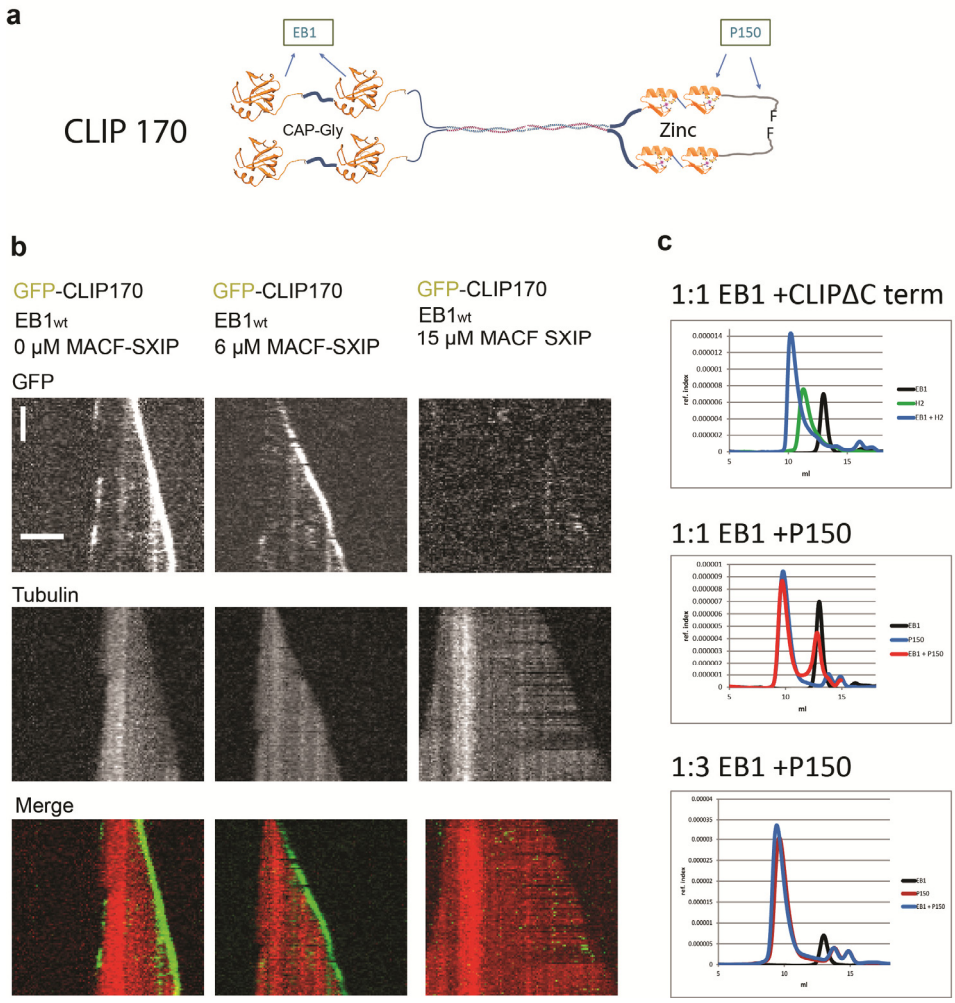

Figure 16: Higher SXIP peptide concentrations are required to disrupt EB1 mediated end tracking of CLIP170

(a) Domain structure of CLIP-170. (**b**) EB1 (150 nM) targets GFP-CLIP170 (75nM) to growing MT ends (left). While 6 µM MACF-$_{SXIP}$ abolished mCherry-p150$_{1\text{-}547T}$ end tracking at the same concentrations (see Fig14) GFP-CLIP170 is still enriched at MT ends (middle). Increasing the MACF-SXIP concentration to 15 uM abolishes EB1 mediated GFP-CLIP170 end tracking (right). Representative kymographs for each condition are depicted with individual channels as indicated. Merge: tubulin in red and GFP-CLIP170 in green. Scale: 3 µm and 20 seconds. **(c)** analytical gel filtration of EB1 and CLIP170ΔCterm at a molar 1:1 ratio (both 12 µM, upper) and for P150$_{1\text{-}547}$N and EB at equimolar ratios (middle, both 12 µM) or at a 1:3 ratio with p150 at 36 µM).

Taken together this shows that SXIP peptides compete with both CAP-Gly domain containing proteins for EB1 binding and that higher concentration of MACF-$_{SXIP}$ peptides are needed to displace GFP-CLIP170 from growing MT ends as compared to mCherry-P150$_{1\text{-}547T}$.

Vice versa unlabelled CLIP170 abolished EB1 mediated end tracking of FITC-MACF-$_{SXIP}$ demonstrating that SXIP motifs and CAP-Gly domain binding to EB1 is mutually exclusive and a general feature of EB mediated plus end tracking (**Fig.17**).

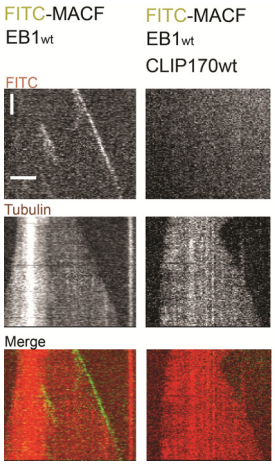

Figure 17: Mutually exclusive binding of SXIP motifs and CAP-Gly domains to EB1

EB1 (150nM) targets FITC-MACF (150nM to growing MT ends (left). Addition of 660 nM CLIP170wt abolishes EB1 mediated plus end tracking of FITC-MACF (right). Representative kymographs for each condition are depicted with individual channels as indicated. Merge: tubulin in red and FITC-MACF in green. Scale: 3 µm and 20 seconds.

3.2.3 CLIP170 restores p150 end tracking in the presence of EB1 and competitors

In cells, p150 localization depends on EBs and CLIP170 (Lansbergen et al., 2004, Watson, 2006). EBs are not sufficient for p150 end tracking, probably due to competition for EBs by SXIP proteins.

I next tested if CLIP170 can directly restore EB dependet end tracking of p150 in the presence of competitors *in vitro*. I chose conditions were MACF-$_{SXIP}$ completely displaced mCherry-P150$_{1\text{-}547T}$ (as in **Fig.15**) from growing MT ends in the presence of EB1 and then added GFP-CLIP170 to the experiment. Strikingly mCherryP150$_{1\text{-}547T}$ was again enriched at growing MT ends (**Fig.17a&b**).

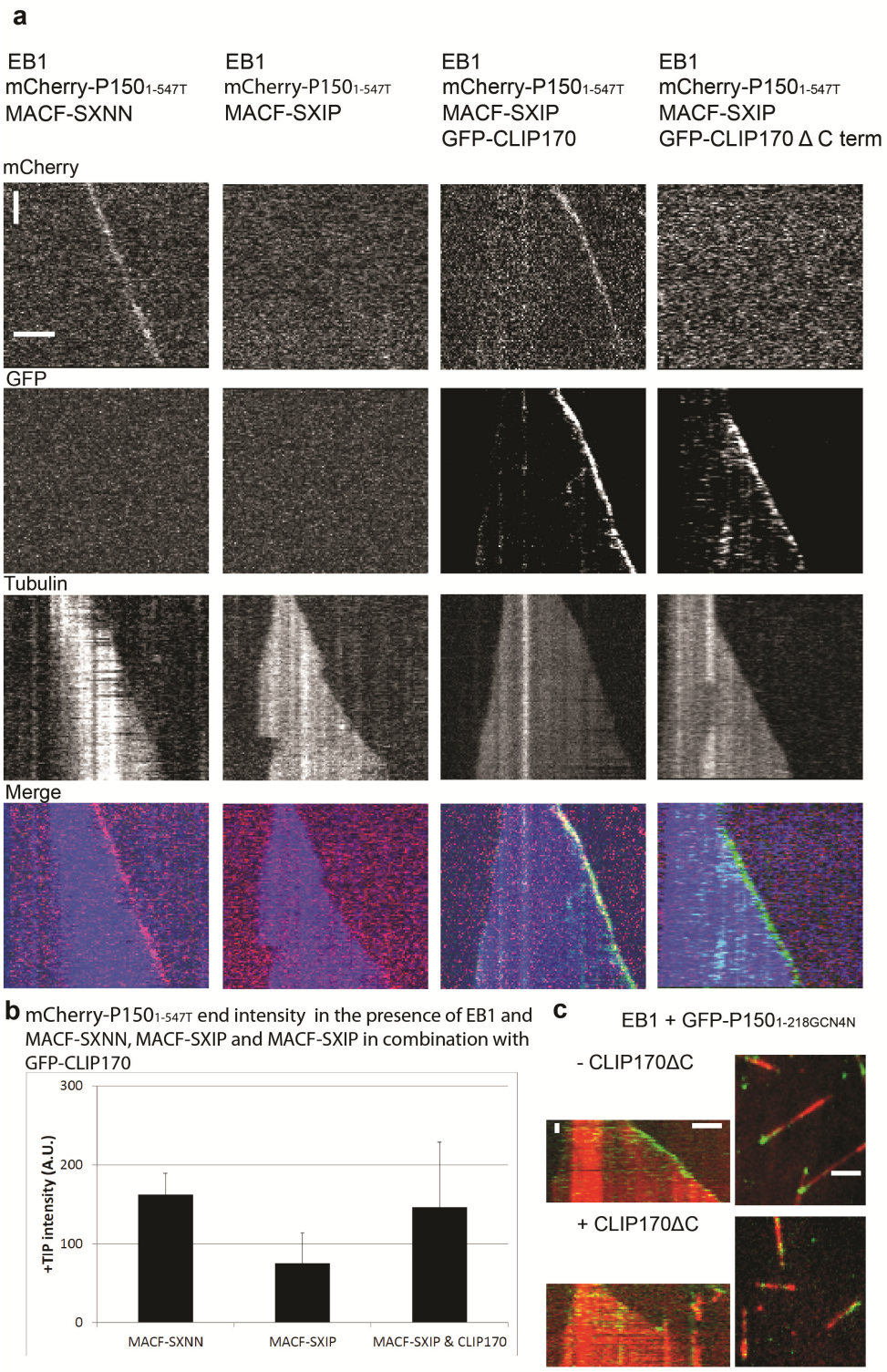

Figure 18: CLIP170 restores EB1 dependent p150 end tracking in the presence of SXIP peptides

(**a**)150 nM EB1 target 75 nM mCherry-P150$_{1\text{-}547}$T to growing MT ends in the presence of 6 µM MACF-$_{SXNN}$ (left). 6 µM MACF-$_{SXIP}$ abolish EB1 mediated end tracking of 75 nM mCherry-P150$_{1\text{-}547}$T (middle left) (also shown in Fig. 14d). Adding 75 nM of full length GFP-CLIP170 to

150 nM EB1, 6µM MACF-SXIP and 75 nM mCherry-$P150_{1-547}T$ restores end tracking of mCherry-$P150_{1-547}T$ (middle, right). Adding 75 nM GFP-CLIP170ΔC to 150 nM EB1, 6µM MACF-SXIP and 75 nM mCherry-$P150_{1-547}T$ did not restore end tracking of mCherry-$P150_{1-547}T$. Representative kymographs for each condition are depicted with individual channels as indicated. Merge: tubulin in blue, GFP-CLIP170 in green and mCherry-$P150_{1-547}T$ in red. Scale: 3 µm and 20 seconds (**b**) Quantification of mCherry-$P150_{1-547}T$ fluorescence intensity at growing MT ends. mCherry-$P150_{1-547}T$ signals were averaged from growth episodes of at least 30 frames from least 10 individual MTs per condition (material and method, image analysis). The comet peak intensities (± Stedev) are plotted as indicated. (**c**) 150 nM EB1 targets 10 nM GFP-$_{P1501-218GCN4}N$ to growing MT ends in the absence (upper) but not in the presence (lower) of unlabelled CLIP170ΔC (660 nM). Final imaging buffer was supplemented with additional 25 mM KCl and 85 mM K-Acetate. Representative kymographs (left) and overview images (right) are depicted with MTs in red and GFP-$P150_{1-218GCN4}N$ in green.

I next studied the underlying mechanisms of how CLIP170 restores p150 end accumulation in the presence of competitors. CLIP170 could provide additional binding sites for p150 with its c terminal part while the n terminus binds composites of α tubulin and EB1 at MT plus ends. Alternatively the CAP-Gly domains of p150 and CLIP170 could co-operatively bind to EB1. To distinguish between the two possibilities I tested if a fragment that lacks the c terminal domain (CLIP170ΔC) rescues p150 end tracking in the presence of EB1 and competitors. While GFP-CLIP170ΔC tracked growing MT ends in the presence of EB1 and MACF-$_{SXIP}$ (similar to full length CLIP170) it failed to target $P150_{1-547T}$ to growing MT ends under these conditions. In fact, CLIP170ΔC acted as an additional competitor for EB1 binding as an excess of unlabelled CLIP170ΔC could displace P150 from growing MT ends (**Fig.18c**).

This shows that full length CLIP170 is needed to restore p150 end tracking and provides an explanation of how CLIP170 positively influences end accumulation of p150 in cells: Its n terminal CAP-Gly domains bind more efficiently to EB1/α-tubulin while its c terminal zinc binding domains provide new binding sites for p150 where SXIP motifs do not bind to.

3.2.4 CLIP170-mediated recruitment of p150 does not require a direct EB1-p150 interactions

I next wanted to find out, if EB1 and CLIP170 dependent end tracking of p150 requires simultaneous binding of p150 to EB1 and CLIP170. To test that, I generated an artificial fusion between EB1 (lacking the last 4 amino acids) and the last 40 amino acids of CLIP170, referred to as EB-CLIPc (**Fig.19a**). This fusion was able to target both FITC-

MACF-$_{SXIP}$ and GFP-P150$_{1\text{-}218GCN4T}$ to growing MT ends (**Fig.19b**) which indicates that the hydrophobic cavity within the EB1 part as well as the CLIP170 derived c terminus within the fusion are intact. If p150 would bind obligatorily to composites of EB1 and CLIP170 one would expect that SXIP peptides could displace p150 from growing MT ends in the presence of EB-CLIPc. If binding to EB1 or the c terminal part of CLIP170 is sufficient for efficient end tracking one would not expect a strong impact of the MACF-$_{SXIP}$ peptide.

To distinguish between the two possibilities, I added MACF$_{\text{-}SXIP}$ to EB-CLIPc and GFP-P150$_{1\text{-}218GCN4T}$ and tested if p150 would be displaced from growing MT ends. Concentration of up to 60 µM MACF$_{\text{-}SXIP}$ did not abolish EB-CLIPc mediated end tracking of GFP-P150$_{1\text{-}218GCN4T}$ (**Fig.19.b**). This demonstrates that the c terminal part of CLIP170 has indeed the ability to provide new binding sites for p150 in order to facilitate end accumulation of p150 and further shows that the c terminus of CLIP170 by itself is sufficient for that i.e. p150 does not need to bind EBs and CLIP170 simultaneously.

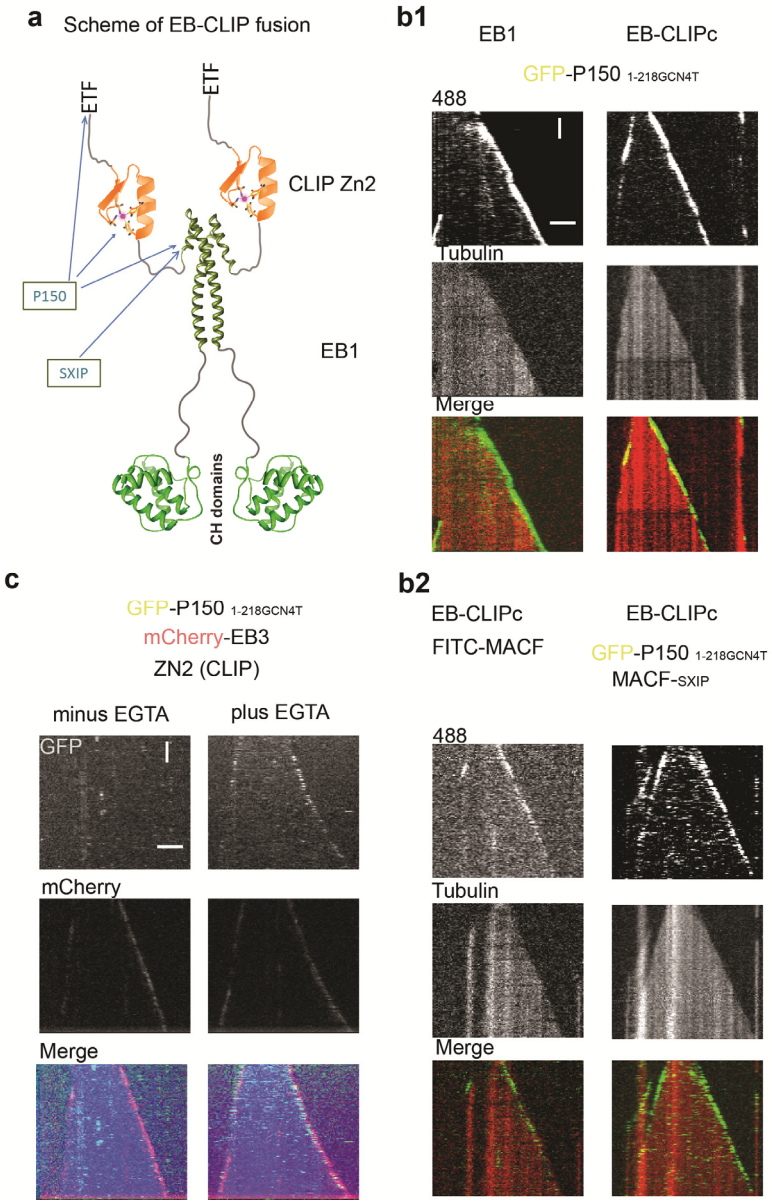

Figure 19: CLIP170-mediated recruitment of p150 does not require a direct EB1-p150 interaction

(**a**) Scheme of the EB-CLIPc fusion. The last (c terminal) 4 amino acids of human EB1 were replaced by the c terminal 40 amino acids of human CLIP170 (containing the distal zinc knuckle and the acidic ETF tail). The fusion has the EB1 hydrophobic cavity (interaction with SXIP and p150), and the zinc knuckle/ETF tail motif to interact with p150. EB-CLIPc does not have the EB1 EEY tail motif. An n terminal HIS-Thioredoxin tag is not depicted. (**b**) Similar to wild type EB1 (150 nM, left) EB-CLIPc (150 nM) recruits GFP-$_{P1501\text{-}218GCN4}$T (20 nM) to growing MT ends (**b1, right**) as well as FITC-MACF (150 nM) (**b2**, left). (**2b, right**) An excess of unlabelled MACF-$_{SXIP}$ peptide (60µM) does not displace GFP-P150$_{1\text{-}218GCN4}$T (20 nM) from growing MT ends in the presence of the EB-CLIPc fusion (150 nM). Representative kymographs for each condition are depicted with individual channels as indicated. Merge: tubulin in red, GFP-P150$_{1\text{-}218GCN4}$T green. Scale: 3 µm and 20 seconds. (**c**) Localisation of GFP-P150$_{1\text{-}218GCN4}$T (20nM) and mCherry-EB3 (75nM) in the presence of unlabelled 660 nM ZN2(CLIP) (c terminal 40 amino acids of CLIP170) in the absence (left) and presence (right) of 5mM EGTA. EGTA binds zinc ions and therefore is expected to unfold the zinc knuckle

domain of CLIP170. mCherry-EB3 is enriched at growing MT ends independently of ZN2(CLIP) and 5 mM EGTA. ZN2(CLIP) efficiently sequesters GFP-$_{P1501\text{-}218GCN4}$T in the absence of EGTA (no GFP signal at growing MT ends, left). Sequestering of GFP-$_{P1501\text{-}218GCN4}$T by ZN2(CLIP) is strongly impaired in the presence of EGTA (right, GFP-$_{P1501\text{-}218GCN4}$T is enriched at growing MT ends).
.

p150 binds to the very c terminal EEF motif of CLIP170 which is structurally very similar to the c terminus of EB1 (EEY). In addition, p150 interacts with a zinc knuckle containing region of CLIP170 (Weisbrich et al., 2007). Simultaneous imaging of mCherry-EB3 and GFP-P150$_{1\text{-}218GCN4T}$ revealed that an unlabelled c terminal CLIP170 fragment could sequester GFP-P150$_{1\text{-}218GCN4T}$ while normal end tracking of mCherry-EB3 was observed (**Fig.19c**). The addition of EGTA (which binds to zinc and is commonly used to interfere with zinc finger mediated interaction (Sun et al., 1996)) weakened this sequestering effect and GFP-P150$_{1\text{-}218GCN4T}$ was again enriched at MT plus ends (**Fig.19c**). This shows that composite binding of p150 to the ETF motif of CLIP170 and a properly folded zinc binding domain are needed for efficient interaction.

Taken together, this shows that CLIP170 can bind to EB1 via its n terminal CAP-Gly domains and provides –at the same time – new binding sites for p150 at MT ends via its c terminal zinc binding domain, effectively increasing the amount of p150 at MT ends in the presence of competitors for EB1. p150 can bind to either EB1 or CLIP170 for its end tracking but does not require composite binding to these two proteins. SXIP motifs do compete with p150 for EB binding but not for binding to the c terminus of CLIP170.

3.2.5 EB1 and p150 target the dynein complex to growing MT ends

End accumulation of the minus end directed motor protein complex dynein is crucial for the initiation of retrograde vesicle and organelle transport (Moughamian and Holzbaur, 2012). MT plus end accumulation of the dynein complex depends on EB1 and p150 but it is not clear if these two activities on their own are sufficient to target the dynein complex to growing MT ends.
Strikingly the human recombinant GFP labelled dynein complex was targeted to growing MT ends via EB1 and mCherry-P150$_{1\text{-}547T}$ (**Fig.20**). In the absence of p150,

EB1 alone failed to target the dynein complex to growing MT ends (**Fig20**). The cc1 part of p150 (see scheme in **Fig.12**) interacts with the dynein complex via the intermediate chain of dynein (Vaughan and Vallee, 1995). In good agreement with this result, an artificial homodimer of two dynein heavy chains without accessory subunits was not recruited to growing MT ends by EB1 and mCherry-P150$_{1\text{-}547T}$ (**Fig.20**).
This identifies the minimal set of activities sufficient for dynein plus end tracking which probably resembled the situation in neuronal cells whereas more complex mechanism seems to be present in other cell types (see discussion).

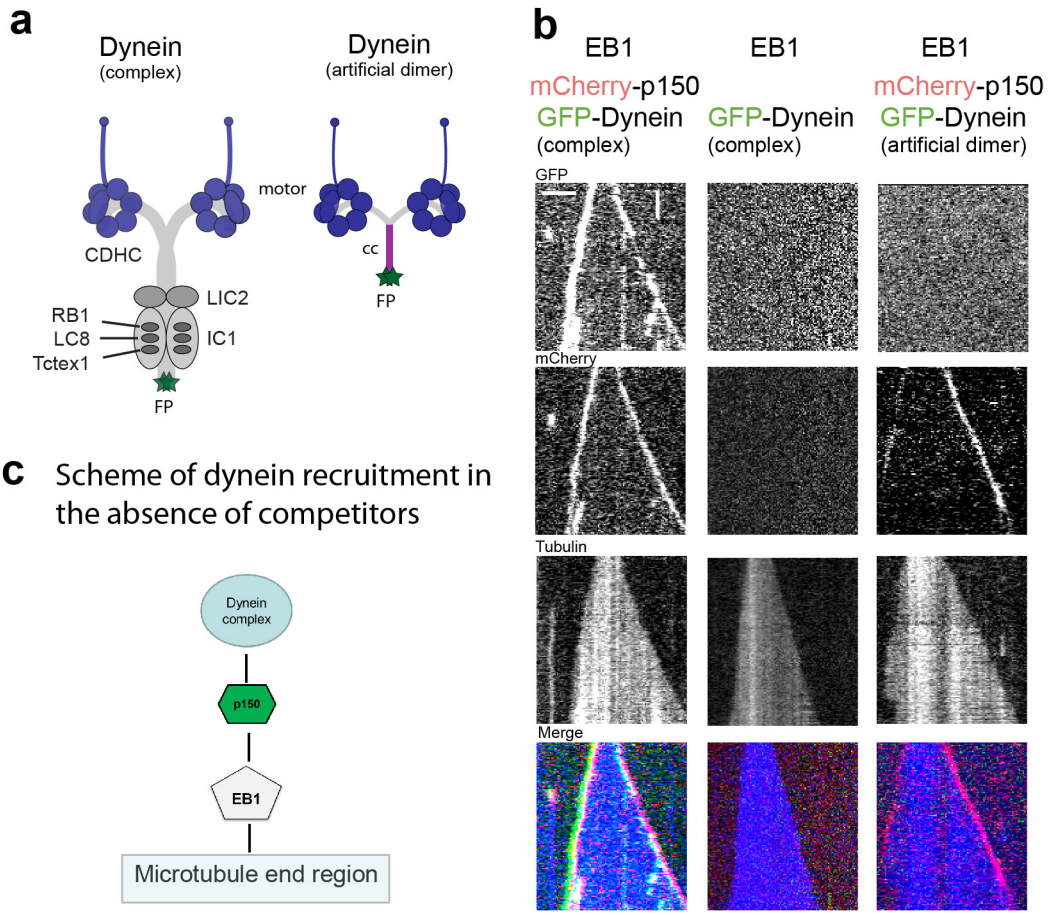

Figure 20: EB1 and p150 target the dynein complex to growing MT ends

(a) Schematic representation of the human dynein complex (left) and a dimer of the two motor domains (right) as used for experiments in this figure (**b**)(**left**) EB1 (200 nM) and mCherry-P1501-547T (125 nM) target the GFP-dynein complex (14 nM) to growing MT ends. Dynein was used as described in (Trokter et al., 2012) and purified by Martina Trokter and Rupam Jha. (**middle**) EB1 alone (200 nM) does not target the GFP-dynein complex to growing MT ends (14 nM). (**right**) EB1 (200nM) and mCherry-P1501-547T (125 nM) do not target an artificial dimer of the two motor domains to growing MT ends. Representative kymographs for

each condition are depicted with individual channels as indicated. Merge: tubulin in blue, GFP-dynein in green and mCherry-P150$_{1-547}$T . Scale: 3 µm and 20 seconds. The ionic strength of this experiment set was lowered (as compared to "standard TIRF buffer, see material and methods) to 60 mM K-PIPES and 45 mM KCl) All other buffer components remained unchanged. (**c**) Scheme illustrating the hierarchical recruitment of the human dynein complex by EB1 and the dynactin component p150 in the absence of competitors.

3.3 Discussion

In this chapter EB1 and CLIP170 dependent MT plus end tracking of N terminal fragments of p150 was reconstituted *in vitro* for the first time. It was further shown that SXIP motifs and CAP-Gly domain competition for EB binding is a general feature of the +TIP network. A mechanism of how CLIP170 positively influences p150 end tracking in the presence of SXIP competitors has been revealed, in which CLIP170 plus end tracks via EB1 and – at the same time – provides new binding sites for p150 at its c terminus to which SXIP peptides do not bind to. This solves the apparent contradiction between *in vitro* studies with purified proteins that reported a direct interaction between p150 and EB1 and the cell biology literature, that showed that EBs are necessary but not sufficient for p150 plus end tracking. In addition it was shown that –in an *in vitro* system – EB1 and p150 are necessary and sufficient to target the dynein complex to growing MT ends, one of the major functions attributed to p150/dynactin (**Fig.21**).

3.3.1 Competition for EBs is a general theme of the +TIP network

EBs are sufficient for p150 end tracking *in vitro* but not in a cellular context. The exact intracellular concentration of the different EB dependent +TIPs is not known. So far, three CAP-Gly domain containing +TIPs are known (CLIP170, CLIP115 and p150) (Galjart, 2005). In contrast, over 30 SXIP motif containing +TIPs have been described so far (Jiang et al., 2012). This suggest that the overall number of SXIP containing +TIPs is higher as compared to CAP-Gly domain containing +TIPs. This notion makes it indeed possible that p150 can be displaced from growing MT ends due to competition when CLIP170 is absent.

CLIP115 shows a high degree of sequence homology with CLIP170 but lacks the C terminal zinc knuckles that interact with p150 (Galjart, 2005). Knock down of CLIP115

increases both, p150 signals and CLIP170 signals at MT ends (Hoogenraad et al., 2002). This suggests that p150 does not only compete with SXIP motifs for EBs but also with other CAP-Gly domain containing proteins with respect to direct EB binding. In this study, I used a CLIP170ΔC fragment which roughly resembles the role of CLIP115 in the cell. Its CAP-Gly domain can interact with EBs but it cannot provide new binding sites for p150 and can therefore be seen as an additional (in addition to SXIP motifs) competitor for EB1 binding. Consistent with the reported role of CLIP115, CLIP170ΔC (as opposed to CLIP170) was unable to restore p150 end tracking in the presence of EB1 and MACF-$_{SXIP}$ and acted as an additional competitor.

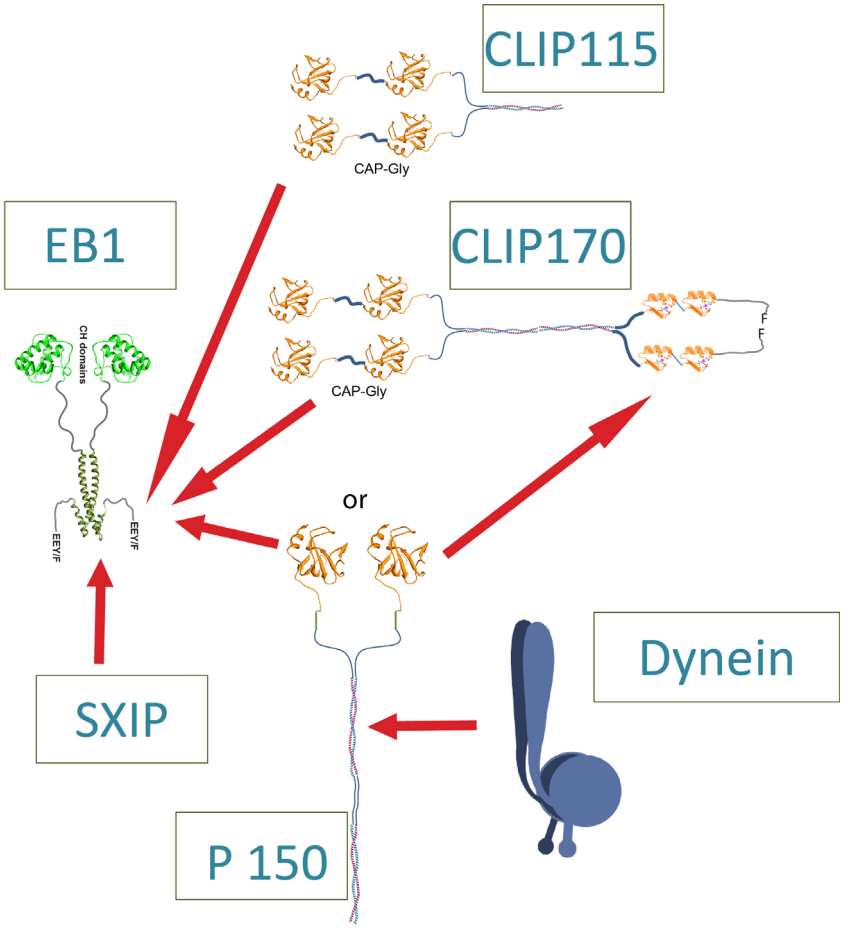

Figure 21: Interactions within the core +TIP network

SXIP motifs, CLIP115, CLIP170 and p150 bind directly to EB1 in a mutually exclusive manner. While CLIP170 can provide new binding sites for p150 at MT ends when it plus end tracks via EB1, CLIP115 and SXIP motifs only compete with p150 for EB binding but do not provide new binding sites. P150 can be targeted to growing MT ends via EBs or CLIP170. A direct

interaction of p150 with the dynein complex (but not the motor domain) supports dynein enrichment at growing MT ends

The simultaneous *in vitro* reconstitution of the major classes of EB dependent +TIP explains the observed phenomena's in cells very well and establishes +TIP competition for EBs as a general theme of the +TIP network.

3.3.2 Different affinities and different binding modes can explain how CLIP170 can overcome competitions by SXIP motif and positively influences p150 end tracking

CLIP170 mediates end tracking of p150 via simultaneous interaction with EBs and p150 in the presence of other competitors. The fact that CLIP170 binding to EBs is more efficient as compared to p150 (**Fig.15&16**) might be attributed to several reasons. Firstly, the overall affinity might be slightly higher – at least this is the case for the fragments used in this study (**Fig.16**). Secondly, the binding mode of CLIP170 and p150 to EB is slightly different. Alanine at position 49 of p150 establishes contacts to the hydrophobic cavity of EBs, in very close proximity to the binding region of the SXIP motifs (Honnappa et al., 2005, Honnappa et al., 2006, Honnappa et al., 2009b). CLIP170 does not have an aliphatic residue at this position (based on sequence alignment, uniprot) which indicates that CLIP170 binding does predominantly depend on the interaction with the flexible tail region of EB (Mishima et al., 2007). This could mean that the competition between p150 and SXIP motifs for EBs is more direct. Both p150 and CLIP170 interact with the flexible tail region of EBs. In the EBc-SXIP complex however, the flexible tail becomes structures and forms part of the binding interface between EBc and the SXIP motife (Honnappa et al., 2009a). This can explain why SXIP motifs also compete with CLIP170 for EBs, but less efficient as compared to p150. Additionally, CLIP170 might interact more efficiently with tubulin at MT ends due to its additional CAP-Gly domains.

CLIP170 can be seen as a more efficient direct EB dependent +TIP as compared to p150 as shown by the presented work. This matches well with data from transfected cells were comets of labelled CLIP170 usually appear to be more intense as compared

to p150 comets at comparable expression levels (Lansbergen et al., 2004, Lee et al., 2010).

3.3.3 CLIP170 provides a new layer of regulation to control the amounts of p150 at MT ends

CLIP170 provides a new layer of regulation in order to precisely control the amount of dynactin/dynein at growing MT ends. CLIP170 switches between an auto inhibited state (in which the c terminus binds to its own n terminus "folded back") and an open conformation (Lansbergen et al., 2004). The autoinhibition can be released by binding to EB1 but not by binding to p150 (Weisbrich et al., 2007).

The degree of autoinhibition in CLIP170 is regulated. Kinases and phosphatases as well as small molecules like neurosteroids can trigger the proportion of activated CLIP170. CLIP170 is a direct substrate of PKA (protein kinase A). Phosphorylation by PKA favours the folded back conformation and results in reduced end accumulation of p150 (Lee et al., 2010). The effects induced by PKA can be –at least *in vitro*- reversed by the neuro steroid Pregnenolon which binds to the coiled coiled region of CLIP170 and reverses the autoinhibition induced by phosphorylation (Weng et al., 2013). Another report identified CK2 (casein kinase) and PLK1 (Polo like kinase 1) as two additional kinases that directly phosphorylate CLIP170, which opposes the effects of PKA. CK2 primes CLIP170 for PLK1 which phosphorylates CLIP170 at position 1311 resulting in increased binding strength between CLIP170 and p150 (Li et al., 2010).

Therefore CLIP170 phosphorylation/dephosphorylation seems to be a main trigger that controls the amount of p150 at MT ends. Alternatively, other EB depend +TIPs such as SXIP motif containing +TIPs as well as CLIP115 are direct targets of kinases – and many of these phosphorylations have been found to modulates their affinity to EB1 (see table in (Duellberg et al., 2013) and (Hoogenraad et al., 2000, Buey et al., 2012))

3.3.4 Plus end tracking of p150 has two main functions in neuronal cells

In neuronal cells, specific loss of p150 at MT ends impairs vesicle transport from the distal tip of neurites. In addition, global knock down of p150 has a destabilizing effect on MT in these cells and increases the catastrophe frequency. Ectopic expression of

wtp150 could rescue this phenotype while the Perry syndrome mutant Q74P failed to do so (Lazarus et al., 2013, Moughamian et al., 2013, Moughamian and Holzbaur, 2012). This suggests that p150 has two major functions in Neurons – a direct stabilization of MTs and an indirect via recruitment of the dynein complex to growing MT ends to initiate retrograde transport from distal ends of neurits. It is not entirely clear to which extent MT stabilization of p150 requires its end accumulation while impaired vesicle transport is clearly linked to a loss of dynactin/dynein at growing MT ends.

Knock down of EBs, CLIP170 and p150 results in impaired retrograde vesicle transport from distal neurite ends suggesting that all of these +TIPs contribute to the loading of dynein motors to MT ends. A comparison of the three knock down conditions (EBs, CLIP170, p150) shows that knock down of CLIP170 has the mildest effect on retrograde vesicle flux form neurite tips (Moughamian et al., 2013). It is shown in the present work that p150 can be loaded onto MT plus ends via EB1 or CLIP170. Knockdown of CLIP170 therefore results in a strong reduction of the number of p150 molecules at MT ends but there should still be a fraction of p150 that is loaded onto MT ends via EBs directly. This can explain why the knock down of EBs and p150 have a more severe effect as compared to CLIP170 knock down but at the same time explains why all of these +TIPs contribute to loading of dynein to MT ends.

3.3.5 The +TIP network has conserved and non-conserved features throughout different tissue types

Apart from p150, LIS1 and NudE are the other main regulator of dynein in vertebrate systems (Kardon and Vale, 2009). Lis1 controls dynein based transport under high load (McKenney et al., 2010) and its knock down causes a general impairment of vesicle transport that is not specific to distal ends of neurites (Moughamian et al., 2013). In agreement with that, no enrichment of LIS1 in distal tips of neurites has been observed as compared to EBs, CLIP170 and p150 which are enriched at least two fold (Moughamian et al., 2013). This suggests that in neurons p150 (and not LIS1) is the main activity that loads dynein to MT plus ends whereas both, LIS1 and p150 contribute to dynein end tracking in cultured non neuronal where both proteins are enriched at growing MT ends (Coquelle et al., 2002, Splinter et al., 2012). The neuronal splice variant of p150 has increased MT lattice affinity (this work and:(Zhapparova et

al., 2009)) but behaves similarly in terms of EB mediated MT plus end tracking. If the increased MT lattice affinity is a special adaptation for long range dynein mediated transport in neurons is possible but a direct comparison between the two isoforms in terms of dynein modulation has not been done yet. Additionally, the higher lattice affinity of the neuronal isoforms results in more efficient stabilization of MTs (Lazarus et al., 2013). Because neurons have long and complex MT arrays, the higher affinity of the neuron specific p150 isoform might be a special adaptation of these cells to generate more stable MTs.

The current work provides new insights into the mechanism of how dynein localisation is controlled. However, the picture is not complete yet and the differences between different tissue types are not fully understood yet. NudE and Lis1 together seem to compete with dynactin for dynein binding as dynactin and NudE have overlapping binding sites (McKenney et al., 2011). In contrast, a recent study in *Drosophila melanogaster* extract showed that Lis1 on its own increases the association of dynactin with dynein during RNA transport (Dix et al., 2013). In agreement with that, analysis in non neuronal cultured cells suggest that Lis1 and dynactin act synergistically to load dynein onto growing MT ends (Splinter et al., 2012). The effect of NudE on dynein end tracking has not been addressed in vertebrate systems but its budding yeast homolog could be implicated in the control of dynein localisation (Li et al., 2005). But it is clear that NudE regulates dynein function in vertebrate systems and potentially also its intracellular localization (Tanenbaum et al., 2008, Wang and Zheng, 2011). Further *in vitro* reconstitutions will be needed to establish clear roles for LIS1 and NudE with respect to dynein localization within the context of different tissues and systems.

+TIPs form a complex network of various activities that control MT organization, MT dynamics, mediate transport along MTs and link them to other cellular structures (Duellberg et al., 2013). In this chapter a central part of this +TIP network has been reconstituted *in vitro* using purified components. It has been demonstrated how different +TIPs act as a system and how they influence each other. More specifically, new molecular details regarding EB and CLIP170 dependent p150/dynein end tracking have been revealed which are also medically relevant as impaired plus end tracking of P150 is associated with severe genetic disorders (Stockmann et al., 2013, Farrer et al., 2009). However further studies will be needed to completely understand how the +TIP network

functions and how different dynein regulators coordinate the various functions of cytoplasmic dynein in different cell types.

Chapter 4. A Designed Ankyrin Repeat Protein Selected to Bind to Tubulin Caps the Microtubule Plus End

Note: This chapter is a summary of a project that was performed as collaboration with the laboratory of Marcel Knossow (CNRS, Gif sur Yvette, France) and Andreas Plückthun (University of Zurich, Switzerland). Except for Figure 21 all data presented were produced by me. External contribution are acknowledged and specified in the figure legend. This project has been published and is listed as reference (Pecqueur et al., 2012).

4.1 Introduction

An important question for understanding microtubule dynamics is the nature of structural transitions that take place when soluble tubulin dimers are incorporated into a microtubule. GDP tubulin is thought to be curved in solution whereas GDP tubulin in the older part of the MT lattice is rather straight (Ravelli et al., 2004). It is not known at which stage straightening of the tubulin dimer occurs. Studies based on the GTP analogue GMPCPP suggested that GTP would pre-straighten the tubulin dimer or somehow affect its bending flexibility prior incorporation into the MT (Muller-Reichert et al., 1998, Wang and Nogales, 2005, Howard and Hyman, 2009)). However, more recent studies did not find any evidence for a pre-straightening of tubulin in the presence of GTP as compared to GDP (Barbier et al., 2010, Rice et al., 2008, Nawrotek et al., 2011).

To address the question when tubulin straightening occurs, Designed ankyrin repeat protein (DARPin) technology (Binz et al., 2003) was applied to shed new light on the structure of tubulin itself and to further dissect the sequence of events that take place while MTs grow. The presented data do not support the idea of a pre-straightening of tubulin but in turn provide strong evidence that tubulin in solution and even at MT ends is still in its curved solution structure. This suggest that large conformational changes that lead to tubulin straightening occur at much later time points during tubulin incorporation into a MT than previously appreciated.

4.1.1 DARPins

DARPin are genetically engendered antibody mimetic tools that have been proven to be powerful molecules in basic research, diagnostics and are promising tools as therapeutic agents. DARPins are selected to bind a specific target protein with high specificity and affinity and have been used as crystallization aids for "hard to crystalize proteins" (Bukowska and Grutter, 2013, Boersma and Pluckthun, 2011).

DARPins are derived from the natural occurring protein Ankyrin that mediates high affinity protein-protein interaction between spectrin and at least 12 different membrane protein families. Ankryrins are composed of repetitive structural units of 33 amino acids that are connected by flexible linker sequences. Each structural unit consists of 6 variable amino acids that mediate specific protein interaction while the remaining 27 amino acids form the structural backbone of each unit. A DARPin is a sequence of typically 5 structural units and each variable amino acid in each structural unit can be different, leading to a high diversity within a DARPin library. From these libraries high affinity binders are selected in screens that can then be further optimized using additional protein engineering approaches (Boersma and Pluckthun, 2011).

In this section, the first anti tubulin DARPin is described and its usefulness for studying cytoskeleton dynamics is demonstrated. This novel DARPin yielded new insight into the structure and conformational changes of tubulin, MT dynamics in general and it is further shown that this DARPin can be used as a tool to specifically perturb MT plus end dynamics *in vivo* and *in vitro*.

4.2 Results

4.2.1 Structural insights from a DARPin tubulin complex: GTP tubulin is curved in solution

A DARPin library for tubulin binders has been screened by L. Pecqueur with the help of other authors as listed in (Pecqueur et al., 2012) and a strong binder has been found, called D1. L. Pecqueur solved the crystal structure of the D1:tubulin complex with tubulin bound to GTP (**Fig.22a**) and he further showed that D1 binds with very similar affinity to GTP-tubulin and GDP-tubulin in solution (**Fig.22d**).

The overview of the complex (**Fig22a**) clearly shows that D1 binds to tubulin at the longitudinal interface of β tubulin only i.e. the part of tubulin that would normally be exposed at the MT plus end. Superposition of the D1:GTP-tubulin complex with T2R (tubulin in complex with RB3-stathmin like domain, see introduction 1.2.2) in its GDP state shows that the overall structure of tubulin is virtually identical; both exhibiting a curved conformation (**Fig22b**). D1 and RB3-SLD binding interfaces do not overlap and the D1 interface is more than 40 Å away from the tubulin dimer interface between α-tubulin and β-tubulin; therefore it is unlikely that both co-crystallisation proteins force the tubulin dimer into the same overall curved conformation. This suggests that the previously reported tubulin structure in T2R resembles the natural and curved tubulin solution structure and that the curvature is independent of GTP or GDP binding. D1 contacts β tubulin along three structural elements which are helices H11 and H6 as well as loop T5 (**Fig.22c**). Helix 6 rotates upon going from the curved tubulin conformation to the straight protofilament conformation (**Fig.22e**) (Ravelli et al., 2004). Thus the D1 binding interface is expected to be present in soluble curved tubulin only but not in straight microtubular tubulin.

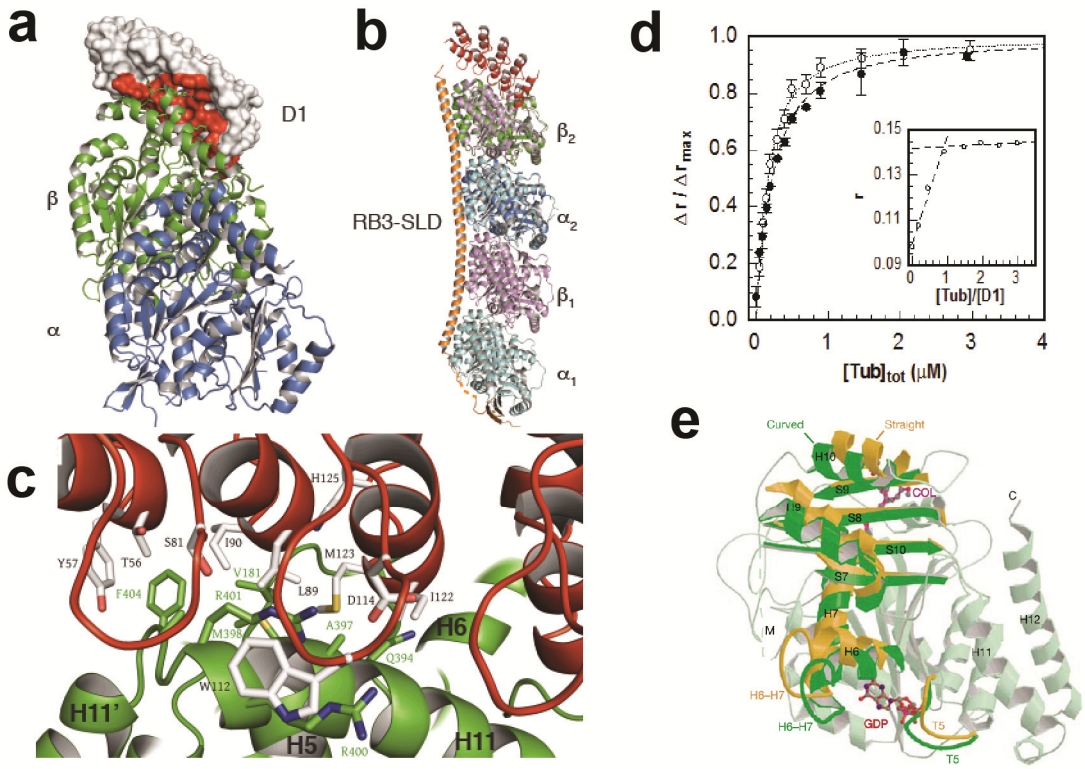

Figure 22: Crystal structure of D1:tubulin

(a) Overall crystal structure of the D1-tubulin complex with tubulin bound to GTP. The red surface corresponds to the D1 interacting surfaces. **(b)** Superposition of D1-tubulin complex with T2R in its GDP bound state (pdb 3RYI). In D1-tubulin, D1 is presented in red and tubulin in dark blue (α tubulin) and green (β tubulin). In T2R α tubulin is presented in cyan and β tubulin in pink and RB3-SLD is orange. **(c)** Close up of the D1 tubulin binding interface with D1 in red and tubulin in green. D1 side chains shown in **(c)** are randomized in the library D1 was selected from. **(d)** D1 binds with similar affinity to GDP and GTP tubulin as accessed by fluorescence anisotropy measurements. Variation of fluorescence anisotropy of labelled D1 (120 nM) upon binding to GDP-tubulin (open circles) or GTP tubulin (solid cicles). Inset: Titration of 1 μM labelled D1 by GDP-tubulin under conditions where the D1 concentration was larger than the kd. Here a maximum was reached for a 1:1 tubulin:d1 ratio, as expected for a 1:1 stoichiometry of the complex. Extracted kd values were: 155 nM (±10 nM) for GTP-tubulin and 120 (±10 nM) for GDP tubulin **(e)** Superposition of tubulin in T2R (green, curved) and in protofilaments (orange, straight) with the M-loop in dashed lines. Fig.a-d was taken from (Pecqueur et al., 2012) and (e) from (Ravelli et al., 2004).

4.2.2 D1 and (D1)2 blocks MT growth specifically at MT plus ends indicative of a curved tubulin conformations at MT plus ends

I first tested if the assumption is valid that D1 does not bind to straightened microtubular tubulin. For that Alexa488 labelled D1 and an Alexa488 labelled tandem repeat of D1 called (D1)2 with increased affinity to tubulin was used. As predicted from the crystal structures, no association with either the lattice nor any of the two ends of

stabilized GMPCPP microtubules in the absence of free tubulin was observed under my assay conditions over a concentration range from 0.75 nM to 100 nM for Alexa488-(D1)2 (**Fig.23a**) or Alexa488-D1 (nor shown).

I next investigated whether and how D1 affects MT dynamics. Because D1 binds to the longitudinal interface of β-tubulin it is expected that D1 acts as a sequestering protein at minus ends. Tubulin dimers bound to D1 are not expected to add to the minus end while D1-free tubulin dimers could add in a normal manner to the minus end (scheme in **Fig.25**).

For MT plus ends 2 scenarios are possible:

If terminal tubulin dimers at MT ends are straight D1 would not bind to MT ends because helix 6 has already rotated away and we would not expect a strong effect of D1 on MT plus end dynamics at low concentrations. In this case, an indirect sequestering based effect would be expected, which would be detected only at high D1 concentrations.

If terminal tubulin subunits at a MT plus end are still in the curved solution state, D1 is expected to add to these ends (from solution or tubulin bound). In turn this association would prevent the addition of the next tubulin subunit onto the plus end because the end would be blocked for the next arriving tubulin by D1 (See scheme in **Fig.25** for illustration).

Using the TIRF based dynamic instability assay (see above and (Telley et al., 2011)), I tested the effect of D1 and the tandem repeat (D1)2 on MT growth. While control MT had one fast growing end and one slow growing end (**Fig.23b**), 250 nM (= 1:80 ratio to tubulin) D1 slowed down MT growth specifically at the plus end and the two ends were not distinguishable anymore. 250 nM (D1)2 blocked growths on the plus end completely while minus ends were not affected (**Fig.23b**).

To confirm unambiguously that growth was blocked specifically on the plus end, I performed kinesin based gliding assays. Kinesin 14 is a minus end directed motor and transports MTs when adsorbed to glass (Hentrich and Surrey, 2010, Vale et al., 1992). Using this assay in the presence of free tubulin and Mal3-GFP (which accumulates at growing MT ends and is thus a marker for growing ends, (Bieling et al., 2007) confirmed that (D1)2 specifically blocked growth at the plus ends: Under control

conditions, MT had both ends labelled with Mal3-GFP (**Fig.23c, upper**) while MT in the presence of (D1)2 had only the lagging end (= minus end) labelled with Mal3-GFP (**Fig.23c, lower**), which confirms that plus end growth is selectively blocked by (D1)2.

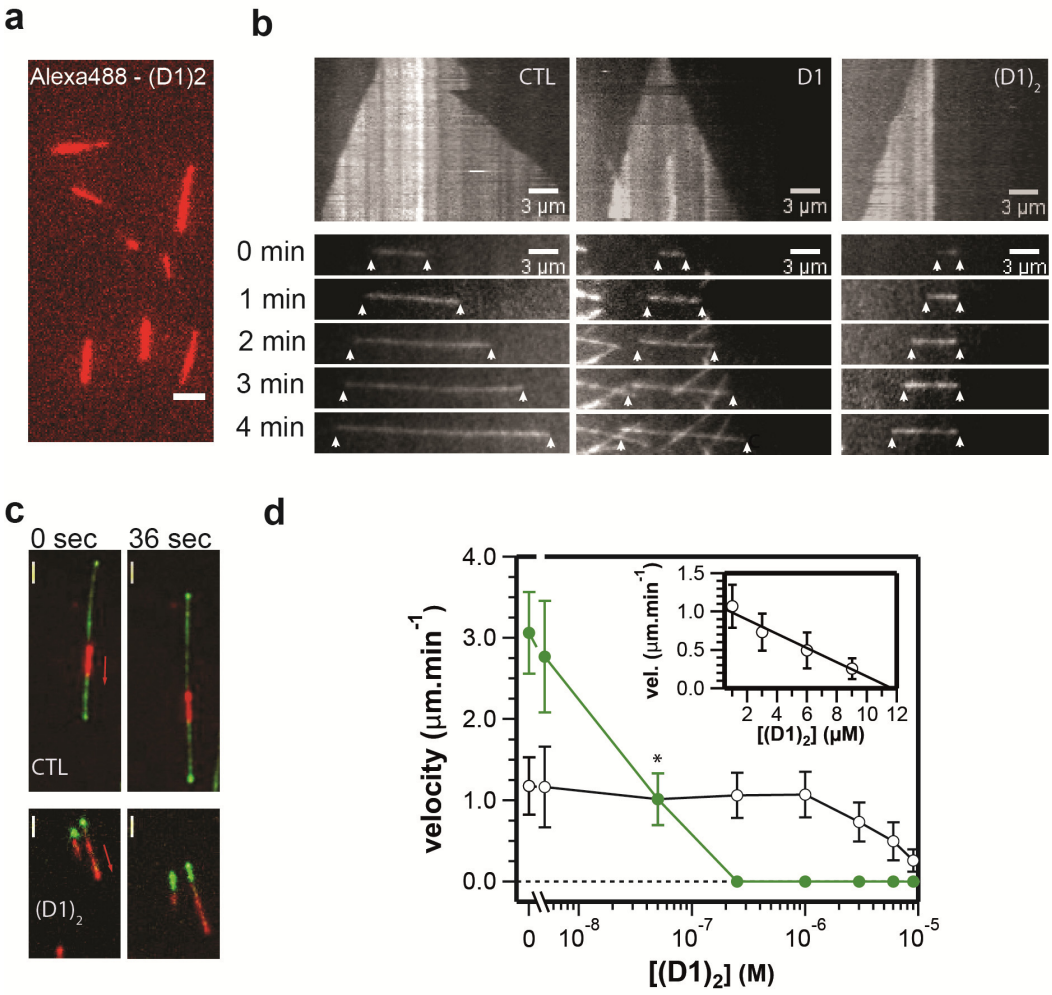

Figure 23: (D1)2 blocks growth specifically at MT plus ends

(**a**) TIRF microcopy images of Alexa488-(D1)2 (90 nM, green) and Alexa568 labelled stabilized GMPCPP MT (red) in the absence of free tubulin. No binding was observed over a concentration range from 0.75 nM to 100nM. Scale:3 µm (**b**) Kymographs of Alexa568 labelled microtubules growing from surface immobilized GMPCPP MT seeds in the absence (left) or presence of 250 nM D1 (middle) or (D1)2 (right) and a time series below. Tubulin concentration was 20 µM (6.5% labelled with Alexa 568). Total duration displayed is 5 minutes. (**c**) TIRF microscopy imaged at two different time points of dynamic MTs being transported by surface immobilized XCTK2 motors (Kinesin 14, a minus end directed motor). MT polymerize from Alexa568 labelled GMPCPP seeds (red) in the presence of 20 µM unlabelled tubulin and 70 nM Mal3-GFP (green) as a growth indicator.(**d**) Growth velocity of MT ends (plus end: green, minus end: black) at 20 µM as a function of increasing (D1)2 concentration. The data point marked with "*" is an average of both plus end and minus end growth velocity because the ends could not be distinguished. Error bars are SD from an average of at least 20 MTs from three independent experiments. Inset: Minus end growth velocity as a function of (D1)2 on a linear scale.

I next measured the growth velocity of MT plus ends and minus ends as a function of (D1)2 concentration. Plus end growth slowed down at very low concentration and stopped completely at 250 nM (**Fig.23d**). Growth of the minus end was affected only at much higher concentration. The growth velocity at the minus end slowed down linearly with (D1)2 concentration (see insert **Fig.23d**) and stopped at a ratio slightly smaller than one (D1)2 per two tubulin dimers as indicated by a linear fit. Thus, for the minus end (D1)2 behaves as one would expect it for a pure sequestering protein that can bind up to two tubulin dimers. D1 had a similar but much weaker effect but did not completely stop growth on the plus end (**Fig.24**) probably due to its lower affinity/shorter dwell time.

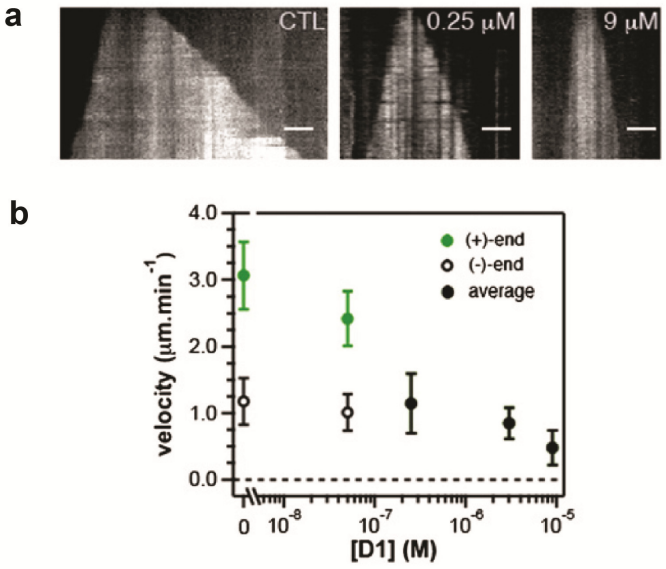

Figure 24: MT growth inhibition by D1

(a) Representative kymographs of growing MT ends in the absence or presence of 0.25µM and 9µM D1 at 20 µM tubulin. Total duration is 279 seconds, scale bar: 3 µm. **(b)** growth velocity of MT ends at 20 µM tubulin as a function of D1 concentration. At concentrations higher than 0.25 µM plus and minus ends could not be distinguished and averages are presented as indicated.

Taken together, this demonstrates that (D1)2 acts as a pure sequestering protein for the minus end and that it "caps" specifically the plus end, preventing further growth on that end (**Fig.24**). (D1)2 binds tubulin in its solution like state but not in its straight protofilament-embedded conformation. (D1)2 adds to MT plus ends in the presence of free tubulin only, which suggests that terminal tubulin subunits at MT ends are curved and that straightening takes place at a later stages of tubulin dimer incorporation.

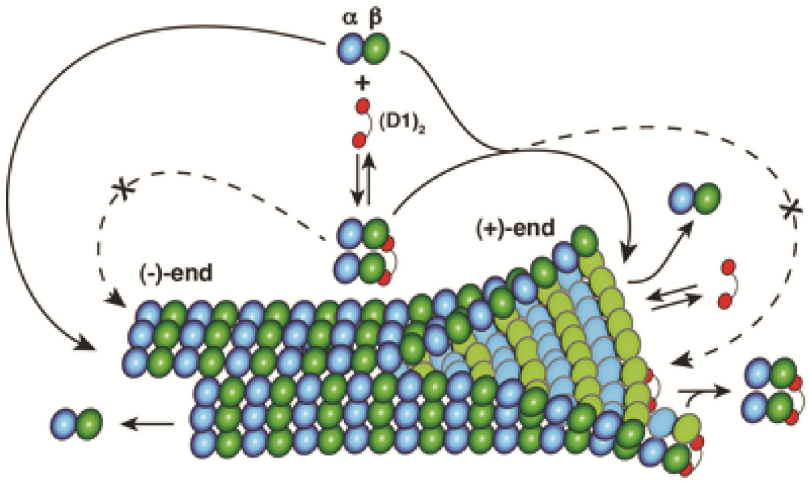

Figure 25: The mechanism of how (D1)2 affects MT dynamics

(D1)2 (red) prevents tubulin addition (α blue, β green) to the minus end. (D1)2 associates with the plus end and blocks the addition of all tubulin dimers to the capped end. From (Pecqueur et al., 2012)

4.2.3 Capping by (D2)2 favours catastrophes

Capping proteins are well described for actin (Cooper and Sept, 2008) but little is known about capping proteins for microtubules. Capping proteins dampen dynamics at filament ends thus favouring a pause like state. Such roles have been described for XKLP1/KIF4a (Bringmann et al., 2004, Bieling et al., 2010b) and Kif18a (Du et al., 2010) but the mechanism of how they fulfil these roles are not understood.

(D1)2 adds to MT plus ends and it can bind two tubulin dimers simultaneously. Due to the long and flexible linker, it is expected that (D1)2 can bind simultaneously to two tubulin subunits at MT ends from adjacent protofilaments. Because (D1)2 blocks further growth at that end and can probably link to protofilaments, it can be seen as a very simple model capping protein. To study the effect of such a simple model capping protein, I tested the effect of (D1)2 on preformed MT plus ends.

I prepolymerized microtubules in the presence of cy5 labelled tubulin from Alexa568 labelled GMPCPP seeds. Next, the solution was exchanged by unlabelled tubulin, GFP-$CLIP_{MTB}$ (a GFP tagged fragment of CLIP170 that binds MT to visualize the entire MT) and (D1)2 or its storage buffer for the control condition. Time lapse movies were started ~ 30 seconds after solution exchange. Kymographs of GFP-$CLIP_{MTB}$ labelled MTs showed that capped plus ends indeed remained in a pause like state (**Fig.26 a&b**) but

ultimately underwent catastrophes. Plus ends did not regrow after they had a catastrophe and minus ends showed normal dynamic instability behaviour (**Fig.26a**).

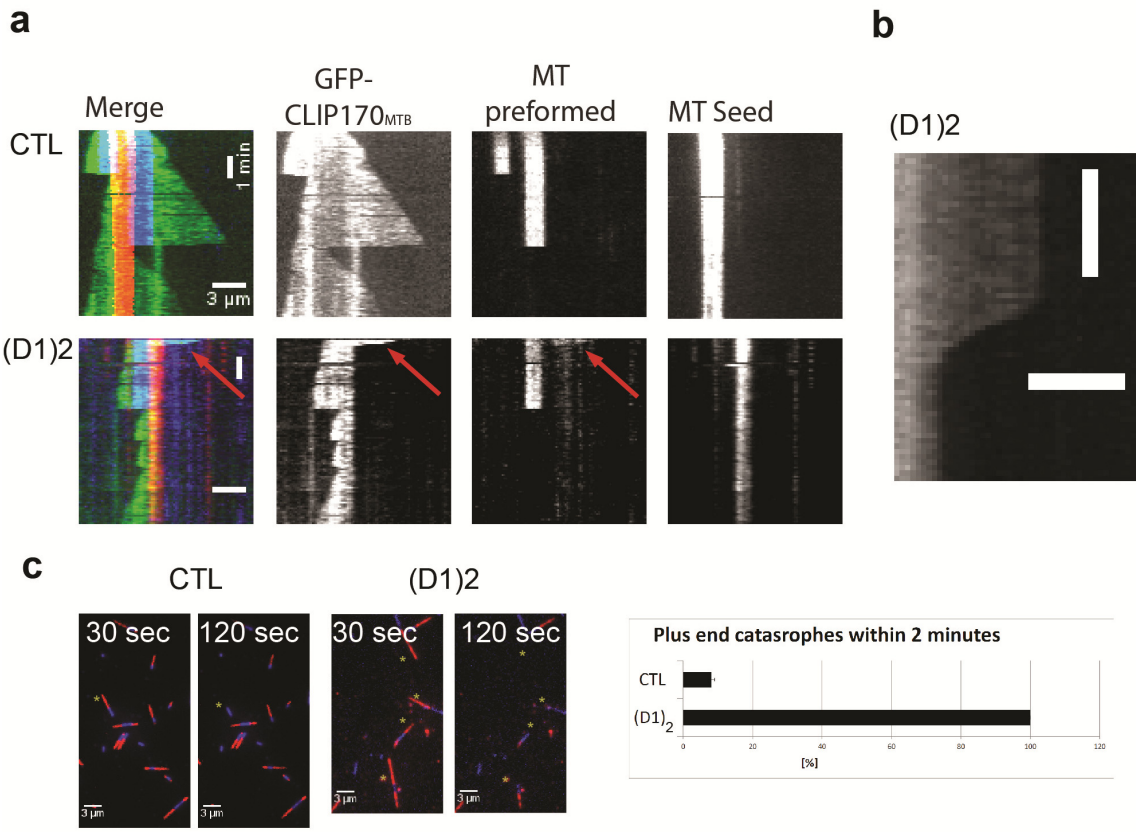

Figure 26: MT end capping by (D1)2 favours catastrophe

(a) Kymographs show the effect of 500 nM (D1)2 on MTs prepolymerized in the presence of 15 µM Cy5-labeled tubulin (blue) from immobilized Alexa568 labelled stabilized seeds (red). Images started ~30 sec after replacing labelled with unlabelled tubulin and the addition of 65 nM GFP-$CLIP_{MTB}$ (green) and (D1)2 (lower) or its storage buffer (upper, CTL). Merged kymographs (left) and the individual channels as indicated are presented. Total time: 500 sec. **(b)** $CLIP_{MTB}$ channel as in **(a)** with higher time resolution to demonstrate the pause state prior catastrophe. Scale: 3 µm (space) and 20 seconds (time). **(c)** Prepolymerized Cy5 labeled plus end segments (red) were grown from stabilized seeds (blue) and were counted ~ 30 seconds after solution exchange and 90 seconds later. Plus ends undergoing catastrophes are marked with an asterisk. The identity of each end was extracted via their growth speed from kymographs (see material and methods for details). For the quantification 50 plus ends from three independent experiments were analysed.

To further analyse the stability of capped plus ends, preformed cy5 labelled segments where quantified at different time points. While ~ 10 % of control MT had one catastrophe within 90 seconds of image acquisition, all (D1)2 capped ends had disappeared after the same time period (**Fig.26c**). Taken together this shows that simple capping of a MT plus ends by (D1)2 favours depolymerisation after forcing the MT end into a pause like state. Thus the mechanism by which XKLP1/Kif4 caps MT plus ends

is probably more complex than simply connecting two protofilaments at MT ends because MT ends capped by XKLP1 remain stable for much longer time periods without pronounced net growth or net shortening (Bieling et al., 2010b) .

I next tested if (D1)2 can also be used to specifically perturb plus ends dynamics *in vivo*. For that I used *Xenopus laevis* egg extract, a well-established *ex vivo* system where MT dynamics can be studied under close to *in vivo* conditions. These extracts contain all proteins of the cytoplasm of the frog egg at essentially native concentrations (Hannak and Heald, 2006).

Egg extracts were supplemented with Alexa 568 tubulin for visualization and sperm nuclei to induce aster formation (Hannak and Heald, 2006). Asters were adsorbed to non functionalized glass coverslips and observed by TIRF microscopy. Then, GFP (control) or Alexa488-(D1)2 was added to a calculated concentration of 750 nM and the diffusion into the field of view was monitored using the fluorescence in the 488 channel (**Fig.27b**)

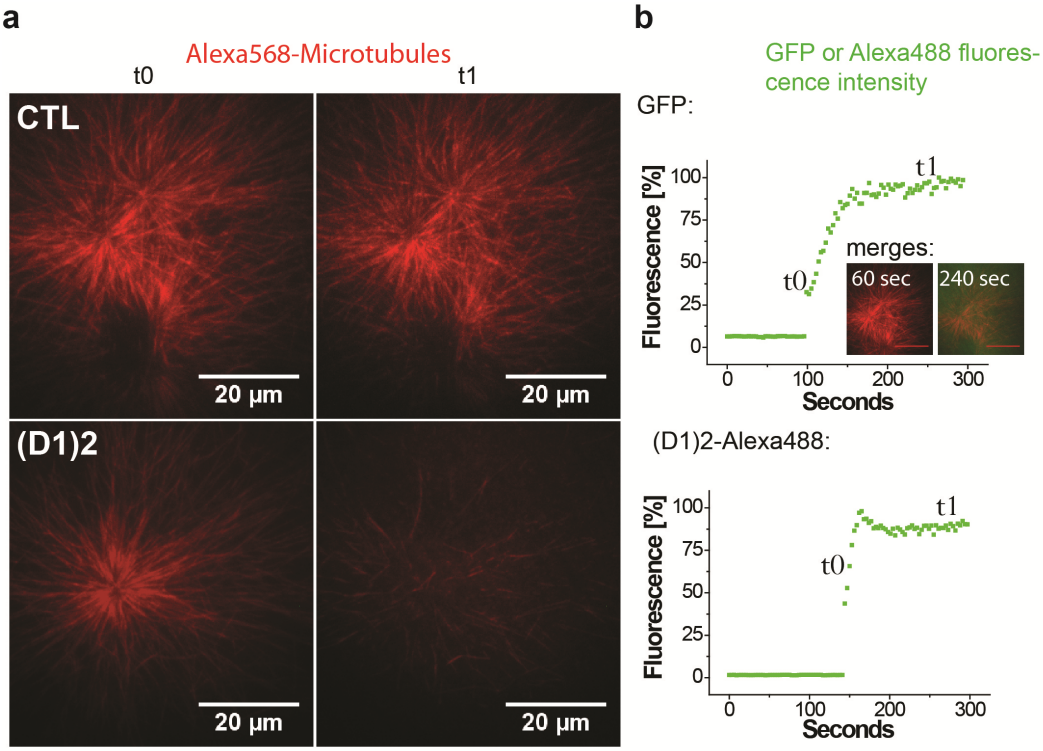

Figure 27: (D1)2 promote MT depolymerisation in Xenopus egg extract

(a) Asters supplemented with Alexa568 tubulin were adsorbed to glass cover slips and imaged by TIRF microscopy (t0). **(b)** After addition of GFP or Alexa488 (D1)2 to an estimated concentration of 0.75 µM, the diffusion into the field of view was monitored using the fluorescence in the 488 channel. Asters that are still present when the newly added protein starts to diffuse into the field of view (t0 in **(a)** and **(b)**) have largely disappeared 150 sec later (t1)

selectively when Alexa488-(D1)2 is added (t1 and (a) and (b)). Inserted images in (**b**) show merged imaged to visualize how GFP (green) diffuses into the evanescent field where asters (red) are imaged.

While Asters supplemented with GFP were unaffected, addition of (D1)2 caused a large reduction of MT density and eventually did lead to complete collapse of these asters (**Fig.27a** at t1). This demonstrates that (D1)2 also caps MT plus ends in the presence of other MAPs under physiological condition. (D1)2 can therefore be used to specifically perturb MT plus end dynamics in *ex vivo* systems and potentially in cell cultures or even in whole animals (microinjection or induced overexpression).

4.3 Discussion

This is the first characterisation of an anti tubulin DARPin and its application as a tool to study cytoskeleton dynamics. Three main conclusions can already be drawn from the current work, which underline the value of DARPins as new tools in the field of cytoskeleton dynamics research.

Before this study, T2R was the only described co crystal structure of the tubulin dimer in complex with a stathmin like domain (Gigant et al., 2000, Nawrotek et al., 2011). The curvature of both GTP-tubulin and GDP-tubulin in these complexes was ~12 C.

A major function of Stathmin in the cell is to regulate the amount of polymerizable tubulin. It does so by sequestering two tubulin dimers per Stathmin which then cannot be incorporated into microtubules. Phosphorylations modulate stathmin affinity for free tubulin, which allows precise spatiotemporal regulation of the polymerizable tubulin pool (Belletti and Baldassarre, 2011, Belmont and Mitchison, 1996).

Therefore it was not clear if Stathmin forces tubulin into a curved conformation to prevent polymerisation or if the observed curvatures resembled the native conformations of tubulin. The binding interface of D1 along tubulin is completely different from RB3-SLD and 40 Å away from the interdimer interface between α and β tubulin. It is therefore unlikely that D1 induces an overall curvature of GTP-tubulin into the same conformation as RB3-SLD does. Thus the new crystal structure of D1-tubulin provides a strong argument for the notion that both GTP- and GDP-tubulin have an overall curved solution structure. But how does GTP trigger the polymerization potency

of tubulin? A recent study reported a T2R crystal structure of tubulin for GTP- and GDP-tubulin at 2.1 Å and 2.5 Å respectively (Nawrotek et al., 2011), resolving their differences in much more detail than previous reports (Gigant et al., 2000). While the overall structures look very similar, detailed differences that are potentially highly significant could be observed. The γ phosphate of GTP interacts with the T3 loop while a watermolecule interacts with the β phosphate in GDP tubulin. This nucleotide change results in the displacement of Asn β101 which directly interacts with the γ phosphate in GTP-tubulin via hydrogen bonds. The resulting displacement of T3 induces a flip of T5 which disrupts two intermolecular hydrogen bonds within the β tubulin subunit, generating two new available residues to form lateral (Thr β180) and longitudinal contacts (β101) to neighbouring tubulin subunits. A second consequence is an increase in the exposure of negative charges at the longitudinal interface of β tubulin, potentially important for electrostatic interaction with α tubulin (Nawrotek et al., 2011).

It has been proposed earlier that the T5 loop and H6-H7 form a kinetic barrier between the straight and the curved conformation, favouring the curved conformation in solution (Ravelli et al., 2004).

Our results further support a model in which tubulin in solution is curved and provides evidence for the first time that tubulin at MT ends is in a curved solution state. Both, GDP- and GTP tubulin could add to MT ends via longitudinal electrostatic interaction in their curved conformation. The formation of lateral and longitudinal contacts would then force the tubulin into the straight conformation, overcoming the energy barrier mentioned above. Because GTP-tubulin has more available residues to interact with neighbouring tubulin subunits, this straightening is more likely to occur for GTP tubulin as compared to GDP tubulin.
However, it should be noted that the DARPin probe is sensitive only to the initial contact formation of new tubulin subunits that add to the microtubule plus end. It cannot be ruled out that straightening occurs directly at the microtubule end directly after initial contacts have been made but before new tubulin subunits add onto this end, because DARPins itself might prevent straightening.

It has been reported that GDP tubulin can also be incorporated into exisitng MTs when GTP and GDP tubulin were mixed (Valiron et al., 2010). If a complete pre-straightening would be required for tubulin incorporation into a MT, this finding would be very hard to imagine. If both GDP and GTP could add onto MT ends in a curved manner it is possible that the energy barrier can occasionally be overcome leading to GDP tubulin incorporation into a MT.

Tubulin incorporation stimulates its intrinsic GTPase activity. After GTP hydrolysis and Pi release, the hydrogen bond between Asn β101 and γ phosphate is lost which could lead to a rearrangement that effectively weakens lateral and/or longitudinal contacts favouring again a curved conformation of the tubulin dimer. If the MT is not protected by a stabilising end structure with stronger inter subunit contacts, tubulin subunits would tend to "flip back" to their original conformation ultimately leading to MT depolymerisation. This is supported by EM studies who observed outward curved oligomeric structures at depolymerising MT ends (Muller-Reichert et al., 1998). These oligomers appear to be connected via longitudinal interactions but not by lateral interaction, suggesting that lateral interaction break before longitudinal interactions are lost.

Finally it was show that simple capping of a MT ends induces a pause like state which ultimately leads to a catastrophe *in vitro* and in X*enopus laevis* egg extract. These pauses are considerably longer as compared to pause states until catastrophe induced by complete tubulin removal (Chapter 2 of this thesis) but short compared to the anaphase situation for Xklp1/Kif4a (Bieling et al., 2010b, Hu et al., 2011). This is a good starting point in order to understand how natural capping proteins like Kif18a and XKLP1/kif4 act and suggests that their mode of action is probably more complex. Further studies will be needed to understand how these classes of proteins affect MT dynamics.

Chapter 5. Material & Methods

5.1 Chemicals & Kits

Description	Company	Cat number	Remarks
(3-Glycidyloxypropyl)trimethoxysilane	Sigma	440167-100ml	
2-(N-Morpholino)ethanesulfonic acid hydrate (MES)	Sigma	M8250-100G	
2,2-Bis(hydroxymethyl)-2,2′,2″-nitrilotriethanol („Bis Tris“)	Sigma	B9754-25G	
2-Mercaptoethanol	Sigma	63689	
2-Propanol	Fischer	P7500PC17	
4-(2-hydroxyethyl)-1-piperazineethanesulfonic acid (Hepes)	Sigma	H3375	
Acetic acid	Fischer	10060000	glacial
Acetone	Fischer	A0600PC17	
Acrylamide/Bisacrylamide mix	Fischer	BP1410-1	Ratio:37.5:1
Adenosine-triphosphate (ATP)	Sigma	A29209-5G	
Agarose	Sigma	A9539-500g	
Ammonium persulfate (APS)	Sigma	A3678-25G	
Apmicilin	Fischer	10193433	
Arginin	Sigma	A8094-1kg	
Brij 35	Thermo/Pierce	28316	10 % solution
Calcium chloride ($CaCl_2$)	Sigma	C5670-100G	
Chloramphenicol	Fischer	BP904-100	
Comassie brilliant blue	Serva	42660	
D-Glucose	Fischer	G/050053	
Dimethyl sulfoxide (DMSO)	Sigma	D8418-50ML	
Dipotassium phosphate (K_2HPO_4)	Sigma	P3786-100G	
Disodium hydrogen phosphate (Na_2HPO_4)	Fischer	S452053	
Dithiothreitol (DTT)	Fischer	10666885	
Ethanol	Sigma	32221-2.5l	
Ethidium bromide	Fischer	BP1302	

Ethylene glycol-bis(2-aminoethylether)-N,N,N′,N′-tetraacetic acid (EGTA)	Sigma	E3889-100g	
Ethylenediaminetetraacetic acid (EDTA)	Sigma	EDS-500g	
Gentamycin	Sigma	G1397-10ML	
Glutamic acid	Sigma	49449-500g	
Glycerol	Fischer	G0650/17	
Glycine	Sigma	G7126-1kg	
GTP gamma S	Roche	11110349001	
Guanosine-5'-[(α,β)-methyleno]triphosphate (GMPCPP)	Jena Bioscience	NU-405S	Sodium salt
Guanosine-5'-triphosphate (GTP)	Fermentas	R0461	
Hydrochloric acid (HCl)	Fischer	10244100	
Hydrogen peroxide (H_2O_2)	Agros	CHE/HYD/3L	Non stabilized
Imidazol	Fischer	10518050	
Isopropyl β-D-1-thiogalactopyranoside (IPTG)	Roche	11411446001	
Kanamycin	Fischer	BP906-5	
Magnesium Chloride ($MgCl_2$)	Sigma	M1028	
Magnesium sulphate ($MgSO_4$)	Sigma	203726-25G	
Methanol	Sigma	322415-1L	
Methylcellulose	Sigma	M0512-100g	4000 cp
Monopotassium phosphate (KH_2PO_4)	Fischer	BP329500	
Monosodium phosphate (NaH_2PO_4)	Fischer	P480053	
NH2-PEG_{3000}-Biotin	Rapp	13 3000-25-20	
NH2-PEG_{3000}-OH	Rapp	10 3000-20	
NHS-Alexa 568 (succinimidyl esters)	Life technolohies	A-20003	
NHS-Alexa 647 (succinimidyl esters)	Life techbnologies	A-20006	
NHS-Biotin (succinimidyl esters)	Thermo Fischer	20217	
NHS-Cy5 (succinimidyl esters)	Lumiprobe	23020	
Nickel II chloride	Sigma	33935	
Nocodazol	Sigma	M1404-2MG	

Paclitaxel/ Taxol	Sigma	T7191-25MG	
Piperazine-N,N′-bis(2-ethanesulfonic acid) (PIPES)	Sigma	P6757-1kg	
Pluronic F127	Sigma	P2443	
Polydimethylsiloxane (PDMS)	Sylgard	24001673921	
Potassium Acetate	Fischer	P376053	
Potassium chloride (KCl)	Fischer	P428053	
Potassium hydroxide (KOH)	Fischer	P564053	
Protease inhibitors (Complete®)	Roche	05 056 489 001	
Proteino Ni-TED	MACHEREY-NAGEL	745200.30	
Roti Block for Western Blots	Carl Roth	A151.1	
Sodium chloride (NaCl)	Fischer	S316065	
Sodium dodecyl sulphate (SDS)	Fischer	SP53053	
Sodium hydroxide (NaOH)	Fischer	S492053	
Sucrose	Sigma	84097-1kg	
Sulfonic acid (H_2SO_4)	Sigma	320501-1L	
Tetracyclin	Sigma	T7660-5G	
Tetramethylethylenediamine (TEMED)	Sigma	T9281	
Toluole/ Toluene	Fischer	10356390	
Tridecafluoro-1,1,2,2,-tetrahydrooctyl-1-trichlorosilane	Sigma	370517-25G	
tris(hydroxymethyl)aminomethane (TRIS)	Fischer	BP152-1	
Trypan Blue	Life technologies	15250-061	
Tween 20	Fischer	BP337-500	
Water (H_20)	Milli Q	N.A.	18.2 MΩ
Zinc chloride ($ZnCl_2$)	Sigma	96486-50g	

Table 1: Chemicals

Description	Company	Cat number	Remarks
Acc65I	New England Biolabs	R0599S	
Antarctic Phosphatase	New England Biolabs	M0289S	
ApaI	New England Biolabs	R0114S	
BSA	Sigma	A4503-100g	
Catalase	Sigma	C40-100MG	
CLIP170 antibody	Sigma	PRS4659-100UG	Rabbit polyclonal
DNase I	Roche	10104159001	
DpnI	New England Biolabs	R0176L	
EcoRI	New England Biolabs	R0101S	
GFP antibody	Abcam	Ab290	Rabbit polyclonal
Glucose oxidase	Serva	22778.01	
HRP-anti mouse secondary antibody	Santa Cruz Biotechnology	Sc-2005	Goat polyclonal
HRP-anti rabbit secondary antibody	Santa Cruz Biotechnology	Sc-2004	Goat polyclonal
Kappa HiFi DNA Polymerase	Kappa Systems (Anachem)	KK 2101	
NcoI-HF®	New England Biolabs	R3193S	
Neutravidin	Life technologies	A-2666	
NotI	New England Biolabs	R0189S	
Penta-His antibody	Qiagen	34660	Mouse monoclonal
T4 Ligase	New England Biolabs	M0202S	
XbaI	New England Biolabs	R0145S	
XhoI	New England Biolabs	R0146S	
β-Casein	Sigma	C6905-250MG	
κ-Casein	Sigma	C0406-100MG	

Table 2: Commercial proteins, enzymes and antibodies

Description	Company	Cat number
QIAquick Gel Extraction Kit	Qiagen	28704
QIAprep Spin Miniprep Kit	Qiagen	27104
NucleoBond® Xtra Midi prep kit	Macherey-Nagel	740410.10
Amersham ECL Advance – Western Blotting detection Kit	GE Healthcare	RPN2135
FuGENE® HD Transfection Reagent	Promega	E2311
Bradford protein detection kit	Biorad	500-0205

Table 3: Kits

5.2 Molecular Biology

Cloning was performed using standard methods. DNA inserts were amplified from cDNA clones or exsiting expression plasmids using Kappa HiFi polymerase (KapaBiosystems; KK 2101) according to the manufactures recommendation. All primers were purchased from Sigma Aldrich (desalt grade) and annealing temperatures were calculated using APE freeware (http://biologylabs.utah.edu/jorgensen/wayned/ape/). Complete PCR reactions were loaded on agarose gels and PCR products were purified using QIAquick Gel Extraction Kit (28704). PCR products and vectors were digested for 1 hour using standard restriction enzymes (all for New England Biolab, NEB, see table 2) and vectors were subsequently treated with Antarctic Phosphatase (NEB, M0289S) for another hour at 37 ˚C. After heat inactivation at 75 ˚C for 20 minutes, the DNA was purified using the QIAquick Gel Extraction Kit. DNA concentrations were measured using a nanodrop spectrophotometer. Inserts and vectors were mixed in a 3:1 molar ratio and incubated with 10 U/µl T4 Ligase (NEB, M0202S) for one hour at room temperature in ligation buffer with ATP (NEB). Then 50 µl of XL1 Blue *Escherichia coli* cells (Stratagene)

were transformed with 5 µl of ligation mix using standard heat shock procedures (Froger and Hall, 2007) and Ampicilin (100 µg/µl, Fischer) or Kanamycin (30 µg/µl, Fischer) as a selection marker for agar plates. Plasmid DNA was isolated using QIAprep Spin Miniprep Kit (27104) from 5 ml liquid over night cultures (37 ˚C, 160 rpm). Positive clones were selected using control restriction digests followed by agarose gel electrophoresis and ethidium bromide staining. Sequences were confirmed using the sequencing service provided by GATC-Biotech (http://www.gatc-biotech.com).

For site directed mutagenesis applications, I followed the guide lines as described in the Quick change II side directed mutagenesis kit (http://www.genomics.agilent.com/en/Site-Directed-Mutagenesis/QuikChange-II/?cid=AG-PT-175&tabId=AG-PR-1161) except that Kappa HiFi polymerase was used for the PCR reaction.

5.3 Protein expression

Proteins were either expressed in *Escherichia coli* BL21-RIL CodonPlus Competent Cells (Stratagene, Cat no: 230240) of SF 21 cells (Invitrogen/life technologies; Cat no: 11497-013).

For *Escherichia coli* based expression, 50 µl of cells were incubated on ice with 100 ng of Plasmid DNA, heat shocked for 45 seconds at 42 ˚C and transferred back on ice for another minute, supplemented with 1 ml standard LB medium (media kitchen LRI) and incubated for 40 minutes at 37 ˚C. Then, 20 µl were added onto agar plates (media kitchen, with 30 µg/µl Chloramphenicol and Kanamycin (30 µg/µl) or Amplicilin (100 µg/µl) and spread using sterile glass beads.

Agar plates were incubated at 37 ˚C over night. On the next evening a single colony was picked for an overnight culture (1 litre LB medium, supplemented with antibiotics and 2 % Glucose at 160 RPM and 37 ˚C using a 5 litre Erlenmeyer flask and a shaker. On the next day, overnight cultures were diluted 1:12 in LB medium with antibiotics and 0.5 % Glycerol (but without glucose) and were transferred to 25 ˚C while shaking at 160 RPM was maintained. The cell density was monitored using the OD_{600} on a conventional spectrophotometer (Ultrospec 3100 pro, Amersham). Once an OD_{600} of 0.8 (± 0.2) was reached, the cultures were transferred to 18 ˚C and expression was induced with 0.5 mM Isopropyl β-D-1-thiogalactopyranoside (Roche, 11411446001)

for about 12 hours. Cells were centrifuged (20 min, 4000g, JLA 81000 rotor (Beckman) 4 ˚C) and the supernatant was discarded. Pellets were re-suspended in PBS (10 mM Na_2HPO_4, 18 mM KH_2PO_4, 27 mM KCl, 137 mM NaCl, pH 7.4) and transferred into 50 ml Falcon tubes (Corning) and centrifuged (15 min, 4000g, centrifuge (Multifuge X1R, Thermo)). The supernatant was discarded. Pellets were used directly for further purification or frozen in liquid nitrogen and stored until further use at – 80 ˚C degree.

For baculovirus mediated protein expressions in Sf 21 insect cells, the Bac-to-Bac® Baculovirus Expression pFastBac system was used (Invitrogen/life technologies) according to the manufactures recommendations.

Bacmids were produced in DH10 MultiBac cells (Bieniossek et al., 2012). DH10 MultiBac cells were transformed with 100 ng pFastBac vector using standard electroporation (Dower et al., 1988) and were grown in SOC (life technologies) medium for 4-8 hours and plated onto agar plates with Gentamycin (7µg/ml), Teracyclin (10 µg/ml), Kanamycin (50µg/ml), Bluo-Gal/X-Gal (0.1 mg/ml) and Isopropyl β-D-1-thiogalactopyranoside (40 µg/ml). Colonies were selected based on their colour (blue white screen, (Ullmann et al., 1967)) after 2 days at 37 ˚C. Colonies were restreaked and incubated for another 2 days to confirm that the selected clones maintained their colour. Bacmids were isolated from 100 ml LB overnight cultures (160 RPM, 37 ˚C) using NucleoBond® Xtra Midi prep kits (Macherey-Nagel, 740410.10).

Sf21 cells were cultured in Sf-900™ II SFM medium (life technologies) at 27 ˚C in suspension under constant shaking.

For baculovirus generation, insect cells were seeded in 6 well plates (Corning) at a density of 900,000 cells per well in 2 ml medium for 1 hour. Transfection was performed using FuGENE-HD (Promega, E2311) and 1 ug of bacmid DNA per 900,000 cells. After 72 hours virus containing supernatant was harvested and filtered (PVDF membrane, 0.22 µm, Millipore) and added to 25 ml of Sf21 suspension culture (density: 0.7 $*10^6$ cells/ml). The cell viability was monitored using Trypan blue (life technologies) and the cell density was measured using a Neubauer improved cell counting chamber. The cell density was adjusted to 0.7 $*10^6$ cells/ml daily. One day after the cells stopped growing and showed clear morphological changes in response to infection (Howes et al., 1956), the virus was harvested. Cells were centrifuged at 1000 g for 5 min and the supernatant was collected and filtered. The exact virus titer was not

determined as 1:100 dilutions (ml virus solution: ml Sf21 cell suspension at 0.7 *10^6 cells/ml) normally gave good expressions after 48-72 hours post infection. Expressions were monitored by Western blots (see below).

5.4 Protein Purification and protein labelling

All purified proteins were separated on SDS gels followed by comassie brilliant Blue (Fischer) staining to test for purity (**see Fig.28**). Protein identities were confirmed using mass spec after SDS gel electrophoresis and protease digest using standard methods (performed by protein analysis and proteomics facility, Clare Hall or Mass spec facility EMBL, Heidelberg, not shown). Protein concentrations were measured using their absorbance at 280 nm. The extinction coefficient was calculated based on their primary amino acid composition as described (Gill and von Hippel, 1989).

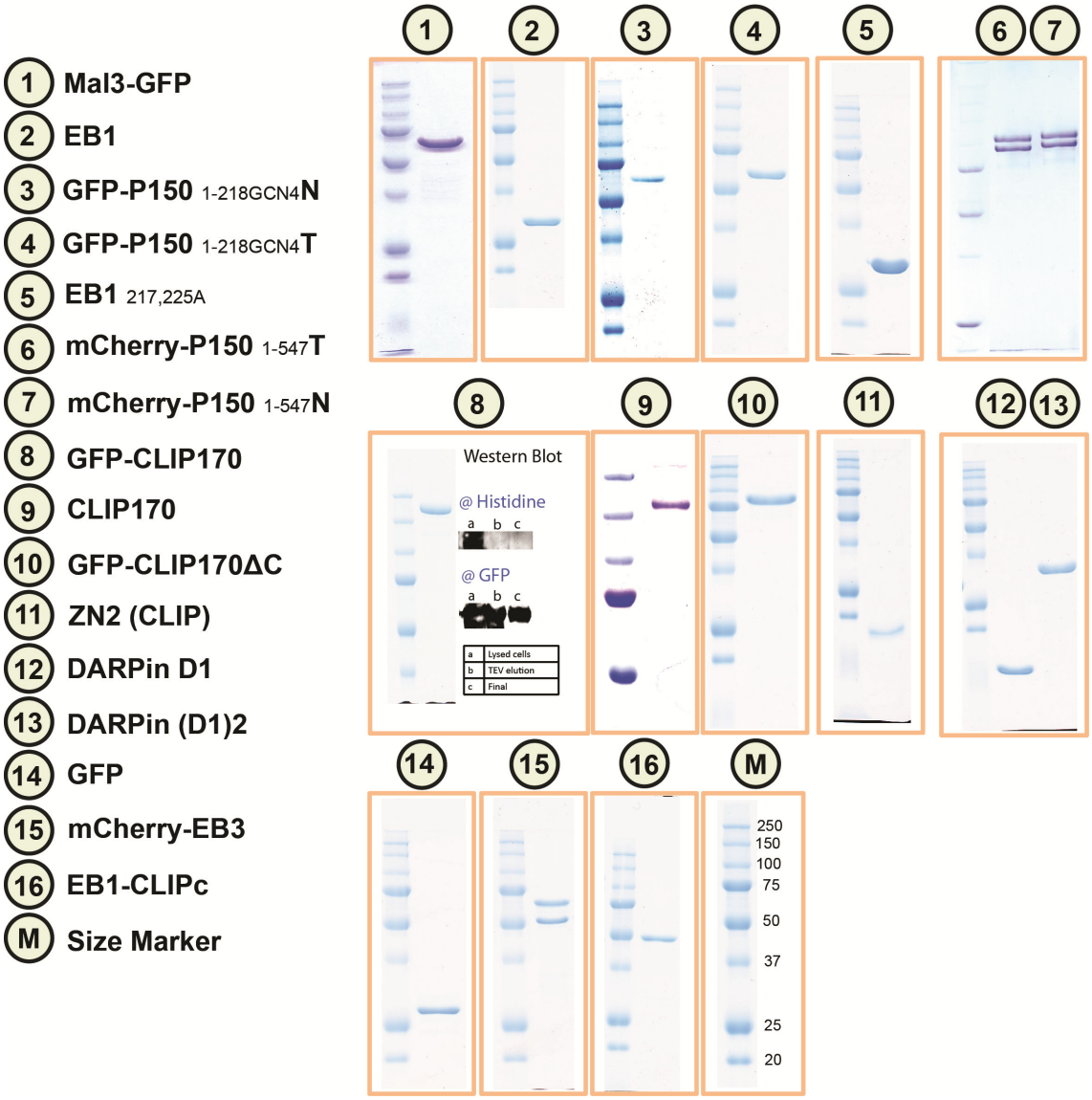

Figure 28: Coomassie brilliant blue stained SDS gels of purified proteins

SDS-PAGE was applied to test the purity of recombinant proteins. The double band seen in mCherry (6,7,15) is not an impurity (mass spec, data not shown). Fluorescent proteins undergo a maturation process where covalent bonds within the poly peptide chain are broken. The two polypeptide chains are either not separated during the denaturation process or are the double band is a result of incomplete maturation of mCherry. TEV protease based elutions from purification coulms were monitored by Western blots against the His tag and another part of the protein. An example for GFP-CLIP170 is given (8).

5.4.1 Tubulin

Tubulin was purified as decribed (Castoldi and Popov, 2003) and NHS- biotin (Pierce) , NHS-Alexa568 (Life technology)or NHS-Cy5 (Lumiprobe) was covalently bound as decribed (Hyman et al., 1991). For all experiments that involved zinc binding domains

of CLIP170, EGTA was removed from tubulin via an additional polymerization/depolymerisation cycle in the absence of EGTA.

5.4.2 Mal3-GFP from *Schizosaccharomyces pombe*

Mal3-GFP was purified expressed from existing expression plasmids and purified as described in (Maurer et al., 2011).

5.4.3 Human EB1 (untagged)

Untagged human EB1 was expressed from an existing expression plasmid as described in (Honnappa et al., 2005). Cells from 4.5 litre expression culture were lysed in 20 mM Bis/Tris Buffer (pH 6), supplemented with DNAse I (Roche) and Complete protease inhibitors (Roche) using a microfluidizer . Clarified lysates (2 spins at 55 000 rpm for 35 minutes in a TI70 rotor (Beckman) were loaded onto a Mono Q ion exchange column (GE Healthcare)equilibrated with 20 mM Bis Tris Buffer (pH 6). Then, a linear NaCl gradient from 0 to 0.5 M was applied over 160 ml and fractions were collected using an AEKTA purifier (GE Healthcare). An aliquot of each fraction was run on an SDS gel to identify peak fractions of EB1. Peak fractions were pooled and gel filtered using a Superdex 200 column (GE Healthcare) in 20 mM Tris/HCl (pH7,4) and 350 mM NaCl. EB containing peak fractions were pooled and snap frozen in liquid N2. The dimeric state of purified EB1 was confirmed using SEC-MALS (Wyatt) in PBS buffer.

5.4.4 Human p150 constructs

Human p150 DNA was PCR amplified from a cDNA clone containing the human DCN1 gene (GenBank: BX640799.1), corresponding to the neuronal splice variant of p150. Full length p150 was inserted into pfastBacHtb vector (life technology) for baculovirus infected SF21 cell expression. While good expression levels could be achieved, all attempts to purify isolated full length p150 failed due to poor solubility (not shown). Therefore, a fragment consisting of the 547 n terminal amino acids was inserted into a petM11 vector (http://www.embl.de/pepcore/pepcore_services/cloning/choice_vector/ecoli/embl/popup

_emblvectors/), designed for bacterial expressions. An n terminal 6xHistidine tag was followed by a TEV cleavage site, followed by mCherry (as used in (Hentrich and Surrey, 2010) et al) followed by aa 1-547 (based on the neuronal splice variant (Dixit et al., 2008)). The fluorescent tag and p150 were separated by a short GGGGTS linker. This fragment was cloned with Martina Trokter (Surrey group). The artificial GCN4 dimer (as used in (Moughamian et al., 2013)) was cloned by Ruben Buy (Michel Steinmetz lab, PSI, Switzerland) into the pet28a vector (Novagen) with an n terminal 6x histidine tag followed by GFP, the n terminal 218 aa of p150 and the GCN4 sequence (Missimer et al., 2010) for dimerization.

Apart from neuronal cells, the majority of cells express an alternative splice variant of p150 that lacks exon 5-7 (Dixit et al., 2008). I applied directed mutagenesis to directly delete these sequences for all constructs mentioned above.

For purification, cells were lysed in 30 mM Hepes (pH 7.4), 350 mM KCl, 5 mM MgCl2 and 1 mM 2 Mercaptoethanol, DNAse I and complete protease inhibitors using a microfluidizer. Clarified lysates (ultracentrifugation, 40 000 rpm, 4 C,35 minutes, Ti 70 rotor (Beckman) were bound to Proteino Ni-TED beads (Macherey-Nagel , 745200.5 , 0.3 g/litre of expression,) in a batch format, transferred to a column and washed with ~ 100 ml wash buffer (30 mM Hepes (pH 7.4), 350 mM KCl, 1 mM MgCl2 and 1 mM 2 Mercaptoethanol). Proteins were eluted using wash buffer supplemented with 400 mM Imidazol. Peak fractions were concentrated (viva spin) and gel filtered using a Superpose 6 column (GE Healthcare) in wash buffer. Pure fractions were pooled, aliquoted and snap frozen in liquid N2.

5.4.5 Human Full length CLIP170 constructs

Human full length CLIP170 and GFP-CLIP170 were expressed from existing expression constructs (Bieling et al., 2008a) using baculovirus infected SF 21 cells as described above. Both constructs contained an n terminal 6x HIS tag followed by a TEV protease cleavage site (Phan et al., 2002). Because each CLIP170 dimer binds 4 zinc ions (Weisbrich et al., 2007), the growth medium was supplemented with 0.1 mM ZnCl2 (Sigma, 429430). Cells were lysed in lysis buffer (30 mM Hepes , pH 7.4, 400 mM KCl, 20 mM L-Arginin, 20 mM K-Glutamat , 0.01 % Brij 35, 10 mM 2

Mercaptoethanol, 3 mM MgCl2, DNAse I and Complete protease inhibitors using a glass homogenizer (1234F36, Fischer). Clarified lysates (ultracentrifugation, 40 000 rpm, 4 ˚C, 35 minutes, Ti 70 rotor (Beckman) were bound to Proteino Ni-TED beads (Macherey-Nagel , 745200.5 , 0.5 g/litre of expression,) in a batch format, transferred to a column and washed with with ~ 100 ml wash buffer (30 mM Hepes, pH 7.4 400 mM KCl, 20 mM L-Arginin , 20 mM K-Glutamat , 0.01 % Brij 35 (Thermo) 10 mM 2 Mercaptoethanol, 3 mM MgCl2). Then 200 ul (1 mg/ml) of purified GST tagged TEV protease was added for 1 hour at room temperature. TEV cleavage released the CLIP170 constructs from the beads and fractions could be eluted using wash buffer. CLIP170 containing fractions were pooled and concentrated (Viva spin) and gel filtered using a Superose 6 column (GE Healthcare) in wash buffer. Pure fractions were pooled and directly used in TIRF assays to avoid damage due to freeze thaw cycles. The purification procedure of CLIP-170 and the final assay conditions differ from previous studies (Bieling et al., 2008a) as it has been found, that EGTA and imidazole can impair proper folding of the C terminal part of this protein. Therefore, imidazole and EGTA have been omitted throughout purification and final experiments.

5.4.6 Human GFP-CLIP170ΔC

GFP-CLIP170ΔC (synonym GFP-CLIP170 H2) was expressed from existing expression plasmids and purified as described in (Bieling et al., 2008a).

5.4.7 EB-CLIPc

For this construct, a pETG-20A expression vector was used as backbone (for details: http://www.embl.de/pepcore/pepcore_services/cloning/cloning_methods/gateway/destination_vectors/)

A n terminal thioredoxin solubility tag was followed by a 6xhistidine purification tag (Weisbrich et al., 2007), the sequence of human EB1 (from the cDNA clone as used in (Honnappa et al., 2005)) except the last 4 aa which were replaced by the last 40 aa of human CLIP170 (from the cDNA clone as used in (Weisbrich et al., 2007). Protein expression was performed as described above except that LB medium was additionally supplemented with 0.1 mM ZnCl2 (Sigma). Cells were lysed in lysis buffer (30 mM

Hepes (pH 7.4), 350 mM KCl, 5 mM MgCl2, 5 mM 2 Mercaptoethanol, DNAse I and Complete protease inhibitors using a microfluidizer. Clarified lysates (ultracentrifugation, 40 000 rpm, 4 C,35 minutes, Ti 70 rotor (Beckman) were bound to Proteino Ni-TED beads (Macherey-Nagel , 745200.5 , 0.3 g/litre of expression,) in a batch format, transferred to a column and washed with with ~ 100 ml wash buffer (30 mM Hepes (pH 7.4), 350 mM KCl, 1 mM MgCl2, 5 mM 2-Mercaptoethanol). Protein was eluted with wash buffer supplemented with 400 mM Imidazol. Directly after elution, imidazole was removed using PD10 columns (GE healthcare). Gel filtration was performed in wash buffer using Superdex 200 column (GE healthcare). After gel filtration was completed, peak fractions were pooled and directly used for TIRF microscopy experiments to avoid damage due to freeze thaw cycles.

5.4.8 Human CLIP-ZN2

CLIP-ZN2 was expressed from existing expression plasmids (Weisbrich et al., 2007) as described except that the n terminal solubility tag was not cleaved in order to enhance solubility.

5.4.9 Human mCherry EB3

mCherry-EB3 was purified as described in (Montenegro Gouveia et al., 2010) by Indranie Sen from Michel Steinmetz lab (PSI, Switzerland).

5.4.10 Human EB1 Y217A E225A

EB1 with two point mutations at position Y217A and E225A was purified as described in (Montenegro Gouveia et al., 2010) by Indranie Sen from Michel Steinmetz lab (PSI, Switzerland).

5.4.11 Human Dynein constructs

Dynein constructs were cloned, expressed and purified as decribed in (Trokter et al., 2012) by Martina Trokter and Rupam Jha (both Surrey group). Gel samples were not

available at the time point of writing this thesis but can be found in (Trokter et al., 2012).

5.4.12 *Xenopus laevis* XCTK2 (Kinesin 14)

XCTK2 was expressed from existing plasmids in baculovirus infected Sf21 cells and purified as described (Hentrich and Surrey, 2010).

5.4.13 DARPin

All DARPin constructs were purified and labelled in Marcel Knossows lab as decribed by Ludovic Pecqueur (Pecqueur et al., 2012).

5.4.14 *Aequorea victoria* GFP

GFP-His was expressed from existing expression plasmids as decribed (Bieling et al., 2008b) in BL21 RIL cells. Cells were lysed in lysis buffer (30 mM Hepes (pH:7.3), 300 mM KCl, 5 mM $MgCl_2$ 1 mM 2 mercaptoethanol, DNAse I and complete protease inhibitors (Roche) using a micro fluidizer. Clarified lysates (ultracentrifugation, 4 ˚C, 35 minutes at 40 000 rpm in a Ti 70 rotor (Beckman) were bound to Proteino Ni-TED beads (Macherey-Nagel , 745200.5 , 0.3 g/litre of expression,) in a batch format. Beads were loaded onto a column and washed with ~ 100 ml wash buffer (30 mM Hepes (pH:7.3), 300 mM KCl, 5 mM $MgCl_2$ 1 mM 2 mercaptoethanol) using a peristaltic pump (Gilson). Protein was eluted with wash buffer supplemented with 400 mM Imidazol at pH 7.3. Fraction were pooled (based on GFP colour) and gel filtered using a superdex 200 column equilibrated with 30 mM Hepes (pH:7.3), 300 mM KCl, 1 mM $MgCl_2$ 1 mM 2 mercaptoethanol. Peak fractions were concentrated (Viva spin) to 3 mg/ml, aliquted and snap frozen in liquid N2 and stored at – 80 C.

5.4.15 Alexa647-BSA

BSA (Sigma) was dissolved in buffer (50 mM Kpi, pH 8.4 100 mM KCl) at a concentration of 15 mg/ml. Then NHS-Alexa647 (life technology) was added in a 3:1 molar excess over the protein and incubated for 40 minutes at 37 C. The reaction was quenched by adding a Arginin stock solution (pH adjusted to 7.5) to a final

concentration of 50 mM. To separate non bounds dyes from proteins, gel filtration was performed using a superdex 200 column (GE healthcare) equilibrated with 30 mM Hepes (pH 7), 100 mM KCl, 2 mM L-Arginin. Peak fractions were pooled and snap frozen (liquid N2) in small aliquots.

5.5 Peptide synthesis

A MACF derived peptide (HRPTPRAGSR PSTAKP**SKIP** TPQRKSPASK LDKSSKRW) was synthesized (with or without FITC label) by the peptide facility (LRI). As a negative control an SKIP→SXNN peptide was synthesized by the peptide facility at Paul Scherer Institute (PSI, Villingen, Switzerland). Peptides were solubilised using 10 mM Tris/HCl (pH 7) and 50 mM NaCl to a stock concentration of 2 mM.

5.6 TIRF microscopy

All microscopy data for results chapter 2 were acquired on a TILL Imic 4001 TIRF microscope (http://www.till-photonics.com/Products/tirf.php) in 360 mode. Each fluorescent channel was split onto an individual cooled Evolve EMCCD camera (Photometrics), which allowed simultaneous imaging of a 488, 561 and 640 (based on excitation) channels.
All microscopy data for results chapter 3 were acquired on a TILL Imic 4001 TIRF microscope in 360 mode but without simultaneous imaging.
All microscopy data for results chapter 4 were acquired on an Olympus XI71 TIRF microscope.
All experiments in buffer were performed at 30 ˚C.

5.6.1 Experiments in Xenopus laevis egg extracts

Xenopus laevis egg extract were prepared by Hiro Mahbubani from the London Research Institute Bio Resources Unit according to published procedures (Hannak and Heald, 2006).
I supplemented these extracts with 360 nM Alexa 568 tubulin (labelling ratio 53 %) and sperm nuclei at 18 C to allow aster formation. 4 ul of this extract was carefully

transferred to a glass cover slip (using a cut pipette tip) and spread to a thin layer to allow adsorption of asters. After 3 minutes the centre of the extract film was overlaid with another 5 µL of extract to prevent drying and the sample was imaged using TIRF microscopy without counter glass using a 488 laser and a 568 laser at a frame rate of 0.33/sec and an exposure time of 100 ms. After ~90 s, 2 µL of 4.125 µM (D1)2-Alexa488 or GFP in 15 mM sodium phosphate, pH 7.4, 130 mM NaCl, and 100 mM KCl and 5 mM 2-Mercaptoethanol was added to the extract while asters were imaged by TIRF microscopy.

5.6.2 MT dynamics assays and +TIP reconstitution assay

Measurements of MT dynamics and binding patterns of MAPs in conventional flow chambers was essentially performed as described (Telley et al., 2011). Final imaging buffers for results chapter 2 was: 80 mM K-PIPES (pH 6.85), 90 mM KCl, 1 mM EGTA, 4 mM MgCl2 (unless stated otherwise in the figure legend), 5 mM 2 Mercaptoethanol, 50 µg/ml β-casein (Sigma), 2 mM GTP (Fermentas), 0.1 % Methylcellulose, 20 mM Glucose, 1 mg/ml Glucose oxidase (Serva) and 0.5 mg/ml Catalse (Sigma). For Chapter 3 and 4, standard imaging buffer was 80 mM K-PIPES (pH 6.85), 60 mM KCl, 1 mM EGTA, 4 mM MgCl2, 5 mM 2 Mercaptoethanol, 50 µg/ml β-casein (Sigma), 2 mM GTP (Sigma), 0.1 % Methylcellulose, 20 mM Glucose, 1.3 mg/ml Glucose oxidase (Serva) and 0.66 mg/ml Catalse (Sigma), unless stated otherwise in the figure legend. For all experiments that involved zinc binding domains of CLIP170, no EGTA was used unless specifically stated in the figure legend.

Average MT growth velocities were extracted manually from kymographs, except for Fig.9 where automated tracking was used (see image analysis).

5.6.3 Dynamic MT gliding assays

The minus end directed motor xctk2 (kinesin 14 family) was non-specifically adsorbed to Methoxy-PEG coated glass cover slips (Hentrich and Surrey, 2010) in gliding buffer (40 mM K Pipes (pH 6.85), 8 mM MgCl2, 1 mM EGTA, 30 mM KCl, 0.05% methylcellulose, 20 mM glucose, 250 µg/mL β-casein, 2 mM GTP, 4 mM ATP, 1 mM

β-mercaptoethanol. Next, Alexa568 labelled GMPCPP seeds were flown into the chamber and were allowed to attach to surface bound motors for 3 minutes at RT. Unbound GMPCPP seeds were washed out and gliding buffer including 0.66 mg/mL catalase (Sigma), and 1.33 mg/mL glucose oxidase (Serva), 20 μM unlabeled tubulin, 70 nM Mal3-GFP (to visualize growing
MT ends), and 500 nM unlabeled (D1)2 (or no DARPin for the control experiment). Time laps imaging (0.33 frames / sec, 100 ms exposure time for the 488 channel and the 561 channel) was performed at 30 C.

5.6.4 Measuring the effect of (D1)2 on preformed plus ends

To investigate the effects of (D1)2 on preformed MT plus ends, flow chambers were placed on a prewarmend metal block in a temperature controlled plexiglass chamber at 30 ˚C. Cy5 MTs were elongated from Alexa568 labelled GMPCPP stabilized seeds for 90 seconds at 15 μM free tubulin. The cy5 tubulin containing solution was replaced by a prewarmed solution containing 15 μM unlabelled free tubulin, 65 nM of GFP-CLIP170$_{MTB}$ (GFP-CLIPΔC) to visualize the entire MT and 0.5 μM (D1)2 or its storage buffer (CTL). The flow chamber was then transferred to the TIRF microscope and time lapse movies were started ~ 30 seconds after solutions have been replaced. As a measure of MT plus end stability, Cy5labeled plus end segments (extending from GMPCPP seeds) were counted when time lapse movies were started and 90 seconds later. Plus ends were discriminated from minus ends by their growth speeds extracted from kymographs. Ends that had growth velocities higher than 1.3 μm/min were counted as plus ends . In the conditions used here, the average growth velocities for plus and minus ends were 1.87 ±0.35 and 0.63 ± 0.17 μm/min, respectively.

5.7 Microfluidics

Etching and silicon master preparation was performed by David Holmes.

5.7.1 Microfluidic channel fabrication

Microfluidic channels were fabricated in PDMS and glass. The channel designs were drawn using standard CAD software and transferred to chrome glass photolithography masks (JD Photo-Tools, Oldham, Lancashire, UK), **Fig.29**. Silicon masters were created using standard photolithographic and deep reactive ion etching (DRIE) techniques. These masters were then used as templates for casting the polydimethylsiloxane (PDMS) microfluidic channel structures.

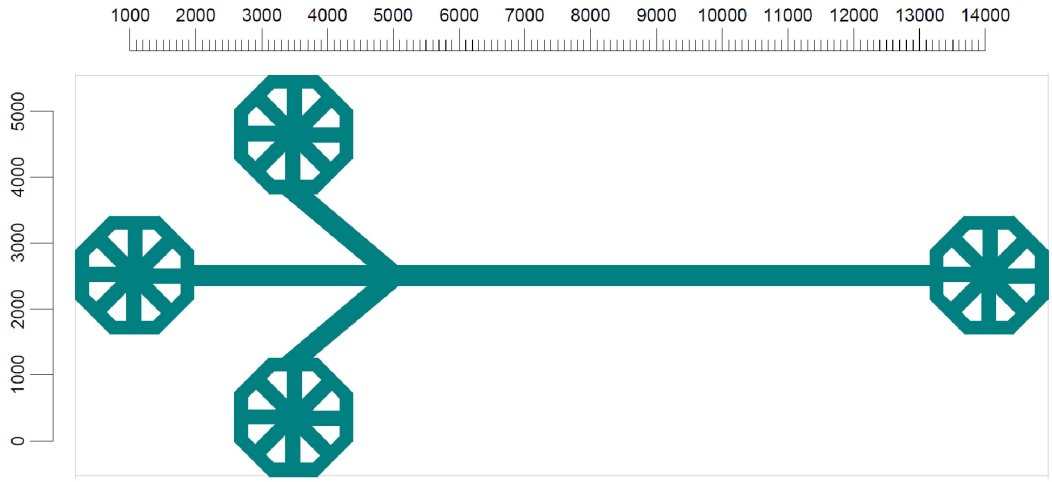

Figure 29: Microfluidics channel design with scale in µm

5.7.2 Fabrication of a silicon master

Silicon wafers (100 mm in diameter) (Compart Technology Ltd., Peterborough, UK) were dehydrated in an oven at 200 °C for 30 minutes. Adhesion promoter hexamethyldisilazane (HDMS) (Sigma Aldrich, Poole, Dorset, UK) was spin coated onto the wafers (4000 rpm for 30 seconds); this was followed by spin coating (4000 rpm for 30 seconds) a 1.8 µm thick layer of S1818 photoresist (Shipley, UK). The wafer and resist were then baked at 110 °C for 60 seconds on a hotplate to remove any residual solvent. The resist coated wafer was then exposed (10 seconds) through a photolithography mask using a mask aligner (Quintel Q4000-6). This was followed by development of the exposed resist in Microposit MF319 developer for 90 seconds, under continuous agitation. The developed wafer was then rinsed in distilled water and

blown dry under a stream of compressed air. Subsequently, a hard bake (2 mins at 115°C on a hotplate) of the resist was performed (to increase resistance to the deep reactive-ion etch (DRIE) process). The wafer was placed in the deep reactive ion etcher (ICP DRIE, Surface Technology Systems, UK) and the Bosch process deep silicon etch was run. After the required number of etch cycles (etch depth per cycle was ~0.5 μm) the wafer was removed from the DRIE. The etch depth was measured using a DektakXT Surface Profiler. The resist was removed from the wafer by ultrasonication in acetone and rinsed in methanol followed by isopropanol (IPA) and blown dry. To render the etched silicon wafer non-stick to PDMS the wafer was treated with a 2% tridecafluoro(1,1,2,2 tetrahydrooctyl) trichlorosilane (Sigma Aldrich, Poole, Dorset, UK) in toluene solution for 1 hour. The wafer was then washed with IPA and blown dry.

5.7.3 PDMS poring

Sylgard 184 Silicon Elastomer Base (Dow corning, 24001673921) and the corresponding curing agent were mixed in a ratio of 9:1 (by weight) at 4 ˚C. Because of its high viscosity complete mixing between the two components had to be ensured using a cut of 10 ml pipete (pietting the mix up and down) and an additional 10 minutes on a turning wheel was applied. The mix was centrifuged (4 ˚C, 4000 g) to remove an excess of air bubbles. The PDMS mix was poured onto the mask and remaining air was removed with a vacuum system (Modulyo 4K, Edwards) for 1 hour at room temperature. The total height of the PDMS layer was ~ 1 cm. Curing (hardening) took place during an incubation at 65 C for ~ 12 hours.

The PDMS layer was removed from the mask and the channels were cut out using a scalpel. Holes for the inlet and out let channels were created using biopsy punchers (Harris Uni-Core I.D. 0.75 mm.)

5.7.4 Glass preparation

PEG-Biotin glass was performed essentially as decribed (Bieling et al., 2010a) except that non stabilized (pure) H_2O_2 was used. Glass cover slips (Menzel, 6776308) had a format of 24x60 mm and each glass slide could be used for the assembly of 1 micro channel.

5.7.5 Bonding

PDMS is hydrophobic and thus does not bond readily to glass surfaces(Bhattacharya et al., 2005). Surface plasma treatment can transiently increase the hydrophilicity of PDMS which allows a strong enough bonding between glass surfaces and PDMS (Bhattacharya et al., 2005). Initial tests showed that surface plasma treatment removed the functional PEG-Biotin groups (not shown). Therefore a small PDMS block (0.4 x 0.8 cm) was manually pressed onto the functionalized glass to protect this area during surface plasma treatment. This spot was marked and later used for imaging. Both the glass and the PDMS block were simultaneously plasma treated for 42 seconds using the Femto Diener Plasma oven . Flow was set to 10 (±1) and power was set to 22%.
The protection was quickly removed using forceps and the glass was pressed onto the PDMS block until a tight seal was formed.

5.7.6 Laminar flow predictions

An online tool to predict if flow is laminar or turbulent was used and flow was predicted to be laminar in the used set up. http://www.ajdesigner.com/fl_reynolds_number/reynolds_number.php.
Except the viscosity, all parameters were known (Temperature was 30 ˚C, Flow speed 15 µl/min, channel geometry was 95 (+/- 5) µm in height and 300 µm in widths (**Fig.29**). To measure the viscosity, an optical trap (JPK) was used as described (Buosciolo, 2004). In brief, the stiffness and the corner frequency of polystyrene beads (Life technologies) was measured as a function of increasing laser power in a liquid of known viscosity (pure water). Next, the same was done for beads in TIRF buffer and the slopes of the resulting linear regressions were compared (not shown). The viscosity of the TIRF buffer was found to be 1.211 +/- 0.2960 [Pa * s/1000] ; approximately 1.5 fold more viscous than water at 30 ˚C. Data analysis was performed by Todd Fallesen (Surrey group).

5.7.7 The microfluidics experiment

Tubing was connected to the PDMS inlets/outlet via short metal extensions (21 g hollow cylinders, cut from "microlances" Becton Dickinson) and Hamilton gas tight syringes (500 µl total volume) in combination with 3 Aladin syringe pumps (World Precision Instruments) were used to introduce solutions into the channels. For better control, the tubing passed manual valves that allowed stopping one flow stream independently of the syringe pump. This was important because after stopping a syringe pump, the build-up pressure relaxes over a few seconds leading to a delayed stop of this flow stream. Vice versa, after switching on a syringe pump the flow stream starts with a delay of few seconds because the pressure has to build up.

The main channel was first washed with ~ 100µl wash buffer (80 mM PIPES (pH 6.85), 90 mM KCl, 1 mM EGTA, 4 mM MgCl2, 5 mM 2-Mercaptoethanol, 50 µg/ml β-casein (Sigma), 0.1 % Methylcellulose), ~ 30µl wash buffer supplemented with 0.05 mg/ml Neutravidin (life technology), ~ 100µl wash buffer, 30 µl wash buffer including biotynilated (estimated to be 15%) and fluorescently labelled (15 %) GMPCPP seeds and again with wash buffer to remove unbound seeds. Flow rates were 50 µl/min for the first 3 solutions. For the seed coupling, flow rates were reduced to 15 µl/min which was a good compromise between seed alignment efficeny with the flow and the overall efficiency of attachment. All experiments were performed at 15 µl/min. The experiment was then started by introducing the first solution of choice into the main channel. Flow was maintained throughout the whole experiment to avoid tubulin depletion and to maintain the alignment of microtubules. When solution needed to be exchanged, the flow stream of one solution was switched off (at the level of the syringe pump) while the buffer stream of the new solution was switched on at the level of the syringe pump while the corresponding manual valve was still closed. The new buffer stream was introduced by opening the corresponding manual valve ~ 1.5 seconds after the first stream was stopped. This method resulted in rather frontal exchanges (not shown) and buffer exchange times between 400 ms and 700 ms. Within these 1.5 seconds the flow speed of the first solution drops but does not reach zero, thus maintaining the MT alignment during a complete buffer exchange.

To monitor buffer exchanges the background fluorescent of the molecules studied could be normally used (e.g. the background florescence of Alexa568 tubulin during tubulin

wash out experiments). When the concentration of fluorescent molecules stayed constant, GFP-His or Alexa647-BSA were used as internal reporter molecules (both used at a final concentration of 125 nM).

Image acquisition was performed simultaneously in all channels (up to three) with exposure times of 100 ms except for Fig.7e where an exposure time of 30 ms was used. Frame rates were between 1 and 32 frames per seconds and are indicated by scale bars where kymographs are presented. For wash out experiments, frame rates between 7.64 and 2 fps were used. The frame rate did not change the average delay time until catastrophe after tubulin removal (not shown). Also, simultaneous illumination did not alter these times under my experimental conditions (not shown).

For tubulin wash out experiments, a catastrophe was defined as the time point when the MT end shrank 3 pixels relative to its position at the time point of tubulin wash out. The time point of wash out is defined as the time when the background florescence of the tubulin channels has dropped below 25 % of its original value. All experiments were performed at 30 ˚C.

5.8 Analytical Gel filtration

Analytical gel filtrations were performed at room temperature. Proteins were dialyzed into the same buffer (10 mM NaPi (pH 7.4), 150 mM NaCl, 5 mM 2-Mercaptoethanol) and mixed at the indicated concentrations and loaded onto a Sephadex 75 gel filtration column (GE Healthcare) at a flow rate of 0.5 ml/minute. Elution profiles were monitored using the change in refractive index (wyatt) as well as the absorbance at 280 nm.

5.9 Gel electrophoresis

Sodium dodecyl sulphate polyacrylamide gel electrophoresis (SDS-PAGE, (Laemmli, 1970)) was performed under denaturating conditions in BioRad chambers using standard procedures. As a size marker, Precision plus Protein Standards (BioRad, 161-0377) were used. Gels were stained using comassie brilliant blue (Meyer and Lamberts, 1965). Agarose gel electrophoresis was performed using standard methods (Viovy,

2000). Tris-Acetate-EDTA buffers were used as running buffers and ethidium bromide to visualize DNA.

5.10 Western Blotting

For most proteins, purification tags were cleaved using TEV protease or Thrombin. To monitor cleavage efficiency, western blots were performed using an any penta-histidine primary antibody.

Protein samples before and after protease digest were separated by SDS-PAGE. Proteins were transferred on nitrocellulose membranes (Whatman Protran) using a tank blotting chamber (Bio Rad) for 90 minutes at a constant current of 385 mA in precooled transfer buffer in a cold room (4 ˚C) . Transfer buffer was 0.025 M Tris, 0.192 M Glycine and 20 % Methanol (Towbin et al., 1992). From here on, all steps were performed at room temperature. Membranes were rinsed with PBS and blocked for 1 hour using Roti Block (Carl Roth) blocking reagent under constant gentle rocking. Next, the membrane was incubated with primary antibody (diluted in block solution as recommended by the manufacture) for 1 hour. Membranes were washed three times in PBST (0.1% Tween) for 5 minutes, incubated in blocking solution for another 5 minutes and then in horseradish peroxidase conjugated secondary antibody (, diluted to in blocking solution) for 45 minutes. Blots were washed with PBST (three times, 5 minutes), PBS (1 time, 5 minutes) and rinsed with water. Amersham ECL Advance – Western Blotting detection Kit was used and chemiluminescence was measured using an Image Quant LAS 400 detector (GE Healthcare).

5.11 Image analysis

Image processing was performed using ImageJ to generate kymographs and to merge images from different channels. For multi colour imaging, a calibration grid was used to correct for camera drifts (**Fig.30**). A Matlab based script for alignment has been written by G. Bohner from the lab to merge two movies based on the spatial information as extracted from the grid images.

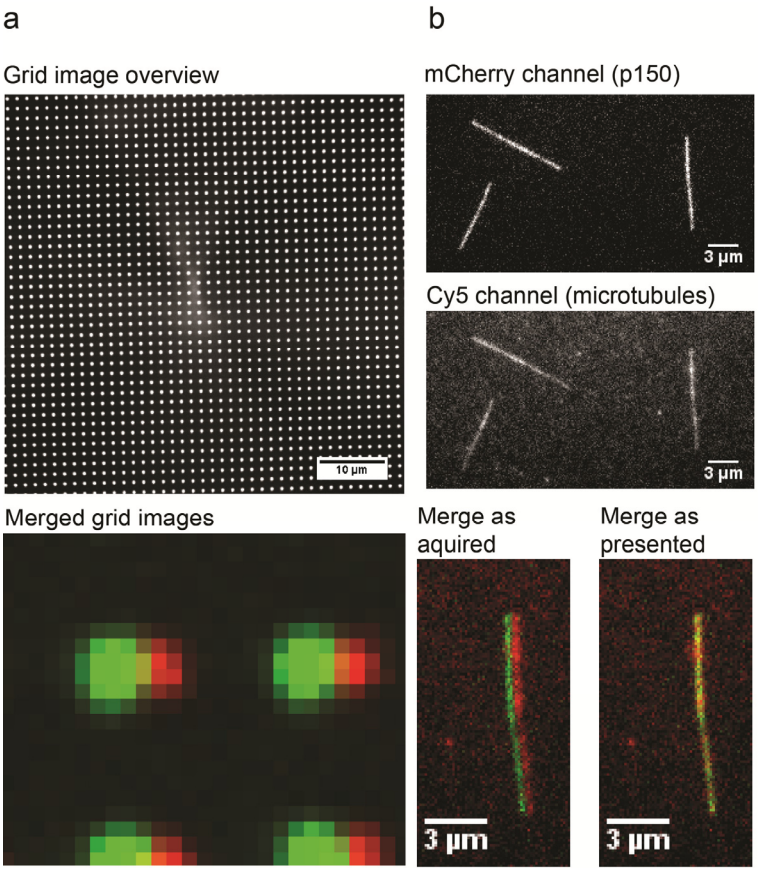

Figure 30: Grid based alignment of individual channels after multi colour TIRF imaging

Channel alignment for multi-colour imaging: Because each fluorescent channel was recorded on an individual camera, grid images were used for proper alignment of different channels after image acquisition. (**a**) Overview of an individual grid imaged with one camera (upper) and merged grid images acquired with 2 different cameras. (**b**) Individual images of the mCherry channel (mCherry $p150_{1\text{-}547N}$, upper) and the cy5 channel (microtubules, middle) and a merged image of the MT (the most right one) before and after alignment correction.1 pixel corresponds to 120 nm.

When two conditions were directly compared, comparable contrast settings were applied for presentation and images were chosen from the same day whenever possible. The build in background subtraction tool in Imaje J ("rolling ball" method) was used for clarity in some cases.

+TIP intensity for figure 7 and 10 was performed using Image J. Grey values were obtained from raw images using line scans through the MT ends in the GFP channels and max intensities were extracted. For background subtractions, another line scan was performed in close proximity (10 pixels away from the MT centre) of the same MT end in the GFP channels to account for the local background (TIRF fields are not uniform

through-out the field of view). The latter value was subtracted from the GFP intensity at the MT ends.

For all other quantifications an automated tracking software was used, in part described in (Maurer et al., 2012), which was mainly developed by G Bohner (3rd author in the paper)

The software is designed to track a MT end positions throughout a time lapse movie of dynamic fluorescently (Cy5 or Alexa 568) labelled MTs and generates time versus position data. Based on these positions the intensities in the corresponding simultaneously acquired MAP channel (GFP) can be extracted (relative to the MT end position). The software crops the images in a way that the MT end is always in the image centre. This allows averaging of several single frames (from the same MT or from different MTs) resulting in MAP binding profiles with enhanced signal to noise ratio and enhanced spatial precision (as compared to the single frame).

Comet averaging and determination of comet length for Mal3 and p150 (Fig.9 and 18) was performed as described (Maurer, in press). A model was used in which Mal3 binding sites transform into the GDP lattice with a rate k.

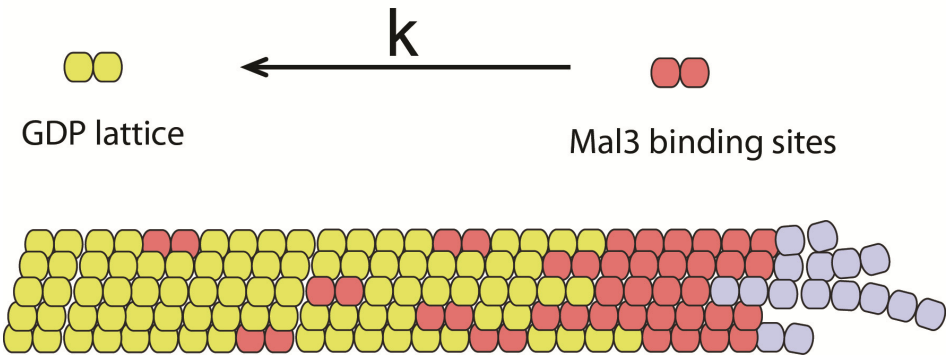

Figure 31: Mal3 binding sites transform into the GDP lattice with a rate k.

To fit the averaged fluorescence signals, the function for the exponential decay

$$E = E0 * e^{-\left(\frac{k*x}{v}\right)} + b$$

was convolved with a Gaussian

$$I = \left(\frac{1}{\sigma\sqrt{2\pi}}\right) * e^{-\left(\frac{x^2}{2\sigma^2}\right)}$$

and least square fitting was applied for minimising the sum of the squared differences between the experimental data and the theoretical model. E0 is the maximal densities of Mal3 binding sites, k is the rate constant for the transition of EB binding sites to GDP lattice tubulin conformations (**Fig.31**), x is the distance away from the microtubule end and v is the growth velocity of the MT and b the offset to correct for lattice binding of Mal3. The life time tau is then defined as: $\tau = (k)^{-1}$

For maximum intensities measurements, the brightest pixel in the MT end region was used. To correct for background fluorescence, the mean of the lowest 20 percentile of the pixel values in a box (6.4μm^2) around the MT end was subtracted.

5.12 Statistics

All error bars represent standard deviations except for the delay times until catastrophe after tubulin removal in chapter 2 where standard errors are presented.

All TIRF based experiments were performed in triplicates (or more). For tubulin wash out experiments, at least 50 MT plus ends were analysed per condition.

When two data sets were compared, Mann-Whytney U tests were performed (Mann, 1947). This test compares two independent groups without the necessity of large normally distributed datasets. Linear regressions were analysed using ANOVA statistics using the standard Origin linear regression statistics.

5.12.1 General computer software

Image processing was performed using ImageJ. Data analysis was performed using Microsoft EXCEL, Origin and MatLab. These programs were also used to prepare graphs presented in the result figures. Figures were prepared using Illustrator. The thesis was written in Microsoft word. Sequencing data were analysed using Ape. *In silico* PCR reaction to design cloning strategies were performed using Serial Cloner.

5.13 Mammalian cell culture

CHO cells were obtained from the cell service facility in Claire Hall. Cells were cultured in phenol red free minimal essential medium (MEM) supplemented with iron-supplemented calf serum (Sigma, C8056-500ML) and MEM non essential amino acids (Sigma M7145-100ML) at 37 ˚C and 5 % CO_2. Trypsin-Versene (Lonza) was used for cell passaging according to standard procedures.

5.14 Live cell imaging

CHO cells were seeded onto Cover slip bottom dishes (Corning, 354089). Cells were allowed to attach to the surface for 24 hours. Transient transfections were performed using FuGene according to the manufactures recommendations. 12 h after transfection, live cell imaging was performed on a spinning disc confocal microscopy system on a Zeiss Observer Z1 in epi fluorescence mode using a 488 argon laser. Imaging was performed at 37 ˚C in phenol red free minimal essential medium (Eagels MEM, as decribed under "mammalian cell culture") supplemented with 40 mM HEPES to keep the pH constant. Frame rates were always 1 fps.

5.14.1 Molecular Biology for live cell imaging

The GFP-$P150_{1\text{-}218GCN4}$T construct (as described under protein expression and purification but without the HIS tag) was subcloned into pcDNA6.2 vector (life technologies). Transcription was under the control of a consecutively active Cytomegalovirus (CMV) promoter.

Chapter 6. Summary and Outlook

What I cannot create, I do not understand.
Richard Feynman, physics lectures blackboard, ca. 1988

Research can be done on several levels. As a first step, a careful description of a process or any phenomenon is necessary. We gain more insight into the observed process if we perturb the process and observe the reaction in response to our manipulation. However, to really understand a process one has to rebuild it from its single components to know which elements do what within this process. The process becomes more transparent and individual components become accessible for a specific manipulation in a defined and controlled manner. Our hypothesis has to predict how the process responds to further manipulations and if it does so poorly, our initial hypothesis is incomplete or incorrect.

In this thesis, *in vitro* reconstitutions of the MT cytoskeleton have been performed to gain knowledge about fundamental processes that underlie MT dynamics itself and the protein network that is associated with it – catastrophe induction, structural transitions during MT growths and +TIPs interactions in particular.

Microtubule dynamics has been reconstituted from purified components more than 25 years ago. Several key studies gained important insight into that process but a conceptual and comprehensive understanding of a hallmark of MT dynamic instability – catastrophes – is still elusive although many possible mechanisms have been postulated (Wade, 2009, Gardner et al., 2013).

These key studies found that growing MTs are protected against depolymerisation by a structure at their ends. Loss of this stabilizing structure causes catastrophe but this loss is not a simple stochastic process, resulting in the notion that catastrophe induction is a multi-step process. However, the nature of this stabilizing end structure and the actual mechanism leading to its loss are not known (Gardner et al., 2013).

Many studies hypothesized that the stabilizing end structure might fluctuate – an untested hypothesis. In this work, Mal3 binding site densities could be linked to momentary MT stability and density fluctuations in these binding sites could be directly visualized. The average rates with which these binding states disappear correlate with MT stability under steady state and non-steady state conditions. My experiments suggest that Mal3 binding sites are either the stabilizing end structure itself, part of the stabilizing end structure or their density is a direct consequence of the density of the actual stabilizing end structure. The latter case would mean that the stabilizing end structure would transform into the Mal3 binding sites and that the disappearance of the stabilizing end structure and the disappearance of Mal3 binding sites would follow a coupled kinetics i.e. if the rate for one transformation increases, the other rate has to increase as well and vice versa. Given that nucleotide analogues that mimic the Mal3 binding site prevent catastrophes (Maurer et al., 2011, Carlier et al., 1989), it is more likely that Mal3 binding sites are or are part of the stabilizing end structure of MT ends.

In contrast, the length of the Mal3 binding zone does not correlate well with MT stability in the performed tubulin wash out experiments, which suggests that not the sum but rather the density of Mal3 binding sites determines filament stability

Furthermore, increasing microtubule age or length destabilizes MTs. This is likely to be caused by tapering (Coombes et al., 2013) although it has not been experimentally measured here.

The presented data suggest that most proposed models are either incomplete or incorrect and provide at the same time new experimental insights into the process of catastrophe induction. Further experiments will be needed to understand the nature of growth fluctuations and their relationship with Mal3 binding site density fluctuation within the context of MT stability and catastrophe induction. More specifically, one would need to find out the reasons for the observed fluctuations of the Mal3 binding site density. These fluctuations may be a consequence of fluctuating instant growth speed during a MT growth episode. This could be tested by performing correlation analysis of instant growth speeds and Mal3-GFP signals. MT growth fluctuations are considerably larger than one would expect from simple polymer models (Gardner et al., 2011a). The reasons for that are not well understood. A recent model hypothesized that slow diffusion and tubulin depletion directly at the MT end might be the reason for these

fluctuations (Yang, 2014). By changing the viscosity and perturbing the proposed tubulin concentration gradients using microfluidics, one should be able to find out if slow diffusion is indeed the reason for the observed growth functions. Alternatively, changing structural featured that are not necessarily related to instant growth speeds might cause the observed Mal3 binding site fluctuations and/or growth fluctuations. Finally, mathematical models are needed to quantitatively link the observed fluctuations to MT stability. For that, rate constants from the available data have to be extracted to build a model, where fluctuating Mal3 binding-site densities are linked to catastrophe probability. Another term would account for a slow decrease of the average binding site density over time as described, which probably reflects evolving tapering at Mt ends.

Many studies underlined the importance of a functional +TIP network at growing microtubule end regions and malfunctions within this network are linked to a variety of severe diseases (Kumar and Wittmann, 2012). Recent progress was made in understanding, why reduced enrichment of the minus motor complex dynein/dynactin at MT ends causes severe neuronal disorders (Moughamian and Holzbaur, 2012, Moughamian et al., 2013). But the mechanisms of how this end accumulation is achieved and how other +TIPs within this network would influence this enrichment was not known. By using a bottom up *in vitro* approach with purified components, I could reconstitute an important part of this +TIP network. The presented data established clear roles for the main classes of +TIPs that directly depend on EBs and provides a possible explanation for the apparent contradiction between structural biology studies and the cell biology literature regarding the role of CLIP170 within the context of dynein/dynactin/p150 plus end tracking.

In order to understand the relationship of dynein targeting to MT ends and its activation, actual cargoes (e.g. RAB/bicausal coated vesicles) should be included into the +TIP reconstitution assay. Analysis of transport initiation position in response to protein activities that control dynein behaviour would greatly improve our understanding of how dynein mediated cargo transport from MT ends is coordinated.

p150/dynactin is not the only regulator of dynein and an expansion of the presented data that include other dynein regulators (Bicausal, LIS1, NDEL1) would be needed to understand the many cellular functions of dynein in the cell. The presented work

focuses on how dynein localisation is regulated by other +TIPs. Future studies would have to link dynein localization and dynein functions in response to its various regulators for a more complete understanding of this highly complex molecular motor.

The sequence of events that occur when GTP bound tubulin in solution is added to the MT lattice has been under debate for a long time. Both GTP and GDP bound tubulin in solution are curved while tubulin is straight in the older part of a GDP MT lattice. The question when tubulin straightening occurs has been subject to many studies (Howard and Hyman, 2009).

The novel D1-tubulin x ray crystal structure (solved by L Pecqueur) further supports the idea that GTP does not pre-straighten the tubulin dimer. This structural information in combination with my TIRF microscopy experiments further suggest, that tubulin at the very MT end is still in a curved state. Consequently, straightening has to occur at a stage after tubulin incorporation, much later than previously appreciated. The presented data are in good agreement with structural data presented by Nawrotek and co-workers. In their high resolution structures of GDP and GTP bound tubulin in complex with a sathmin like domain, they found structural changes between the two species that would explain favourable incorporation for GTP tubulin without the necessity of pre-straightening (Nawrotek et al., 2011).

It would be interesting to see when the actual straightening occurs and if this is linked to GTP hydrolysis. A good tool to study this relationship would be a sensor for curvature that does not block longitudinal interaction. Simultaneous imaging of the Mal3-binding zone (See chapter 2) in response to capping by DARPins might give additional insight into the nature of the stabilizing end strcutre at MT ends.

Taken together, the presented thesis gives three examples where *in vitro* reconstitutions approaches gave new and insightful knowledge about fundamental cellular processes. Structural biology approaches generally provide high spatial resolution but samples are fixed and averaging is often applied. Therefore, dynamics and information about individual species is typically not possible. *In vivo* and *ex vivo* studies are indispensable for the identification of key players within a process. They further contain dynamics information but face a very high level of complexity and are often not as easily accessible to imaging techniques.

In vitro reconstitution experiments especially when observed by fluorescence microscopy, are the bridge between these two disciplines and are built on findings provided by *in vivo*/*ex vivo* studies and structural biology. *In vitro* experiments contain dynamics information but do not face the overwhelming complexity of *in vivo* or *ex vivo* systems. They aim to understand how distinct molecular/microscopic features result in higher ordered system dynamics that give rise to the high degree of complexity found in living organisms

.

Chapter 7. Appendix

Summary of external contributions:

External contributions are specified wherever they are referred to, either in the material method section, the main text or in corresponding figure legends. The following section is therefore redundant but might be still useful to specify where work was not performed by me.

Results Chapter 2

Photo etching for the molds to create PDMS micro channels was performed by David Holmes (London Centre for Nanotechnology, University College London, London, United Kingdom). David Holmes and Nic Cade (Surrey group) helped in the micro channel design. Nic Cade and Todd Fallesen (Surrey group) helped with model fitting. Gergo Bohner, Nic Cade and Sebastian Maurer (all Surrey group) developed Mat Lab scripts for automated microtubule tracking and procedures for comet averaging and fitting. They further developed methods for grid based alignment of individual fluorescent channels for merged presentation of data. Research design was performed by Thomas Surrey and me.

Results Chapter 3

+TIPs: Martinas Trokter (Thomas Surrey group) cloned all dynein constructs and mcherry-P150$_{1\text{-}547N}$. Martina Trokter and Rupam Jha purified the dynein complex and an artificial dynein motor domain dimer. MACF peptides were designed in Michel Steinmetz lab (Laboratory of Biomolecular Research, Paul Scherrer Institut, Villigen PSI, Switzerland) by him, Ruben Buey and Indrani Sen and synthesised at the Paul Scherer Institute and the peptide facility at LRI. Ruben Buey cloned GFP-P150 $_{1\text{-}218GCN4}$ *Xenopus laevis* egg extraxts for control experiments (not shown in this thesis) were prepared by Emanual Boutant (Surrey group) or Hiro Mahbubani from the LRI Bio Resource Unit. Iris Lueke (Surrey group) and Janet Seiler (Purification facility, EMBL, Heidelberg) helped with insect cell culture and virus amplification. Research design was performed by Thomas Surrey, Michel Steinmetz and me.

Results Chapter 4

The DARPin screen was performed by Ludovic Pecqueur in the group of Marcel Knossow (Laboratoire d'Enzymologie et Biochimie Structurales, Centre de Recherche

de Gif, Centre National de la Recherche Scientifique, 91198 Gif sur Yvette, France), Birgit Dreier in the group of Andreas Plückthun (Department of Biochemistry, University of Zurich, CH-8057 Zurich, Switzerland) and Qiyang Jiang in the group of Chunguang Wang (Institute of Protein Research, School of Life Sciences and Technology, Tongji University, Shanghai 200092, China). Ludovic Pecqueur performed purifications of D1 and (D1)2, performed DARPin labellings, solved the x ray crystal structure of the DARPin – tubulin complex and performed binding assays (Fluorescence anisotropy) and turbidity measurements (not shown). *Xenopus laevis* egg extracts were prepared by Hiro Mahbubani from the LRI Bio Resource Unit. Research design was performed by Ludovic Pecqueur, Marcel Knossow, Bernoit Gigant, Thomas Surrey and me.

Reference List

AHMED, S., SUN, S., SIGLIN, A. E., POLENOVA, T. & WILLIAMS, J. C. 2010. Disease-associated mutations in the p150(Glued) subunit destabilize the CAP-gly domain. *Biochemistry,* 49**,** 5083-5.

AKHMANOVA, A., HOOGENRAAD, C. C., DRABEK, K., STEPANOVA, T., DORTLAND, B., VERKERK, T., VERMEULEN, W., BURGERING, B. M., DE ZEEUW, C. I., GROSVELD, F. & GALJART, N. 2001. Clasps are CLIP-115 and -170 associating proteins involved in the regional regulation of microtubule dynamics in motile fibroblasts. *Cell,* 104**,** 923-35.

AKHMANOVA, A. & STEINMETZ, M. O. 2010. Microtubule +TIPs at a glance. *J Cell Sci,* 123**,** 3415-9.

AL-BASSAM, J., KIM, H., BROUHARD, G., VAN OIJEN, A., HARRISON, S. C. & CHANG, F. 2010. CLASP promotes microtubule rescue by recruiting tubulin dimers to the microtubule. *Dev Cell,* 19**,** 245-58.

ALLEN, P. B., MILNE, G., DOEPKER, B. R. & CHIU, D. T. 2010. Pressure-driven laminar flow switching for rapid exchange of solution environment around surface adhered biological particles. *Lab Chip,* 10**,** 727-33.

AMAYED, P., CARLIER, M. F. & PANTALONI, D. 2000. Stathmin slows down guanosine diphosphate dissociation from tubulin in a phosphorylation-controlled fashion. *Biochemistry,* 39**,** 12295-302.

AMBROSE, J. C., LI, W., MARCUS, A., MA, H. & CYR, R. 2005. A minus-end-directed kinesin with plus-end tracking protein activity is involved in spindle morphogenesis. *Mol Biol Cell,* 16**,** 1584-92.

AMOS, L. A. & SCHLIEPER, D. 2005. Microtubules and maps. *Adv Protein Chem,* 71**,** 257-98.

AMRUTE-NAYAK, M. & BULLOCK, S. L. 2012. Single-molecule assays reveal that RNA localization signals regulate dynein-dynactin copy number on individual transcript cargoes. *Nat Cell Biol,* 14**,** 416-23.

ASENJO, A. B., CHATTERJEE, C., TAN, D., DEPAOLI, V., RICE, W. J., DIAZ-AVALOS, R., SILVESTRY, M. & SOSA, H. 2013. Structural model for tubulin recognition and deformation by kinesin-13 microtubule depolymerases. *Cell Rep,* 3**,** 759-68.

AYAZ, P., YE, X., HUDDLESTON, P., BRAUTIGAM, C. A. & RICE, L. M. 2012. A TOG:alphabeta-tubulin complex structure reveals conformation-based mechanisms for a microtubule polymerase. *Science,* 337**,** 857-60.

BARBIER, P., DORLEANS, A., DEVRED, F., SANZ, L., ALLEGRO, D., ALFONSO, C., KNOSSOW, M., PEYROT, V. & ANDREU, J. M. 2010. Stathmin and interfacial microtubule inhibitors recognize a naturally curved conformation of tubulin dimers. *J Biol Chem,* 285**,** 31672-81.

BELLETTI, B. & BALDASSARRE, G. 2011. Stathmin: a protein with many tasks. New biomarker and potential target in cancer. *Expert Opin Ther Targets,* 15**,** 1249-66.

BELMONT, L. D. & MITCHISON, T. J. 1996. Identification of a protein that interacts with tubulin dimers and increases the catastrophe rate of microtubules. *Cell,* 84**,** 623-31.

BHATTACHARYA, R., YANG, H. & CABRAL, F. 2011. Class V beta-tubulin alters dynamic instability and stimulates microtubule detachment from centrosomes. *Mol Biol Cell,* 22**,** 1025-34.

BHATTACHARYA, S., DATTA, A., BERG, J. M. & GANGOPADHYAY, S. 2005. Studies on surface wettability of poly(dimethyl) siloxane (PDMS) and glass under oxygen-plasma treatment and correlation with bond strength. *Journal of Microelectromechanical Systems,* 14.

BIELING, P., KANDELS-LEWIS, S., TELLEY, I. A., VAN DIJK, J., JANKE, C. & SURREY, T. 2008a. CLIP-170 tracks growing microtubule ends by dynamically recognizing composite EB1/tubulin-binding sites. *The Journal of Cell Biology,* 183**,** 1223-1233.

BIELING, P., LAAN, L., SCHEK, H., MUNTEANU, E. L., SANDBLAD, L., DOGTEROM, M., BRUNNER, D. & SURREY, T. 2007. Reconstitution of a microtubule plus-end tracking system in vitro. *Nature,* 450**,** 1100-5.

BIELING, P., TELLEY, I. A., HENTRICH, C., PIEHLER, J. & SURREY, T. 2010a. Fluorescence Microscopy Assays on Chemically Functionalized Surfaces for Quantitative Imaging of Microtubule, Motor, and +TIP Dynamics. *Methods Cell Biology,* 95**,** 555-580.

BIELING, P., TELLEY, I. A., PIEHLER, J. & SURREY, T. 2008b. Processive kinesins require loose mechanical coupling for efficient collective motility. *EMBO Rep,* 9**,** 1121-7.

BIELING, P., TELLEY, I. A. & SURREY, T. 2010b. A minimal midzone protein module controls formation and length of antiparallel microtubule overlaps. *Cell,* 142**,** 420-32.

BIENIOSSEK, C., IMASAKI, T., TAKAGI, Y. & BERGER, I. 2012. MultiBac: expanding the research toolbox for multiprotein complexes. *Trends Biochem Sci,* 37**,** 49-57.

BINZ, H. K., STUMPP, M. T., FORRER, P., AMSTUTZ, P. & PLUCKTHUN, A. 2003. Designing repeat proteins: well-expressed, soluble and stable proteins from combinatorial libraries of consensus ankyrin repeat proteins. *J Mol Biol,* 332**,** 489-503.

BOERSMA, Y. L. & PLUCKTHUN, A. 2011. DARPins and other repeat protein scaffolds: advances in engineering and applications. *Curr Opin Biotechnol,* 22**,** 849-57.

BOLTERAUER, H., LIMBACH, H. J. & TUSZYNSKI, J. A. 1999. Models of assembly and disassembly of individual microtubules: stochastic and averaged equations. *J Biol Phys,* 25**,** 1-22.

BORISY, G. G. & TAYLOR, E. W. 1967. The mechanism of action of colchicine. Binding of colchincine-3H to cellular protein. *J Cell Biol,* 34**,** 525-33.

BORNENS, M. 2012. The centrosome in cells and organisms. *Science,* 335**,** 422-6.

BOWNE-ANDERSON, H., ZANIC, M., KAUER, M. & HOWARD, J. 2013. Microtubule dynamic instability: a new model with coupled GTP hydrolysis and multistep catastrophe. *Bioessays,* 35**,** 452-61.

BRINGMANN, H., SKINIOTIS, G., SPILKER, A., KANDELS-LEWIS, S., VERNOS, I. & SURREY, T. 2004. A kinesin-like motor inhibits microtubule dynamic instability. *Science,* 303**,** 1519-22.

BRINKLEY, B. R. 1985. Microtubule organizing centers. *Annu Rev Cell Biol,* 1**,** 145-72.

BROUHARD, G. J., STEAR, J. H., NOETZEL, T. L., AL-BASSAM, J., KINOSHITA, K., HARRISON, S. C., HOWARD, J. & HYMAN, A. A. 2008. XMAP215 is a processive microtubule polymerase. *Cell,* 132**,** 79-88.

BRUN, L., RUPP, B., WARD, J. J. & NEDELEC, F. 2009. A theory of microtubule catastrophes and their regulation. *Proc Natl Acad Sci U S A,* 106**,** 21173-8.

BRUNET, S., SARDON, T., ZIMMERMAN, T., WITTMANN, T., PEPPERKOK, R., KARSENTI, E. & VERNOS, I. 2004. Characterization of the TPX2 domains involved in microtubule nucleation and spindle assembly in Xenopus egg extracts. *Mol Biol Cell,* 15**,** 5318-28.

BRYLAWSKI, B. P. & CAPLOW, M. 1983. Rate for nucleotide release from tubulin. *J Biol Chem,* 258**,** 760-3.

BUEY, R. M., SEN, I., KORTT, O., MOHAN, R., GFELLER, D., VEPRINTSEV, D., KRETZSCHMAR, I., SCHEUERMANN, J., NERI, D., ZOETE, V., MICHIELIN, O., DE PEREDA, J. M., AKHMANOVA, A., VOLKMER, R. & STEINMETZ, M. O. 2012. Sequence determinants of a microtubule tip localization signal (MtLS). *J Biol Chem*.

BUKOWSKA, M. A. & GRUTTER, M. G. 2013. New concepts and aids to facilitate crystallization. *Curr Opin Struct Biol,* 23**,** 409-16.

BUOSCIOLO, S. 2004. New calibration method for position detector for simultaneous measurements of force constants and local viscosity in optical tweezers. *Optics Communication*.

CAPLOW, M. & SHANKS, J. 1996. Evidence that a single monolayer tubulin-GTP cap is both necessary and sufficient to stabilize microtubules. *Mol Biol Cell,* 7**,** 663-75.

CARLIER, M. F., DIDRY, D., SIMON, C. & PANTALONI, D. 1989. Mechanism of GTP hydrolysis in tubulin polymerization: characterization of the kinetic intermediate microtubule-GDP-Pi using phosphate analogues. *Biochemistry,* 28**,** 1783-91.

CARLIER, M. F., HILL, T. L. & CHEN, Y. 1984. Interference of GTP hydrolysis in the mechanism of microtubule assembly: an experimental study. *Proc Natl Acad Sci U S A,* 81**,** 771-5.

CARLIER, M. F. & PANTALONI, D. 1988. Binding of phosphate to F-ADP-actin and role of F-ADP-Pi-actin in ATP-actin polymerization. *J Biol Chem,* 263**,** 817-25.

CARLIER, M. F., PANTALONI, D. & KORN, E. D. 1987. The mechanisms of ATP hydrolysis accompanying the polymerization of Mg-actin and Ca-actin. *J Biol Chem,* 262**,** 3052-9.

CASPI, M., COQUELLE, F. M., KOIFMAN, C., LEVY, T., ARAI, H., AOKI, J., DE MEY, J. R. & REINER, O. 2003. LIS1 missense mutations: variable phenotypes result from unpredictable alterations in biochemical and cellular properties. *J Biol Chem,* 278**,** 38740-8.

CASTLE, B. T. & ODDE, D. J. 2013. Brownian dynamics of subunit addition-loss kinetics and thermodynamics in linear polymer self-assembly. *Biophys J,* 105**,** 2528-40.

CASTOLDI, M. & POPOV, A. V. 2003. Purification of brain tubulin through two cycles of polymerization-depolymerization in a high-molarity buffer. *Protein Expr Purif,* 32**,** 83-8.

CAUDRON, M., BUNT, G., BASTIAENS, P. & KARSENTI, E. 2005. Spatial coordination of spindle assembly by chromosome-mediated signaling gradients. *Science,* 309**,** 1373-6.

CHRETIEN, D., FULLER, S. D. & KARSENTI, E. 1995. Structure of growing microtubule ends: two-dimensional sheets close into tubes at variable rates. *J Cell Biol,* 129**,** 1311-28.

CHRETIEN, D., METOZ, F., VERDE, F., KARSENTI, E. & WADE, R. H. 1992. Lattice defects in microtubules: protofilament numbers vary within individual microtubules. *J Cell Biol,* 117**,** 1031-40.

CHUNG, B. M., ROTTY, J. D. & COULOMBE, P. A. 2013. Networking galore: intermediate filaments and cell migration. *Curr Opin Cell Biol,* 25**,** 600-12.

CIANI, B., BJELIC, S., HONNAPPA, S., JAWHARI, H., JAUSSI, R., PAYAPILLY, A., JOWITT, T., STEINMETZ, M. O. & KAMMERER, R. A. 2010. Molecular basis of coiled-coil oligomerization-state specificity. *Proc Natl Acad Sci U S A,* 107**,** 19850-5.

COOMBES, C. E., YAMAMOTO, A., KENZIE, M. R., ODDE, D. J. & GARDNER, M. K. 2013. Evolving tip structures can explain age-dependent microtubule catastrophe. *Curr Biol,* 23**,** 1342-8.

COOPER, J. A. & SEPT, D. 2008. New insights into mechanism and regulation of actin capping protein. *Int Rev Cell Mol Biol,* 267**,** 183-206.

COQUELLE, F. M., CASPI, M., CORDELIERES, F. P., DOMPIERRE, J. P., DUJARDIN, D. L., KOIFMAN, C., MARTIN, P., HOOGENRAAD, C. C., AKHMANOVA, A., GALJART, N., DE MEY, J. R. & REINER, O. 2002. LIS1, CLIP-170's Key to the Dynein/Dynactin Pathway. *Molecular and Cellular Biology,* 22**,** 3089-3102.

CULVER-HANLON, T. L., LEX, S. A., STEPHENS, A. D., QUINTYNE, N. J. & KING, S. J. 2006. A microtubule-binding domain in dynactin increases dynein processivity by skating along microtubules. *Nat Cell Biol,* 8**,** 264-70.

DAMMERMANN, A., DESAI, A. & OEGEMA, K. 2003. The minus end in sight. *Curr Biol,* 13**,** R614-24.

DESAI, A. & MITCHISON, T. J. 1997. Microtubule polymerization dynamics. *Annu Rev Cell Dev Biol,* 13**,** 83-117.

DIMITROV, A., QUESNOIT, M., MOUTEL, S., CANTALOUBE, I., POUS, C. & PEREZ, F. 2008. Detection of GTP-tubulin conformation in vivo reveals a role for GTP remnants in microtubule rescues. *Science,* 322**,** 1353-6.

DIX, C. I., SOUNDARARAJAN, H. C., DZHINDZHEV, N. S., BEGUM, F., SUTER, B., OHKURA, H., STEPHENS, E. & BULLOCK, S. L. 2013. Lissencephaly-1 promotes the recruitment of dynein and dynactin to transported mRNAs. *J Cell Biol,* 202**,** 479-94.

DIXIT, R., LEVY, J. R., TOKITO, M., LIGON, L. A. & HOLZBAUR, E. L. 2008. Regulation of dynactin through the differential expression of p150Glued isoforms. *J Biol Chem,* 283**,** 33611-9.

DOGTEROM, M. & SURREY, T. 2013. Microtubule organization in vitro. *Curr Opin Cell Biol,* 25**,** 23-9.

DOREY, F. 2011. Statistics in brief: Interpretation and use of p values: all p values are not equal. *Clin Orthop Relat Res,* 469**,** 3259-61.

DOWER, W. J., MILLER, J. F. & RAGSDALE, C. W. 1988. High efficiency transformation of E. coli by high voltage electroporation. *Nucleic Acids Res,* 16**,** 6127-45.

DRAGESTEIN, K. A., VAN CAPPELLEN, W. A., VAN HAREN, J., TSIBIDIS, G. D., AKHMANOVA, A., KNOCH, T. A., GROSVELD, F. & GALJART, N. 2008. Dynamic behavior of GFP-CLIP-170 reveals fast protein turnover on microtubule plus ends. *J Cell Biol,* 180**,** 729-37.

DRECHSEL, D. N. & KIRSCHNER, M. W. 1994. The minimum GTP cap required to stabilize microtubules. *Curr Biol,* 4**,** 1053-61.

DU, Y., ENGLISH, C. A. & OHI, R. 2010. The kinesin-8 Kif18A dampens microtubule plus-end dynamics. *Curr Biol,* 20**,** 374-80.

DUELLBERG, C., FOURNIOL, F. J., MAURER, S. P., ROOSTALU, J. & SURREY, T. 2013. End-binding proteins and Ase1/PRC1 define local functionality of structurally distinct parts of the microtubule cytoskeleton. *Trends Cell Biol,* 23**,** 54-63.

EBEL, H. & GUNTHER, T. 1980. Magnesium metabolism: a review. *J Clin Chem Clin Biochem,* 18**,** 257-70.

ETIENNE-MANNEVILLE, S. 2013. Microtubules in cell migration. *Annu Rev Cell Dev Biol,* 29**,** 471-99.

FARRER, M. J., HULIHAN, M. M., KACHERGUS, J. M., DACHSEL, J. C., STOESSL, A. J., GRANTIER, L. L., CALNE, S., CALNE, D. B., LECHEVALIER, B., CHAPON, F., TSUBOI, Y., YAMADA, T., GUTMANN, L., ELIBOL, B., BHATIA, K. P., WIDER, C., VILARINO-GUELL, C., ROSS, O. A., BROWN, L. A., CASTANEDES-CASEY, M., DICKSON, D. W. & WSZOLEK, Z. K. 2009. DCTN1 mutations in Perry syndrome. *Nat Genet,* 41**,** 163-5.

FLYVBJERG, H., HOLY, T. E. & LEIBLER, S. 1994. Stochastic dynamics of microtubules: A model for caps and catastrophes. *Phys Rev Lett,* 73**,** 2372-2375.

FLYVBJERG, H., HOLY, T. E. & LEIBLER, S. 1996. Microtubule dynamics: Caps, catastrophes, and coupled hydrolysis. *Phys Rev E Stat Phys Plasmas Fluids Relat Interdiscip Topics,* 54**,** 5538-5560.

FOURNIOL, F. J., SINDELAR, C. V., AMIGUES, B., CLARE, D. K., THOMAS, G., PERDERISET, M., FRANCIS, F., HOUDUSSE, A. & MOORES, C. A. 2010. Template-free 13-protofilament microtubule-MAP assembly visualized at 8 A resolution. *J Cell Biol,* 191**,** 463-70.

FROGER, A. & HALL, J. E. 2007. Transformation of plasmid DNA into E. coli using the heat shock method. *J Vis Exp***,** 253.

FULLER, B. G. 2010. Self-organization of intracellular gradients during mitosis. *Cell Div,* 5**,** 5.

GALJART, N. 2005. CLIPs and CLASPs and cellular dynamics. *Nat Rev Mol Cell Biol,* 6**,** 487-98.

GARD, D. L. & KIRSCHNER, M. W. 1987. Microtubule assembly in cytoplasmic extracts of Xenopus oocytes and eggs. *J Cell Biol,* 105**,** 2191-201.

GARDNER, M. K., CHARLEBOIS, B. D., JANOSI, I. M., HOWARD, J., HUNT, A. J. & ODDE, D. J. 2011a. Rapid microtubule self-assembly kinetics. *Cell,* 146**,** 582-92.

GARDNER, M. K., ZANIC, M., GELL, C., BORMUTH, V. & HOWARD, J. 2011b. Depolymerizing kinesins Kip3 and MCAK shape cellular microtubule architecture by differential control of catastrophe. *Cell,* 147**,** 1092-103.

GARDNER, M. K., ZANIC, M. & HOWARD, J. 2013. Microtubule catastrophe and rescue. *Curr Opin Cell Biol,* 25**,** 14-22.

GENNERICH, A. & VALE, R. D. 2009. Walking the walk: how kinesin and dynein coordinate their steps. *Curr Opin Cell Biol,* 21**,** 59-67.

GIGANT, B., CURMI, P. A., MARTIN-BARBEY, C., CHARBAUT, E., LACHKAR, S., LEBEAU, L., SIAVOSHIAN, S., SOBEL, A. & KNOSSOW, M. 2000. The 4 A X-ray structure of a tubulin:stathmin-like domain complex. *Cell,* 102**,** 809-16.

GILL, S. C. & VON HIPPEL, P. H. 1989. Calculation of protein extinction coefficients from amino acid sequence data. *Anal Biochem,* 182**,** 319-26.

GITTES, F., MICKEY, B., NETTLETON, J. & HOWARD, J. 1993. Flexural rigidity of microtubules and actin filaments measured from thermal fluctuations in shape. *J Cell Biol,* 120**,** 923-34.

GLIKSMAN, N. R., SKIBBENS, R. V. & SALMON, E. D. 1993. How the transition frequencies of microtubule dynamic instability (nucleation, catastrophe, and rescue) regulate microtubule dynamics in interphase and mitosis: analysis using a Monte Carlo computer simulation. *Mol Biol Cell,* 4**,** 1035-50.

GLOTZER, M. 2005. The molecular requirements for cytokinesis. *Science,* 307**,** 1735-9.

GOLDBERG, J. L. 2003. How does an axon grow? *Genes Dev,* 17**,** 941-58.

GOODWIN, S. S. & VALE, R. D. 2010. Patronin regulates the microtubule network by protecting microtubule minus ends. *Cell,* 143**,** 263-74.

GOSHIMA, G., NEDELEC, F. & VALE, R. D. 2005. Mechanisms for focusing mitotic spindle poles by minus end-directed motor proteins. *J Cell Biol,* 171**,** 229-40.

GRILL, S. W., HOWARD, J., SCHAFFER, E., STELZER, E. H. & HYMAN, A. A. 2003. The distribution of active force generators controls mitotic spindle position. *Science,* 301**,** 518-21.

GRUMMT, I. 2006. Actin and myosin as transcription factors. *Curr Opin Genet Dev,* 16**,** 191-6.

HALPIN, D., KALAB, P., WANG, J., WEIS, K. & HEALD, R. 2011. Mitotic spindle assembly around RCC1-coated beads in Xenopus egg extracts. *PLoS Biol,* 9**,** e1001225.

HAMM-ALVAREZ, S. F. & SHEETZ, M. P. 1998. Microtubule-dependent vesicle transport: modulation of channel and transporter activity in liver and kidney. *Physiol Rev,* 78**,** 1109-29.

HANNAK, E. & HEALD, R. 2006. Investigating mitotic spindle assembly and function in vitro using Xenopus laevis egg extracts. *Nat Protoc,* 1**,** 2305-14.

HARMON, R. M. & GREEN, K. J. 2013. Structural and Functional Diversity of Desmosomes. *Cell Commun Adhes*.

HAYASHI, I., WILDE, A., MAL, T. K. & IKURA, M. 2005. Structural basis for the activation of microtubule assembly by the EB1 and p150Glued complex. *Mol Cell,* 19**,** 449-60.

HENTRICH, C. & SURREY, T. 2010. Microtubule organization by the antagonistic mitotic motors kinesin-5 and kinesin-14. *J Cell Biol,* 189**,** 465-80.

HERMESH, O. & JANSEN, R. P. 2013. Take the (RN)A-train: localization of mRNA to the endoplasmic reticulum. *Biochim Biophys Acta,* 1833**,** 2519-25.

HERZOG, W., LEONARD, T., JOUMAA, V., DUVALL, M. & PANCHANGAM, A. 2012. The three filament model of skeletal muscle stability and force production. *Mol Cell Biomech,* 9**,** 175-91.

HIGGS, H. N. 2001. Actin nucleation: nucleation-promoting factors are not all equal. *Curr Biol,* 11**,** R1009-12.

HIROKAWA, N. 1996. Organelle transport along microtubules - the role of KIFs. *Trends Cell Biol,* 6**,** 135-41.

HOLMES, K. C., POPP, D., GEBHARD, W. & KABSCH, W. 1990. Atomic model of the actin filament. *Nature,* 347**,** 44-9.

HOLT, C. E. & BULLOCK, S. L. 2009. Subcellular mRNA localization in animal cells and why it matters. *Science,* 326**,** 1212-6.

HONNAPPA, S., GOUVEIA, S. M., WEISBRICH, A., DAMBERGER, F. F., BHAVESH, N. S., JAWHARI, H., GRIGORIEV, I., VAN RIJSSEL, F. J., BUEY, R. M., LAWERA, A., JELESAROV, I., WINKLER, F. K., WUTHRICH, K., AKHMANOVA, A. & STEINMETZ, M. O. 2009a. An EB1-binding motif acts as a microtubule tip localization signal. *Cell,* 138**,** 366-76.

HONNAPPA, S., GOUVEIA, S. M., WEISBRICH, A., DAMBERGER, F. F., BHAVESH, N. S., JAWHARI, H., GRIGORIEV, I., VAN RIJSSEL, F. J. A., BUEY, R. M. & LAWERA, A. 2009b. An EB1-Binding Motif Acts as a Microtubule Tip Localization Signal. *Cell,* 138**,** 366-376.

HONNAPPA, S., JOHN, C. M., KOSTREWA, D., WINKLER, F. K. & STEINMETZ, M. O. 2005. Structural insights into the EB1-APC interaction. *Embo J,* 24**,** 261-9.

HONNAPPA, S., OKHRIMENKO, O., JAUSSI, R., JAWHARI, H., JELESAROV, I., WINKLER, F. K. & STEINMETZ, M. O. 2006. Key Interaction Modes of Dynamic +TIP Networks. *Molecular Cell,* 23**,** 663-671.

HOOGENRAAD, C. C., AKHMANOVA, A., GROSVELD, F., DE ZEEUW, C. I. & GALJART, N. 2000. Functional analysis of CLIP-115 and its binding to microtubules. *J Cell Sci,* 113 (Pt 12)**,** 2285-97.

HOOGENRAAD, C. C., KOEKKOEK, B., AKHMANOVA, A., KRUGERS, H., DORTLAND, B., MIEDEMA, M., VAN ALPHEN, A., KISTLER, W. M., JAEGLE, M., KOUTSOURAKIS, M., VAN CAMP, N., VERHOYE, M., VAN DER LINDEN, A., KAVERINA, I., GROSVELD, F., DE ZEEUW, C. I. & GALJART, N. 2002. Targeted mutation of Cyln2 in the Williams syndrome critical region links CLIP-115 haploinsufficiency to neurodevelopmental abnormalities in mice. *Nat Genet,* 32**,** 116-27.

HORIO, T. & HOTANI, H. 1986. Visualization of the dynamic instability of individual microtubules by dark-field microscopy. *Nature,* 321**,** 605-7.

HOSNY, N. A., SONG, M., CONNELLY, J. T., AMEER-BEG, S., KNIGHT, M. M. & WHEELER, A. P. 2013. Super-resolution imaging strategies for cell biologists using a spinning disk microscope. *PLoS One,* 8**,** e74604.

HOWARD, J. & HYMAN, A. A. 2009. Growth, fluctuation and switching at microtubule plus ends. *Nat Rev Mol Cell Biol,* 10**,** 569-74.

HOWES, D. W., MELNICK, J. L. & REISSIG, M. 1956. Sequence of morphological changes in epithelial cell cultures infected with poliovirus. *J Exp Med,* 104**,** 289-304.

HU, C. K., COUGHLIN, M., FIELD, C. M. & MITCHISON, T. J. 2011. KIF4 regulates midzone length during cytokinesis. *Curr Biol,* 21**,** 815-24.

HYMAN, A., DRECHSEL, D., KELLOGG, D., SALSER, S., SAWIN, K., STEFFEN, P., WORDEMAN, L. & MITCHISON, T. 1991. Preparation of modified tubulins. *Methods Enzymol,* 196**,** 478-85.

HYMAN, A. A., SALSER, S., DRECHSEL, D. N., UNWIN, N. & MITCHISON, T. J. 1992. Role of GTP hydrolysis in microtubule dynamics: information from a slowly hydrolyzable analogue, GMPCPP. *Mol Biol Cell,* 3**,** 1155-67.

IP, E. H. 2007. General linear models. *Methods Mol Biol,* 404**,** 189-211.

JANKE, C. & KNEUSSEL, M. 2010. Tubulin post-translational modifications: encoding functions on the neuronal microtubule cytoskeleton. *Trends Neurosci,* 33**,** 362-72.

JEGOU, A., CARLIER, M. F. & ROMET-LEMONNE, G. 2011. Microfluidics pushes forward microscopy analysis of actin dynamics. *Bioarchitecture,* 1**,** 271-276.

JIANG, K., TOEDT, G., MONTENEGRO GOUVEIA, S., DAVEY, N. E., HUA, S., VAN DER VAART, B., GRIGORIEV, I., LARSEN, J., PEDERSEN, L. B., BEZSTAROSTI, K., LINCE-FARIA, M., DEMMERS, J., STEINMETZ, M. O., GIBSON, T. J. & AKHMANOVA, A. 2012. A Proteome-wide screen for mammalian SxIP motif-containing microtubule plus-end tracking proteins. *Curr Biol,* 22**,** 1800-7.

JORDAN, M. A., THROWER, D. & WILSON, L. 1992. Effects of vinblastine, podophyllotoxin and nocodazole on mitotic spindles. Implications for the role of microtubule dynamics in mitosis. *J Cell Sci,* 102 (Pt 3)**,** 401-16.

KARDON, J. R. & VALE, R. D. 2009. Regulators of the cytoplasmic dynein motor. *Nat Rev Mol Cell Biol,* 10**,** 854-65.

KERSSEMAKERS, J., HOWARD, J., HESS, H. & DIEZ, S. 2006. The distance that kinesin-1 holds its cargo from the microtubule surface measured by fluorescence interference contrast microscopy. *Proc Natl Acad Sci U S A,* 103**,** 15812-7.

KIM, S. & COULOMBE, P. A. 2007. Intermediate filament scaffolds fulfill mechanical, organizational, and signaling functions in the cytoplasm. *Genes Dev,* 21**,** 1581-97.

KIM, S. & DYNLACHT, B. D. 2013. Assembling a primary cilium. *Curr Opin Cell Biol,* 25**,** 506-11.

KIRSCHNER, M. W. 1980. Implications of treadmilling for the stability and polarity of actin and tubulin polymers in vivo. *J Cell Biol,* 86**,** 330-4.

KITAGAWA, D., VAKONAKIS, I., OLIERIC, N., HILBERT, M., KELLER, D., OLIERIC, V., BORTFELD, M., ERAT, M. C., FLUCKIGER, I., GONCZY, P. & STEINMETZ, M. O. 2011. Structural basis of the 9-fold symmetry of centrioles. *Cell,* 144**,** 364-75.

KOMAROVA, Y., DE GROOT, C. O., GRIGORIEV, I., GOUVEIA, S. M., MUNTEANU, E. L., SCHOBER, J. M., HONNAPPA, S., BUEY, R. M., HOOGENRAAD, C. C., DOGTEROM, M., BORISY, G. G., STEINMETZ, M. O. & AKHMANOVA, A. 2009. Mammalian end binding proteins control persistent microtubule growth. *The Journal of Cell Biology,* 184**,** 691-706.

KUKULSKI, W., SCHORB, M., WELSCH, S., PICCO, A., KAKSONEN, M. & BRIGGS, J. A. 2011. Correlated fluorescence and 3D electron microscopy with high sensitivity and spatial precision. *J Cell Biol,* 192**,** 111-9.

KUMAR, P., LYLE, K. S., GIERKE, S., MATOV, A., DANUSER, G. & WITTMANN, T. 2009. GSK3beta phosphorylation modulates CLASP-microtubule association and lamella microtubule attachment. *J Cell Biol,* 184**,** 895-908.

KUMAR, P. & WITTMANN, T. 2012. +TIPs: SxIPping along microtubule ends. *Trends Cell Biol,* 22**,** 418-28.

LAEMMLI, U. K. 1970. Cleavage of structural proteins during the assembly of the head of bacteriophage T4. *Nature,* 227**,** 680-5.

LAI, C., LIN, X., CHANDRAN, J., SHIM, H., YANG, W. J. & CAI, H. 2007. The G59S mutation in p150(glued) causes dysfunction of dynactin in mice. *J Neurosci,* 27**,** 13982-90.

LANSBERGEN, G., KOMAROVA, Y., MODESTI, M., WYMAN, C., HOOGENRAAD, C. C., GOODSON, H. V., LEMAITRE, R. P., DRECHSEL, D. N., VAN MUNSTER, E., GADELLA, T. W., JR., GROSVELD, F., GALJART, N., BORISY, G. G. & AKHMANOVA, A. 2004. Conformational changes in CLIP-170 regulate its binding to microtubules and dynactin localization. *J Cell Biol,* 166**,** 1003-14.

LAZARUS, J. E., MOUGHAMIAN, A. J., TOKITO, M. K. & HOLZBAUR, E. L. 2013. Dynactin subunit p150(Glued) is a neuron-specific anti-catastrophe factor. *PLoS Biol,* 11**,** e1001611.

LEE, H. S., KOMAROVA, Y. A., NADEZHDINA, E. S., ANJUM, R., PELOQUIN, J. G., SCHOBER, J. M., DANCIU, O., VAN HAREN, J., GALJART, N., GYGI, S. P., AKHMANOVA, A. & BORISY, G. G. 2010. Phosphorylation Controls Autoinhibition of Cytoplasmic Linker Protein-170. *Molecular Biology of the Cell,* 21**,** 2661-2673.

LEE, S. H. & DOMINGUEZ, R. 2010. Regulation of actin cytoskeleton dynamics in cells. *Mol Cells,* 29**,** 311-25.

LEUNG, C. L., SUN, D., ZHENG, M., KNOWLES, D. R. & LIEM, R. K. 1999. Microtubule actin cross-linking factor (MACF): a hybrid of dystonin and dystrophin that can interact with the actin and microtubule cytoskeletons. *J Cell Biol,* 147**,** 1275-86.

LEVAYER, R. & LECUIT, T. 2012. Biomechanical regulation of contractility: spatial control and dynamics. *Trends Cell Biol,* 22**,** 61-81.

LI, H., LIU, X. S., YANG, X., WANG, Y., TURNER, J. R. & LIU, X. 2010. Phosphorylation of CLIP-170 by Plk1 and CK2 promotes timely formation of kinetochore-microtubule attachments. *Embo J,* 29**,** 2953-65.

LI, J., LEE, W. L. & COOPER, J. A. 2005. NudEL targets dynein to microtubule ends through LIS1. *Nat Cell Biol,* 7**,** 686-90.

LI, S., FINLEY, J., LIU, Z. J., QIU, S. H., CHEN, H., LUAN, C. H., CARSON, M., TSAO, J., JOHNSON, D., LIN, G., ZHAO, J., THOMAS, W., NAGY, L. A., SHA, B., DELUCAS, L. J., WANG, B. C. & LUO, M. 2002. Crystal structure of the cytoskeleton-associated protein glycine-rich (CAP-Gly) domain. *J Biol Chem,* 277**,** 48596-601.

LIGON, L. A., TOKITO, M., FINKLESTEIN, J. M., GROSSMAN, F. E. & HOLZBAUR, E. L. 2004. A direct interaction between cytoplasmic dynein and kinesin I may coordinate motor activity. *J Biol Chem,* 279**,** 19201-8.

LOUGHLIN, R., HEALD, R. & NEDELEC, F. 2010. A computational model predicts Xenopus meiotic spindle organization. *J Cell Biol,* 191**,** 1239-49.

LOUGHLIN, R., WILBUR, J. D., MCNALLY, F. J., NEDELEC, F. J. & HEALD, R. 2011. Katanin contributes to interspecies spindle length scaling in Xenopus. *Cell,* 147**,** 1397-407.

LOWE, J., LI, H., DOWNING, K. H. & NOGALES, E. 2001. Refined structure of alpha beta-tubulin at 3.5 A resolution. *J Mol Biol,* 313**,** 1045-57.

LYCANS, R. M., HIGGINS, C. B., TANNER, M. S., BLOUGH, E. R. & DAY, B. S. 2013. Plasma treatment of PDMS for applications of in vitro motility assays. *Colloids Surf B Biointerfaces*.

MANN 1947. On a Test of Whether one of Two Random Variables is Stochastically Larger than the Other. *Annals of Mathematical Statistics,,* 18.

MANNA, T., THROWER, D. A., HONNAPPA, S., STEINMETZ, M. O. & WILSON, L. 2009. Regulation of microtubule dynamic instability in vitro by differentially phosphorylated stathmin. *J Biol Chem,* 284**,** 15640-9.

MARGOLIN, G., GREGORETTI, I. V., CICKOVSKI, T. M., LI, C., SHI, W., ALBER, M. S. & GOODSON, H. V. 2012. The mechanisms of microtubule catastrophe and rescue: implications from analysis of a dimer-scale computational model. *Mol Biol Cell,* 23**,** 642-56.

MARTIN, S. R., SCHILSTRA, M. J. & BAYLEY, P. M. 1993. Dynamic instability of microtubules: Monte Carlo simulation and application to different types of microtubule lattice. *Biophys J,* 65**,** 578-96.

MARZO, I. & NAVAL, J. 2013. Antimitotic drugs in cancer chemotherapy: promises and pitfalls. *Biochem Pharmacol,* 86**,** 703-10.

MAURER, C., BOHNER,GUSTAFSSON, SURREY in press. EB1 accelerates two conformational transitions important for microtubule maturation and dynamics *Current Biology*.

MAURER, S. P., BIELING, P., COPE, J., HOENGER, A. & SURREY, T. 2011. GTPgammaS microtubules mimic the growing microtubule end structure recognized by end-binding proteins (EBs). *Proc Natl Acad Sci U S A,* 108**,** 3988-93.

MAURER, S. P., FOURNIOL, F. J., BOHNER, G., MOORES, C. A. & SURREY, T. 2012. EBs recognize a nucleotide-dependent structural cap at growing microtubule ends. *Cell,* 149**,** 371-82.

MCKENNEY, R. J., VERSHININ, M., KUNWAR, A., VALLEE, R. B. & GROSS, S. P. 2010. LIS1 and NudE induce a persistent dynein force-producing state. *Cell,* 141**,** 304-14.

MCKENNEY, R. J., WEIL, S. J., SCHERER, J. & VALLEE, R. B. 2011. Mutually exclusive cytoplasmic dynein regulation by NudE-Lis1 and dynactin. *J Biol Chem,* 286**,** 39615-22.

MEJILLANO, M. R. & HIMES, R. H. 1991. Binding of guanine nucleotides and Mg2+ to tubulin with a nucleotide-depleted exchangeable site. *Arch Biochem Biophys,* 291**,** 356-62.

MEYER, T. S. & LAMBERTS, B. L. 1965. Use of coomassie brilliant blue R250 for the electrophoresis of microgram quantities of parotid saliva proteins on acrylamide-gel strips. *Biochim Biophys Acta,* 107**,** 144-5.

MISHIMA, M., MAESAKI, R., KASA, M., WATANABE, T., FUKATA, M., KAIBUCHI, K. & HAKOSHIMA, T. 2007. Structural basis for tubulin recognition by cytoplasmic linker protein 170 and its autoinhibition. *Proc Natl Acad Sci U S A,* 104**,** 10346-51.

MISSIMER, J. H., DOLENC, J., STEINMETZ, M. O. & VAN GUNSTEREN, W. F. 2010. Exploring the trigger sequence of the GCN4 coiled-coil: biased molecular

dynamics resolves apparent inconsistencies in NMR measurements. *Protein Sci,* 19**,** 2462-74.
MITCHISON, T. & KIRSCHNER, M. 1984. Dynamic instability of microtubule growth. *Nature,* 312**,** 237-42.
MITCHISON, T. J. 1993. Localization of an exchangeable GTP binding site at the plus end of microtubules. *Science,* 261**,** 1044-7.
MIURA, M., MATSUBARA, A., KOBAYASHI, T., EDAMATSU, M. & TOYOSHIMA, Y. Y. 2010. Nucleotide-dependent behavior of single molecules of cytoplasmic dynein on microtubules in vitro. *FEBS Lett,* 584**,** 2351-5.
MOHAN, R., KATRUKHA, E. A., DOODHI, H., SMAL, I., MEIJERING, E., KAPITEIN, L. C., STEINMETZ, M. O. & AKHMANOVA, A. 2013. End-binding proteins sensitize microtubules to the action of microtubule-targeting agents. *Proc Natl Acad Sci U S A,* 110**,** 8900-5.
MONTENEGRO GOUVEIA, S., LESLIE, K., KAPITEIN, L. C., BUEY, R. M., GRIGORIEV, I., WAGENBACH, M., SMAL, I., MEIJERING, E., HOOGENRAAD, C. C., WORDEMAN, L., STEINMETZ, M. O. & AKHMANOVA, A. 2010. In vitro reconstitution of the functional interplay between MCAK and EB3 at microtubule plus ends. *Curr Biol,* 20**,** 1717-22.
MOORES, C. A., PERDERISET, M., KAPPELER, C., KAIN, S., DRUMMOND, D., PERKINS, S. J., CHELLY, J., CROSS, R., HOUDUSSE, A. & FRANCIS, F. 2006. Distinct roles of doublecortin modulating the microtubule cytoskeleton. *Embo J,* 25**,** 4448-57.
MOUGHAMIAN, A. J. & HOLZBAUR, E. L. 2012. Dynactin is required for transport initiation from the distal axon. *Neuron,* 74**,** 331-43.
MOUGHAMIAN, A. J., OSBORN, G. E., LAZARUS, J. E., MADAY, S. & HOLZBAUR, E. L. 2013. Ordered recruitment of dynactin to the microtubule plus-end is required for efficient initiation of retrograde axonal transport. *J Neurosci,* 33**,** 13190-203.
MULLER-REICHERT, T., CHRETIEN, D., SEVERIN, F. & HYMAN, A. A. 1998. Structural changes at microtubule ends accompanying GTP hydrolysis: information from a slowly hydrolyzable analogue of GTP, guanylyl (alpha,beta)methylenediphosphonate. *Proc Natl Acad Sci U S A,* 95**,** 3661-6.
NAKAMURA, S., GRIGORIEV, I., NOGI, T., HAMAJI, T., CASSIMERIS, L. & MIMORI-KIYOSUE, Y. 2012. Dissecting the nanoscale distributions and functions of microtubule-end-binding proteins EB1 and ch-TOG in interphase HeLa cells. *PLoS One,* 7**,** e51442.
NAWROTEK, A., KNOSSOW, M. & GIGANT, B. 2011. The determinants that govern microtubule assembly from the atomic structure of GTP-tubulin. *J Mol Biol,* 412**,** 35-42.
NIEDERMAN, R., AMREIN, P. C. & HARTWIG, J. 1983. Three-dimensional structure of actin filaments and of an actin gel made with actin-binding protein. *J Cell Biol,* 96**,** 1400-13.
NIETHAMMER, P., BASTIAENS, P. & KARSENTI, E. 2004. Stathmin-tubulin interaction gradients in motile and mitotic cells. *Science,* 303**,** 1862-6.
O'BRIEN, E. T., SALMON, E. D. & ERICKSON, H. P. 1997. How calcium causes microtubule depolymerization. *Cell Motil Cytoskeleton,* 36**,** 125-35.

O'BRIEN, E. T., SALMON, E. D., WALKER, R. A. & ERICKSON, H. P. 1990. Effects of magnesium on the dynamic instability of individual microtubules. *Biochemistry,* 29**,** 6648-56.

ODDE, D. J., CASSIMERIS, L. & BUETTNER, H. M. 1995. Kinetics of microtubule catastrophe assessed by probabilistic analysis. *Biophys J,* 69**,** 796-802.

OLMSTED, J. B. & BORISY, G. G. 1975. Ionic and nucleotide requirements for microtubule polymerization in vitro. *Biochemistry,* 14**,** 2996-3005.

OTTERBEIN, L. R., GRACEFFA, P. & DOMINGUEZ, R. 2001. The crystal structure of uncomplexed actin in the ADP state. *Science,* 293**,** 708-11.

OZAKI, Y., MATSUI, H., NAGAMACHI, A., ASOU, H., AKI, D. & INABA, T. 2011. The dynactin complex maintains the integrity of metaphasic centrosomes to ensure transition to anaphase. *J Biol Chem,* 286**,** 5589-98.

PADINHATEERI, R., KOLOMEISKY, A. B. & LACOSTE, D. 2012. Random hydrolysis controls the dynamic instability of microtubules. *Biophys J,* 102**,** 1274-83.

PALUCH, E. K. & RAZ, E. 2013. The role and regulation of blebs in cell migration. *Curr Opin Cell Biol,* 25**,** 582-90.

PECQUEUR, L., DUELLBERG, C., DREIER, B., JIANG, Q., WANG, C., PLUCKTHUN, A., SURREY, T., GIGANT, B. & KNOSSOW, M. 2012. A designed ankyrin repeat protein selected to bind to tubulin caps the microtubule plus end. *Proc Natl Acad Sci U S A,* 109**,** 12011-6.

PEDIGO, S. & WILLIAMS, R. C., JR. 2002. Concentration dependence of variability in growth rates of microtubules. *Biophys J,* 83**,** 1809-19.

PETRY, S., GROEN, A. C., ISHIHARA, K., MITCHISON, T. J. & VALE, R. D. 2013. Branching microtubule nucleation in Xenopus egg extracts mediated by augmin and TPX2. *Cell,* 152**,** 768-77.

PHAN, J., ZDANOV, A., EVDOKIMOV, A. G., TROPEA, J. E., PETERS, H. K., 3RD, KAPUST, R. B., LI, M., WLODAWER, A. & WAUGH, D. S. 2002. Structural basis for the substrate specificity of tobacco etch virus protease. *J Biol Chem,* 277**,** 50564-72.

PHILIMONENKO, V. V., ZHAO, J., IBEN, S., DINGOVA, H., KYSELA, K., KAHLE, M., ZENTGRAF, H., HOFMANN, W. A., DE LANEROLLE, P., HOZAK, P. & GRUMMT, I. 2004. Nuclear actin and myosin I are required for RNA polymerase I transcription. *Nat Cell Biol,* 6**,** 1165-72.

PIETTE, B. M., LIU, J., PEETERS, K., SMERTENKO, A., HAWKINS, T., DEEKS, M., QUINLAN, R., ZAKRZEWSKI, W. J. & HUSSEY, P. J. 2009. A thermodynamic model of microtubule assembly and disassembly. *PLoS One,* 4**,** e6378.

POZO-GUISADO, E., CASAS-RUA, V., TOMAS-MARTIN, P., LOPEZ-GUERRERO, A. M., ALVAREZ-BARRIENTOS, A. & MARTIN-ROMERO, F. J. 2013. Phosphorylation of STIM1 at ERK1/2 target sites regulates interaction with the microtubule plus-end binding protein EB1. *J Cell Sci,* 126**,** 3170-80.

PROTA, A. E., BARGSTEN, K., ZURWERRA, D., FIELD, J. J., DIAZ, J. F., ALTMANN, K. H. & STEINMETZ, M. O. 2013. Molecular mechanism of action of microtubule-stabilizing anticancer agents. *Science,* 339**,** 587-90.

RAVELLI, R. B., GIGANT, B., CURMI, P. A., JOURDAIN, I., LACHKAR, S., SOBEL, A. & KNOSSOW, M. 2004. Insight into tubulin regulation from a complex with colchicine and a stathmin-like domain. *Nature,* 428**,** 198-202.

RAY, S., MEYHOFER, E., MILLIGAN, R. A. & HOWARD, J. 1993. Kinesin follows the microtubule's protofilament axis. *J Cell Biol,* 121**,** 1083-93.

RECK-PETERSON, S. L., YILDIZ, A., CARTER, A. P., GENNERICH, A., ZHANG, N. & VALE, R. D. 2006. Single-Molecule Analysis of Dynein Processivity and Stepping Behavior. *Cell,* 126**,** 335-348.

REYNOLDS, O. 1895. On the Dynamical Theory of Incompressible Viscous Fluids and the Determination of the Criterion. *Philos. Trans. R. Soc. London Ser. A,* 186.

RICE, L. M., MONTABANA, E. A. & AGARD, D. A. 2008. The lattice as allosteric effector: structural studies of alphabeta- and gamma-tubulin clarify the role of GTP in microtubule assembly. *Proc Natl Acad Sci U S A,* 105**,** 5378-83.

RODIONOV, V. I., GYOEVA, F. K., TANAKA, E., BERSHADSKY, A. D., VASILIEV, J. M. & GELFAND, V. I. 1993. Microtubule-dependent control of cell shape and pseudopodial activity is inhibited by the antibody to kinesin motor domain. *J Cell Biol,* 123**,** 1811-20.

ROOSTALU, J., HENTRICH, C., BIELING, P., TELLEY, I. A., SCHIEBEL, E. & SURREY, T. 2011. Directional switching of the kinesin Cin8 through motor coupling. *Science,* 332**,** 94-9.

RUBIN, C. I. & ATWEH, G. F. 2004. The role of stathmin in the regulation of the cell cycle. *J Cell Biochem,* 93**,** 242-50.

SAXTON, W. M., STEMPLE, D. L., LESLIE, R. J., SALMON, E. D., ZAVORTINK, M. & MCINTOSH, J. R. 1984. Tubulin dynamics in cultured mammalian cells. *J Cell Biol,* 99**,** 2175-86.

SCHAEFER, A. W., SCHOONDERWOERT, V. T., JI, L., MEDERIOS, N., DANUSER, G. & FORSCHER, P. 2008. Coordination of actin filament and microtubule dynamics during neurite outgrowth. *Dev Cell,* 15**,** 146-62.

SCHEEL, J., PIERRE, P., RICKARD, J. E., DIAMANTOPOULOS, G. S., VALETTI, C., VAN DER GOOT, F. G., HANER, M., AEBI, U. & KREIS, T. E. 1999. Purification and analysis of authentic CLIP-170 and recombinant fragments. *J Biol Chem,* 274**,** 25883-91.

SCHEFFERS, D. J., DEN BLAAUWEN, T. & DRIESSEN, A. J. 2000. Non-hydrolysable GTP-gamma-S stabilizes the FtsZ polymer in a GDP-bound state. *Mol Microbiol,* 35**,** 1211-9.

SCHEK, H. T., 3RD, GARDNER, M. K., CHENG, J., ODDE, D. J. & HUNT, A. J. 2007. Microtubule assembly dynamics at the nanoscale. *Curr Biol,* 17**,** 1445-55.

SCHROER, T. A. 2004. Dynactin. *Annual Review of Cell and Developmental Biology,* 20**,** 759-779.

SCHULER, H. 2001. ATPase activity and conformational changes in the regulation of actin. *Biochim Biophys Acta,* 1549**,** 137-47.

SEETAPUN, D., CASTLE, B. T., MCINTYRE, A. J., TRAN, P. T. & ODDE, D. J. 2012. Estimating the microtubule GTP cap size in vivo. *Curr Biol,* 22**,** 1681-7.

SELIGMANN, J. & TWELVES, C. 2013. Tubulin: an example of targeted chemotherapy. *Future Med Chem,* 5**,** 339-52.

SHELANSKI, M. L. & TAYLOR, E. W. 1967. Isolation of a protein subunit from microtubules. *J Cell Biol,* 34**,** 549-54.

SODEIK, B., EBERSOLD, M. W. & HELENIUS, A. 1997. Microtubule-mediated transport of incoming herpes simplex virus 1 capsids to the nucleus. *J Cell Biol,* 136**,** 1007-21.

SPIEGELMAN, B. M., PENNINGROTH, S. M. & KIRSCHNER, M. W. 1977. Turnover of tubulin and the N site GTP in Chinese hamster ovary cells. *Cell,* 12**,** 587-600.

SPLINTER, D., RAZAFSKY, D. S., SCHLAGER, M. A., SERRA-MARQUES, A., GRIGORIEV, I., DEMMERS, J., KEIJZER, N., JIANG, K., POSER, I., HYMAN, A. A., HOOGENRAAD, C. C., KING, S. J. & AKHMANOVA, A. 2012. BICD2, dynactin, and LIS1 cooperate in regulating dynein recruitment to cellular structures. *Mol Biol Cell,* 23**,** 4226-41.

STEINMETZ, M. O. 2007. Structure and thermodynamics of the tubulin-stathmin interaction. *J Struct Biol,* 158**,** 137-47.

STEWART, M. P., HELENIUS, J., TOYODA, Y., RAMANATHAN, S. P., MULLER, D. J. & HYMAN, A. A. 2011. Hydrostatic pressure and the actomyosin cortex drive mitotic cell rounding. *Nature,* 469**,** 226-30.

STEWART, R. J., FARRELL, K. W. & WILSON, L. 1990. Role of GTP hydrolysis in microtubule polymerization: evidence for a coupled hydrolysis mechanism. *Biochemistry,* 29**,** 6489-98.

STOCKMANN, M., MEYER-OHLENDORF, M., ACHBERGER, K., PUTZ, S., DEMESTRE, M., YIN, H., HENDRICH, C., LINTA, L., HEINRICH, J., BRUNNER, C., PROEPPER, C., KUH, G. F., BAUMANN, B., LANGER, T., SCHWALENSTOCKER, B., BRAUNSTEIN, K. E., VON ARNIM, C., SCHNEUWLY, S., MEYER, T., WONG, P. C., BOECKERS, T. M., LUDOLPH, A. C. & LIEBAU, S. 2013. The dynactin p150 subunit: cell biology studies of sequence changes found in ALS/MND and Parkinsonian syndromes. *J Neural Transm,* 120**,** 785-98.

SUN, L., GAO, J., DONG, X., LIU, M., LI, D., SHI, X., DONG, J. T., LU, X., LIU, C. & ZHOU, J. 2008. EB1 promotes Aurora-B kinase activity through blocking its inactivation by protein phosphatase 2A. *Proc Natl Acad Sci U S A,* 105**,** 7153-8.

SUN, L., LIU, A. & GEORGOPOULOS, K. 1996. Zinc finger-mediated protein interactions modulate Ikaros activity, a molecular control of lymphocyte development. *Embo J,* 15**,** 5358-69.

TANAKA, K., MUKAE, N., DEWAR, H., VAN BREUGEL, M., JAMES, E. K., PRESCOTT, A. R., ANTONY, C. & TANAKA, T. U. 2005. Molecular mechanisms of kinetochore capture by spindle microtubules. *Nature,* 434**,** 987-94.

TANENBAUM, M. E., MACUREK, L., GALJART, N. & MEDEMA, R. H. 2008. Dynein, Lis1 and CLIP-170 counteract Eg5-dependent centrosome separation during bipolar spindle assembly. *Embo J,* 27**,** 3235-45.

TEIXIDO-TRAVESA, N., ROIG, J. & LUDERS, J. 2012. The where, when and how of microtubule nucleation - one ring to rule them all. *J Cell Sci,* 125**,** 4445-56.

TELLEY, I. A., BIELING, P. & SURREY, T. 2011. Reconstitution and quantification of dynamic microtubule end tracking in vitro using TIRF microscopy. *Methods Mol Biol,* 777**,** 127-45.

TOURNEBIZE, R., POPOV, A., KINOSHITA, K., ASHFORD, A. J., RYBINA, S., POZNIAKOVSKY, A., MAYER, T. U., WALCZAK, C. E., KARSENTI, E. & HYMAN, A. A. 2000. Control of microtubule dynamics by the antagonistic activities of XMAP215 and XKCM1 in Xenopus egg extracts. *Nat Cell Biol,* 2**,** 13-9.

TOWBIN, H., STAEHELIN, T. & GORDON, J. 1992. Electrophoretic transfer of proteins from polyacrylamide gels to nitrocellulose sheets: procedure and some applications. 1979. *Biotechnology,* 24**,** 145-9.

TRAN, P. T., WALKER, R. A. & SALMON, E. D. 1997. A metastable intermediate state of microtubule dynamic instability that differs significantly between plus and minus ends. *J Cell Biol,* 138**,** 105-17.

TREISMAN, R. 2013. Shedding light on nuclear actin dynamics and function. *Trends Biochem Sci,* 38**,** 376-7.

TROKTER, M., MUCKE, N. & SURREY, T. 2012. Reconstitution of the human cytoplasmic dynein complex. *Proc Natl Acad Sci U S A,* 109**,** 20895-900.

TROPINI, C., ROTH, E. A., ZANIC, M., GARDNER, M. K. & HOWARD, J. 2012. Islands containing slowly hydrolyzable GTP analogs promote microtubule rescues. *PLoS One,* 7**,** e30103.

ULLMANN, A., JACOB, F. & MONOD, J. 1967. Characterization by in vitro complementation of a peptide corresponding to an operator-proximal segment of the beta-galactosidase structural gene of Escherichia coli. *J Mol Biol,* 24**,** 339-43.

UTENG, M., HENTRICH, C., MIURA, K., BIELING, P. & SURREY, T. 2008. Poleward transport of Eg5 by dynein-dynactin in Xenopus laevis egg extract spindles. *The Journal of Cell Biology,* 182**,** 715-726.

VALE, R. D., MALIK, F. & BROWN, D. 1992. Directional instability of microtubule transport in the presence of kinesin and dynein, two opposite polarity motor proteins. *J Cell Biol,* 119**,** 1589-96.

VALIRON, O., ARNAL, I., CAUDRON, N. & JOB, D. 2010. GDP-tubulin incorporation into growing microtubules modulates polymer stability. *J Biol Chem,* 285**,** 17507-13.

VAN DER VAART, B., MANATSCHAL, C., GRIGORIEV, I., OLIERIC, V., GOUVEIA, S. M., BJELIC, S., DEMMERS, J., VOROBJEV, I., HOOGENRAAD, C. C., STEINMETZ, M. O. & AKHMANOVA, A. 2011. SLAIN2 links microtubule plus end-tracking proteins and controls microtubule growth in interphase. *J Cell Biol,* 193**,** 1083-99.

VANDECANDELAERE, A., BRUNE, M., WEBB, M. R., MARTIN, S. R. & BAYLEY, P. M. 1999. Phosphate release during microtubule assembly: what stabilizes growing microtubules? *Biochemistry,* 38**,** 8179-88.

VARGA, V., HELENIUS, J., TANAKA, K., HYMAN, A. A., TANAKA, T. U. & HOWARD, J. 2006. Yeast kinesin-8 depolymerizes microtubules in a length-dependent manner. *Nat Cell Biol,* 8**,** 957-62.

VASQUEZ, R. J., HOWELL, B., YVON, A. M., WADSWORTH, P. & CASSIMERIS, L. 1997. Nanomolar concentrations of nocodazole alter microtubule dynamic instability in vivo and in vitro. *Mol Biol Cell,* 8**,** 973-85.

VAUGHAN, K. T., TYNAN, S. H., FAULKNER, N. E., ECHEVERRI, C. J. & VALLEE, R. B. 1999. Colocalization of cytoplasmic dynein with dynactin and CLIP-170 at microtubule distal ends. *J Cell Sci,* 112 (Pt 10)**,** 1437-47.

VAUGHAN, K. T. & VALLEE, R. B. 1995. Cytoplasmic dynein binds dynactin through a direct interaction between the intermediate chains and p150Glued. *J Cell Biol,* 131**,** 1507-16.

VAUGHAN, P. S., MIURA, P., HENDERSON, M., BYRNE, B. & VAUGHAN, K. T. 2002. A role for regulated binding of p150(Glued) to microtubule plus ends in organelle transport. *J Cell Biol,* 158**,** 305-19.

VERHEY, K. J. & HAMMOND, J. W. 2009. Traffic control: regulation of kinesin motors. *Nat Rev Mol Cell Biol,* 10**,** 765-77.

VIOVY 2000. Electrophoresis of DNA and other polyelectrolytes: Physical mechanisms. *Rev. Mod. Phys.*

VITRE, B., COQUELLE, F. M., HEICHETTE, C., GARNIER, C., CHRETIEN, D. & ARNAL, I. 2008. EB1 regulates microtubule dynamics and tubulin sheet closure in vitro. *Nat Cell Biol,* 10**,** 415-21.

VOLKOV, V. A., ZAYTSEV, A. V., GUDIMCHUK, N., GRISSOM, P. M., GINTSBURG, A. L., ATAULLAKHANOV, F. I., MCINTOSH, J. R. & GRISHCHUK, E. L. 2013. Long tethers provide high-force coupling of the Dam1 ring to shortening microtubules. *Proc Natl Acad Sci U S A,* 110**,** 7708-13.

VOTER, W. A., O'BRIEN, E. T. & ERICKSON, H. P. 1991. Dilution-induced disassembly of microtubules: relation to dynamic instability and the GTP cap. *Cell Motil Cytoskeleton,* 18**,** 55-62.

WADE, R. H. 2009. On and around microtubules: an overview. *Mol Biotechnol,* 43**,** 177-91.

WALKER, R. A., INOUE, S. & SALMON, E. D. 1989. Asymmetric behavior of severed microtubule ends after ultraviolet-microbeam irradiation of individual microtubules in vitro. *J Cell Biol,* 108**,** 931-7.

WALKER, R. A., O'BRIEN, E. T., PRYER, N. K., SOBOEIRO, M. F., VOTER, W. A., ERICKSON, H. P. & SALMON, E. D. 1988. Dynamic instability of individual microtubules analyzed by video light microscopy: rate constants and transition frequencies. *J Cell Biol,* 107**,** 1437-48.

WALKER, R. A., PRYER, N. K. & SALMON, E. D. 1991. Dilution of individual microtubules observed in real time in vitro: evidence that cap size is small and independent of elongation rate. *J Cell Biol,* 114**,** 73-81.

WANG, H. W. & NOGALES, E. 2005. Nucleotide-dependent bending flexibility of tubulin regulates microtubule assembly. *Nature,* 435**,** 911-5.

WANG, K. K. 2000. Calpain and caspase: can you tell the difference? *Trends Neurosci,* 23**,** 20-6.

WANG, S. & ZHENG, Y. 2011. Identification of a novel Dynein binding domain in nudel essential for spindle pole organization in Xenopus egg extract. *J Biol Chem,* 286**,** 587-93.

WANG, X., WINTER, D., ASHRAFI, G., SCHLEHE, J., WONG, Y. L., SELKOE, D., RICE, S., STEEN, J., LAVOIE, M. J. & SCHWARZ, T. L. 2011. PINK1 and Parkin target Miro for phosphorylation and degradation to arrest mitochondrial motility. *Cell,* 147**,** 893-906.

WATSON, P. 2006. Microtubule plus-end loading of p150Glued is mediated by EB1 and CLIP-170 but is not required for intracellular membrane traffic in mammalian cells. *Journal of Cell Science,* 119**,** 2758-2767.

WEISBRICH, A., HONNAPPA, S., JAUSSI, R., OKHRIMENKO, O., FREY, D., JELESAROV, I., AKHMANOVA, A. & STEINMETZ, M. O. 2007. Structure-function relationship of CAP-Gly domains. *Nature Structural & Molecular Biology,* 14**,** 959-967.

WEISENBERG, R. C., BORISY, G. G. & TAYLOR, E. W. 1968. The colchicine-binding protein of mammalian brain and its relation to microtubules. *Biochemistry,* 7**,** 4466-79.

WELTE, M. A. 2004. Bidirectional transport along microtubules. *Curr Biol,* 14**,** R525-37.

WENG, J. H., LIANG, M. R., CHEN, C. H., TONG, S. K., HUANG, T. C., LEE, S. P., CHEN, Y. R., CHEN, C. T. & CHUNG, B. C. 2013. Pregnenolone activates CLIP-170 to promote microtubule growth and cell migration. *Nat Chem Biol,* 9**,** 636-42.

WITKE, W., PODTELEJNIKOV, A. V., DI NARDO, A., SUTHERLAND, J. D., GURNIAK, C. B., DOTTI, C. & MANN, M. 1998. In mouse brain profilin I and profilin II associate with regulators of the endocytic pathway and actin assembly. *Embo J,* 17**,** 967-76.

WITTMANN, T., HYMAN, A. & DESAI, A. 2001. The spindle: a dynamic assembly of microtubules and motors. *Nat Cell Biol,* 3**,** E28-34.

WOLTER 2003. Introduction to Variance Estimation. *Springer Series in Statistics*.

WORDEMAN, L. & MITCHISON, T. J. 1995. Identification and partial characterization of mitotic centromere-associated kinesin, a kinesin-related protein that associates with centromeres during mitosis. *J Cell Biol,* 128**,** 95-104.

WOZNIAK, M. J., BOLA, B., BROWNHILL, K., YANG, Y. C., LEVAKOVA, V. & ALLAN, V. J. 2009. Role of kinesin-1 and cytoplasmic dynein in endoplasmic reticulum movement in VERO cells. *J Cell Sci,* 122**,** 1979-89.

YAMADA, M., TOBA, S., TAKITOH, T., YOSHIDA, Y., MORI, D., NAKAMURA, T., IWANE, A. H., YANAGIDA, T., IMAI, H., YU-LEE, L. Y., SCHROER, T., WYNSHAW-BORIS, A. & HIROTSUNE, S. 2010. mNUDC is required for plus-end-directed transport of cytoplasmic dynein and dynactins by kinesin-1. *Embo J,* 29**,** 517-31.

YANG, M. 2014. Slow diffusion underlies alternation of fast and slow growth periods of microtubule assembly. *ScientificWorldJournal,* 2014**,** 601898.

YEH, T. Y., QUINTYNE, N. J., SCIPIONI, B. R., ECKLEY, D. M. & SCHROER, T. A. 2012. Dynactin's pointed-end complex is a cargo-targeting module. *Mol Biol Cell,* 23**,** 3827-37.

ZHANG, H. & LABOUESSE, M. 2010. The making of hemidesmosome structures in vivo. *Dev Dyn,* 239**,** 1465-76.

ZHANG, J., LI, S., FISCHER, R. & XIANG, X. 2003. Accumulation of cytoplasmic dynein and dynactin at microtubule plus ends in Aspergillus nidulans is kinesin dependent. *Mol Biol Cell,* 14**,** 1479-88.

ZHAPPAROVA, O. N., BRYANTSEVA, S. A., DERGUNOVA, L. V., RAEVSKAYA, N. M., BURAKOV, A. V., BANTYSH, O. B., SHANINA, N. A. & NADEZHDINA, E. S. 2009. Dynactin Subunit p150Glued Isoforms Notable for Differential Interaction with Microtubules. *Traffic,* 10**,** 1635-1646.

ZOVKO, S., ABRAHAMS, J. P., KOSTER, A. J., GALJART, N. & MOMMAAS, A. M. 2008. Microtubule plus-end conformations and dynamics in the periphery of interphase mouse fibroblasts. *Mol Biol Cell,* 19**,** 3138-46.

ZUELA, N., BAR, D. Z. & GRUENBAUM, Y. 2012. Lamins in development, tissue maintenance and stress. *EMBO Rep,* 13**,** 1070-8.